Evolution of Galaxy Morphology in the Field and Cluster Environment Since $z \sim 1$

by

Angelo George

A Thesis Submitted to Saint Mary's University, Halifax, Nova Scotia in Partial Fulfillment
of the Requirements for the Degree of Master of Science in Astronomy
(Department of Astronomy and Physics)

August, 2020, Halifax, Nova Scotia

Approved: ________________
Dr. Marcin Sawicki
Supervisor

Approved: ________________
Dr. Ivana Damjanov
Supervisor

Approved:________________
Dr. Robert Thacker
Examiner

Approved:________________
Dr. Vincent Hénault-Brunet
Examiner

Date: AUGUST 13, 2020.

Acknowledgements

Firstly, I thank my supervisors, Dr. Marcin Sawicki and Dr. Ivana Damjanov, for guiding me constantly in my research with patience. I have learned from them what it takes to be a good Astronomer during the last two years. I extend my thanks to Dr. Thibaud Moutard and Anneya Golob for the catalogues they made for galaxies studied in this thesis. I also wish to acknowledge the help provided by Harrison Souchereau towards my research.

A special thanks to the extra-galactic group in the department for the weekly ArXiv meetings. I would also like to express my great appreciation to the group of HSC collaborators worldwide for their valuable inputs. I acknowledge Dr. Masamune Oguri and Dr. Jubee Sohn for the membership details of cluster galaxies in HSC and HST data respectively. I also thank Dr. Robert Thacker and Dr. Vincent Hénault-Brunet for their suggestions to improve my thesis. I am particularly grateful for the assistance given by Compute Canada support team to run my algorithm efficiently.

I would like to express my deep gratitude to the Department of Astronomy for welcoming me as one of them and assisting me throughout my Master's programme. I wish to acknowledge the peer support of all graduate students in the department. I also thank CCO group on the campus for their comradeship I enjoyed.

I am also grateful to my family and my best friend, Charles Cruz, for their constant support and encouragement. Last but not least, I thank Almighty God, the faith in whom has helped me overcome the obstacles I faced.

Contents

List of Figures

List of Tables

Abstract

Evolution of Galaxy Morphology in the Field and Cluster Environment Since $z \sim 1$

by Angelo George

The study of galaxy morphology can provide important information about how galaxies evolve. In this thesis, we study size and concentration of light profiles for $\sim$15000 star-forming galaxies (SFGs, $M_* \gtrsim 10^{9.5}$ M$_\odot$) and $\sim$5000 massive quiescent galaxies (QGs, $M_* \gtrsim 10^{10}$ M$_\odot$) in the COSMOS/UltraVISTA region using CLAUDS+HSC-SSP *griz* bands at $0.1 < z < 0.9$. We find a slow evolution in the characteristic sizes of SFGs, $R_e \propto (1+z)^{-0.45}$, which is consistent with the growth of their bulges. In contrast, the characteristic size of QGs grows faster, $R_e \propto (1+z)^{-1.06}$, driven by several physical processes including progenitor bias, adiabatic expansion, and merging. Analysis of 75 cluster galaxies does not show any significant difference from the field galaxies. However, a separate analysis of $\sim$130 spectroscopically confirmed members of five cluster cores from the HST CLASH survey provide evidence for the effects of the densest environments on QG size.

August 13, 2020

Chapter 1

Introduction

Galaxies are fundamental building blocks of structure in the Universe. They are formed at the centres of the potential wells of dark matter halos through gravitational collapse of matter (Ratra & Vogeley 2008; Benson 2010; Somerville & Davé 2015). The continuous changes in abundance and physical properties of systems in two major galaxy populations - star forming and quiescent - reflect the processes that drive galaxy evolution in the ageing Universe (Shen et al. 2003; Ravindranath et al. 2004; Blanton & Moustakas 2009; Kormendy et al. 2009; Szomoru et al. 2011; Bezanson et al. 2012; Conselice 2014; van der Wel et al. 2014; Feldmann et al. 2017).

Star-forming galaxies (SFGs) are characterised by high gas fractions and associated high star formation rates (e.g., Brinchmann et al. 2004; Feldmann et al. 2017). The light from these galaxies is dominated by young massive stars, which make them blue, although the dust present in them can redden them by absorbing light at shorter wavelengths and re-emitting in longer wavelengths (Xiao et al. 2012). At $z \sim 0$, star formation is confined in disks that dominate galaxy light profiles. At $z \sim 2$, however, vigorous star formation activity is concentrated in large, bright clumps (e.g., Genzel et al. 2011). Observational studies show that star formation rates in SFGs have been decreasing with time since $z \sim 1.5$ (e.g., Lilly et al. 1996; Sawicki et al. 1997; Daddi et al. 2007; Reddy et al. 2012; Madau & Dickinson 2014; Pannella et al. 2015).

In contrast, quiescent galaxies (QGs) represent a galaxy population where star formation activities are either suppressed or minimal (Renzini 2006; Valentino et al. 2020). They have limited cold gas in them and their light profiles are dominated by red, low-mass, older stars (e.g., Fabello et al. 2011; Huang et al. 2012). QGs have a more centrally concentrated morphology compared to SFGs (e.g., Mowla et al. 2019b). As the Universe ages, the fraction of QGs is increasing; at higher masses ($M_* \gtrsim 10^{10}$ $M_\odot$), QGs dominate the galaxy population in the local Universe (e.g., Blanton & Moustakas 2009).

Star formation activity in individual SFGs ceases eventually as they evolve (galaxy quenching, Fang et al. 2013) and thus, there is a clear evolutionary connection between SFGs and QGs. Depletion of gas reservoirs and/or heating of gas can quench star formation in galaxies and there are several processes that can contribute to these quenching mechanisms. Feedback processes from active galactic nuclei (AGNs) and supernovae can expel cold gas from galaxies (e.g., Hopkins et al. 2006). AGN feedback can also heat the surrounding gas which will prevent star formation in galaxies (Croton et al. 2006).

Alternatively, bulge formation and growth in the centres of galaxies can aid quenching. For gas in a galaxy to collapse and form stars, it should satisfy Toomre's stability criterion, $Q < 1$, where the Toomre Q parameter is proportional to epicyclic frequency (κ), which is connected to the depth of the gravitational potential (Toomre 1964). Because the stellar population in the bulges are centrally concentrated, bulges have a deeper gravitational potential well than disks. Thus, growth of bulges increases the value of the Toomre Q parameter, which can prevent gas from collapsing and forming stars in galaxies (Martig et al. 2009; Fang et al. 2013).

Star formation can also be suppressed through collisional and non-collisional galaxy interactions (Gabor et al. 2010). Collisional interactions (galaxy mergers) occur when the orbital energy of the interacting galaxies is lower than their internal velocity dispersions, and such interactions can induce AGN activity that heats the gas. Mergers generally happen in galaxy groups and outskirts of galaxy clusters where the number density of galaxies is high and the orbital energy of galaxies is lower than their internal energy. High speed non-collisional interactions such as harassment and tidal stripping can deplete the cold gas reservoirs of galaxies thereby preventing star formation (e.g., Farouki & Shapiro 1981; Ferguson & Binggeli 1994). Such interactions are common in the dense cores of clusters where the galaxies move fast. Furthermore, environmental processes such as ram pressure stripping and strangulation can also deplete galaxies' cold gas reservoirs (van de Voort et al.

2017).

One of the most accessible tracers of the physical properties of a galaxy is its morphology - the distribution of galaxy light projected on the sky in a given range of wavelengths (i.e., galaxy appearance in astronomical images). Studying the morphologies of galaxies helps us understand these underlying physical properties and the processes that drive the change in physical properties (i.e., evolution) of galaxies. For example, disky SFGs are rotationally supported whereas elliptical or bulgy QGs are dynamically hot with relatively high internal velocity dispersions compared to SFGs (van der Kruit & Freeman 2011; Bezanson et al. 2012). Moreover, all the processes that quench galaxies will also affect galaxy morphology.

There are two approaches to the analysis of galaxy light profiles in general: parametric and non-parametric. In parametric methods, one or more analytic functions are used to model the light profiles of galaxies (e.g., de Vaucouleurs 1953; Sersic 1968; Peng et al. 2010a). In contrast, the non-parametric approach quantifies galaxy morphology by measuring structural properties of galaxies such as asymmetries and clumpiness without the assumption that a galaxy can be represented by an analytic function (e.g., Petrosian 1976; Lotz et al. 2004). Both methods have their advantages and disadvantages. The non-parametric approach is highly useful to study the morphological features of irregular galaxies as well as merging systems, because such features are difficult to model using standard analytic functions. However, the robustness of the non-parametric methods depends on the depth of the image. On the other hand, parametric methods can model a galaxy even to galaxy surface brightness levels that are fainter than the background sky value by extrapolating the observable fraction of galaxy light profile with the aid of analytic functions. Such extrapolation is important to study the evolution in galaxy morphology since galaxies at higher redshift have lower apparent surface brightness than those in the local Universe. Hence, a number of studies focused on the evolution in galaxy morphology utilise the parametric approach (e.g., Williams et al. 2010; Peng et al. 2010b; van der Wel et al. 2014; Faisst et al. 2017; Mowla et al. 2019a,b).

1.1 Evolution of Galaxy Morphology

In parametric studies, parameters of the analytic functions that describe galaxy light profiles are related to the key morphological indicators: size of galaxies and the concentration of their light profiles. Observations show that galaxy size and concentration vary with star formation activity, stellar mass and redshift (e.g., Shen et al. 2003; Williams et al. 2010; van der Wel et al. 2014; Morishita et al. 2014; Lange et al. 2015; Faisst et al. 2017; Damjanov et al. 2019; Mowla et al. 2019b; Matharu et al. 2019, 2020). These studies have also shown that SFG and QG populations evolve differently and the difference in evolution is reflected in their morphologies. Generally, QGs have more centrally concentrated morphology and are comparatively smaller in sizes than SFGs at a given stellar mass and redshift. Within the SFG or QG population, massive galaxies in general are larger in size than low mass galaxies while galaxies at lower redshift are larger than those at higher redshift.

The relation between size and stellar mass differs for SFGs and QGs (e.g., Shen et al. 2003; Williams et al. 2010; van der Wel et al. 2014; Mowla et al. 2019b). These studies show that this relation between size and mass for SFGs can be described by a single power law over the entire mass range. In comparison with SFGs, QGs have a more complex relation between size and mass: low mass QGs ($M_* \lesssim 10^{10.3}$ $\mathrm{M}_\odot$) show a weak relation similar to SFGs, but high mass QGs ($M_* \gtrsim 10^{10.3}$ $\mathrm{M}_\odot$) show a significantly stronger positive correlation between size and stellar mass.

Furthermore, SFGs and QGs show different dependencies between average galaxy size for a given stellar mass and redshift. The pace of the redshift evolution of average size for the SFG population decreases with cosmic time; SFGs at earlier epochs grew in size faster than those at later epochs (Ferguson et al. 2004; Oesch et al. 2010; Mosleh et al. 2012; Franx et al. 2008; Williams et al. 2010; van der Wel et al. 2014; Mowla et al. 2019b; Lilly et al. 1998; Ravindranath et al. 2004; Barden et al. 2005). The average size of massive QGs grows at a faster rate than the size of SFGs and this size growth rate for QGs does not change with redshift (e.g., van der Wel et al. 2014; Mowla et al. 2019b).

Evolution in the concentration of galaxy light profiles with redshift is also evident as both SFGs and QGs change their shapes with cosmic time. At higher redshifts ($z \sim 2$), SFG morphology is in general highly irregular with star-forming clumps (Law et al. 2007; Bournaud & Elmegreen 2009) whereas SFGs have disky structure at lower redshifts (Shen et al. 2003). The concentration of the QG population evolve from a disk dominated (less concentrated) at early epochs ($z \sim 2$, van der Wel et al. 2011) to bulge dominated or elliptical (more concentrated) galaxies today (Shen et al. 2003).

1.2 Processes Driving the Structural Evolution of Galaxies

The growth of galaxy size depends on the history of mass assembly in galaxies. Therefore, by studying the growth in galaxy size and the evolution in the relation between size and stellar mass we can provide constraints to the processes that drive galaxy evolution and associated morphological transformation.

1.2.1 Star-Forming Galaxies

Since the formation of galaxy disks is coupled to the evolution of dark matter halos, a fast evolution in the average sizes of SFGs is expected (Mo et al. 1998). Such fast evolution in SFG sizes in pace with the growth of halos is supported by the observations at higher redshifts ($2 < z < 6$, Ferguson et al. 2004; Oesch et al. 2010; Mosleh et al. 2012). However, the slow evolution or lack of evolution at lower redshifts ($z < 1$) points towards a more complicated evolutionary scenario (Lilly et al. 1998; Ravindranath et al. 2004; Barden et al. 2012; van der Wel et al. 2014). Hence, a more comprehensive investigation into this redshift range ($z < 1$) is required to understand the physical mechanisms driving the size evolution of SFGs.

A possible reason for the change in the pace of the size evolution of SFGs is the *growth of bulges* with cosmic time (e.g., Oser et al. 2010; Hopkins et al. 2010; Tacchella et al. 2015; Sachdeva et al. 2017). Since bulges are more centrally concentrated than disks, they are relatively smaller in size. Thus, the size (radius) of an SFG at a fixed mass decreases as it becomes more bulge dominated. Bulge growth in galaxies can happen internally (secular or slow evolution, Kormendy & Kennicutt 2004; Athanassoula 2005; Kormendy 2008; Ceverino et al. 2010; Sellwood 2014) and/or can be induced externally through galaxy interactions (e.g., Naab et al. 2006; Hopkins et al. 2010).

1.2.2 Quiescent Galaxies

Several processes can contribute towards the evolution of quiescent galaxy sizes and the size-mass relation of the quiescent population. A significant contributor is the *progenitor bias*, which refers to the fact that newly quenched galaxies are larger in size than those quenched at earlier epochs. This difference is due to the upsizing or the increase in the median size of their progenitor SFGs with time (Franx et al. 2008; Carollo et al. 2013; Fagioli et al. 2016; Damjanov et al. 2019).

Fading of disk once a galaxy is quenched can also affect the size evolution of QGs. As the star formation in a galaxy ceases, its disk component gradually fades away (Christlein & Zabludoff 2004; Carollo et al. 2016). This fading of disks happens as massive stars in the former star-forming regions die and the bulge dominance increases during this fading process. The bulge dominance caused by the fading of disks in the galaxy light profile results in smaller effective sizes of galaxies.

Another internal process that affects the morphological evolution of QGs is the *adiabatic expansion* of galaxies. In the adiabatic expansion (puffing-up) model, feedback processes destabilise the inner regions of galaxies where baryons dominate. These feedback processes include AGN feedback (Fan et al. 2008, 2010) and stellar feedback (e.g., supernovae, Baumgardt & Kroupa 2007; Damjanov et al. 2009; Lapi et al. 2018). As a galaxy loses mass through a feedback mechanism, its gravitational potential becomes shallower. Consequently, the baryonic matter, including stars, rearranges itself to a more relaxed stable configuration. This rearrangement of baryonic material results in puffing up of galaxies. Several numerical simulations show that a galaxy loses a fraction of its mass through stellar feedback processes, which results in the adiabatic expansion (Boily & Kroupa 2003; Goodwin & Bastian 2006; Baumgardt & Kroupa 2007; Damjanov et al. 2009; Moeckel & Bate 2010).

Galaxy mergers can efficiently increase the size of QGs with time (Toomre & Toomre 1972; Di Matteo et al. 2005; Cox et al. 2006). Mergers can be either wet (gas rich) or dry (gas poor). A wet merger can rejuvenate star formation in galaxies and thus, does not contribute to the size growth of QGs. Dry *major mergers*, where the masses of the interacting galaxies are similar, are known to produce larger QGs (Kaviraj et al. 2014). Such mergers can yield an increase in size proportional to the increase in mass (eg., Boylan-

Kolchin et al. 2006; Naab et al. 2007; Bezanson et al. 2009). However, dry major mergers may not be significantly affecting the size-mass relation of massive QGs as the number of such events observed since $z \sim 1$ is low (Bundy et al. 2009; López-Sanjuan et al. 2010a,b; Kaviraj et al. 2014).

At the same time, *minor mergers*, where the ratio of masses of the interacting galaxies is more than 10:1, and *accretion* of *ex-situ* stellar population through tidal stripping of satellite galaxies, happen more frequently than major mergers (Newman et al. 2012). Theoretical studies and simulations show that massive QGs grow in size through minor mergers and accretion (e.g., Khochfar & Silk 2006; Naab et al. 2009; Oser et al. 2010, 2012; Hilz et al. 2012; Rodriguez-Gomez et al. 2016), which is supported by observations (e.g., Bezanson et al. 2009; van Dokkum et al. 2010; Trujillo et al. 2011; Fagioli et al. 2016; Sawicki et al. 2020). These processes add material to the outskirts of galaxies resulting in a large increase in size and a modest increase in mass: the growth in size due to minor mergers is proportional to the square of the mass added (Bezanson et al. 2009; Naab et al. 2009; Coccato et al. 2011). Assuming a short merger timescale (~ 1 Gyr) based on numerical simulations, Newman et al. (2012) argue that the minor mergers can explain most of the size evolution of massive QGs at $z < 1$ using observations of galaxy pairs to estimate the number of minor mergers and constrain their effects on the size growth of QGs.

1.2.3 Environment and Galaxy Morphology

Galaxy morphology and the number density of galaxies are related; for example, quiescent spheroidal galaxies are a larger fraction of galaxy population in denser regions than in the field. Thus, environment is understood to play a vital role in the evolution of galaxies (e.g., Dressler 1980; Farouki & Shapiro 1981; Rettura et al. 2010; Muzzin et al. 2012; Lani et al. 2013; Scoville et al. 2013; Peng et al. 2010b, 2015; D'Onofrio et al. 2015; Balogh et al. 2016; Carollo et al. 2016; Kawinwanichakij et al. 2017; Schaefer et al. 2017; Golden-Marx & Miller 2019; Chartab et al. 2020). There are mainly two ways a dense environment can affect galaxy evolution and associated morphological transformation: enhancing quenching of star formation in galaxies and aiding galaxy-galaxy interactions.

Environment contributes towards the progenitor bias in the size-mass relation of the QGs by suppressing star formation activities in galaxies. Several processes related to the environment can halt (quench) star formation in galaxies. *Ram pressure stripping* is thought to be a common process that quenches star formation in galaxies residing in clusters. As an SFG falls into a cluster environment, its interstellar medium (ISM) is stripped away by the pressure exerted by intracluster medium (ICM), forming a tail of gas behind the galaxy (Gunn & Gott 1972; Mayer et al. 2006; Jáchym et al. 2007; D'Onofrio et al. 2015; Mehmood 2017; Sohn et al. 2019). Although ram pressure can sometimes cause a starburst event by extreme compression of the ISM (Ebeling et al. 2014), quenching of star formation is accelerated as the ISM is either removed or heated by ram pressure. This ram pressure experienced by an in-falling galaxy is

$$P_{\mathrm{ram}} \approx \rho_{\mathrm{ICM}} v^2, \tag{1.2.1}$$

where ρ_{ICM} is the density of ICM and v is the velocity of the galaxy relative to the ICM (Sohn et al. 2019). Therefore, the efficiency of ram pressure stripping depends heavily on the local density. Since the density of ICM increases towards the cluster centre, we expect increased impact of ram pressure stripping on galaxies observed in the cluster cores. The stripping of gas from galaxies occurs only if the ram pressure exceeds the restoring gravitational force in galaxies,

$$F = \Sigma_{\mathrm{gas}} v_{\mathrm{rot}}^2 R_{\mathrm{disk}}^{-1}, \tag{1.2.2}$$

where Σ_{gas} is surface gas density, v_{rot} is rotational velocity of the disk and R_{disk} is the radius of the disk (Sohn et al. 2019). Because the restoring gravitational force per unit area decreases with radial distance from the galaxy centre, ram pressure stripping is stronger towards galaxy outskirts. Ram pressure stripping also depends on the morphology and the angle of inclination of the infalling galaxies. For example, the effect of ram pressure will be stronger for a disky galaxy if it falls face-on compared to an edge-on infall.

Another environmental galaxy quenching process that works along with ram pressure stripping is *strangulation* or cosmological starvation, in which galaxies are devoid of their cold gas reservoirs. Dense environments can hinder the inflow of cold gas into galaxies because the outer gas reservoirs are stripped off from a galaxy (Balogh et al. 2000; Peng et al. 2015). Without the inflow of gas, star-forming activities are quickly suppressed as a galaxy consumes remaining cold gas left within the system (over-consumption, Balogh et al. 2016). Studies show that this quenching process becomes more prominent with cosmic time (e.g., van de Voort et al. 2017).

Additionally, dense environments rich in galaxies promote galaxy-galaxy interactions. In highly dense environments such as clusters, the average velocities of galaxies are larger than their internal velocity dispersions. Hence, most of the interactions are high speed non-collisional galaxy encounters. Galaxy *harassment* is a cumulative effect of frequent high speed galaxy encounters (Farouki & Shapiro 1981; Aguilar & White 1986; Moore et al. 1996; Mehmood 2017). Such frequent encounters can result in significant mass loss in galaxies. Moreover, if the galaxy-galaxy interaction is strong, it will perturb the galaxy disks. In such scenarios, the disk will become dynamically hot and stellar orbits will be rearranged into random fashion resulting in a spheroid or an elliptical galaxy with a puffed up morphology. Harassment is more efficient in puffing up galaxies with lower masses (and thus shallower potential wells). Consequently, harassment, in general, yields low mass dwarf spheroidal galaxies. In galaxies with larger disks, the harassment often results in the funnelling of the baryonic material towards the centre of the galaxy, contributing to the formation and growth of bulges in these systems. This growth of bulges will yield a reduction in galaxy sizes and more concentrated light profiles.

Tidal stripping, another type of non-collisional galaxy interactions, also causes mass loss and morphological change in galaxies (Ferguson & Binggeli 1994; Mayer et al. 2006; Oser et al. 2010, 2012). In this process, a host galaxy gravitationally pulls out stellar materials from the outer regions of its satellite, which often results in tidal debris left behind. Depending on the masses of the host and the satellite galaxies and the distance between them, the process can strip a galaxy of its disk and outer regions completely, only leaving behind a red bulge at the centre. Similar to harassment, tidal stripping also yields spheroidal morphology in galaxies due to bulge dominance. Furthermore, the stripping process can also cause puffing up of galaxy as it loses mass.

Some dense environments can also support collisional galaxy interactions - *mergers*. Considering that the galaxies in the denser regions are generally QGs, most of the merging events in rich environment are dry mergers. Merger events are common in galaxy clusters at higher redshifts ($z \gtrsim 1$; e.g., Contini et al. 2016; Sawicki et al. 2020) and galaxy groups but rare in cluster cores at lower redshifts ($z \lesssim 1$) because of the larger orbital velocity of galaxies in the cluster cores. However, a particular type of minor mergers does happen in the cluster cores at lower redshifts ($z \lesssim 1$): galaxies in the core merge with brightest cluster galaxies (BCGs) by spiralling into it as they lose orbital energy due to dynamical friction. This type of minor mergers, *galactic cannibalism*, causes the disappearances of galaxies as they move towards the cluster centre (Hausman & Ostriker 1978; Duncan et al. 1983; Blakeslee & Tonry 1992; Weinberg 1997; Nipoti et al. 2003, 2004; Chen 2019).

To estimate the impact of environment on galaxy morphology and its evolution, we must study galaxy clusters. Within clusters, the effects of many processes listed above are expected to become more prominent as the density of the environment increases. Several studies that focus on cluster cores support the role of the densest environments in the quenching mechanism and morphological evolution of galaxies (e.g., Gutiérrez et al. 2004; Burke et al. 2013; Monna et al. 2015; Castignani et al. 2020). Since cores of galaxy clusters represent extremely dense regions in the Universe, morphological study of galaxies in cluster cores along with galaxies residing in less dense regions (field) is required to distinguish between the effects of different physical processes that affect galaxy transformation in different environments.

1.3 Motivation and Goal of this Thesis

We intend to investigate the morphological evolution of SFGs and QGs and the effects of the environment using data from CFHT Large Area U-band Deep Survey (CLAUDS; Sawicki et al. 2019) and the Hyper Suprime-Cam Subaru Strategic Program (HSC-SSP; Aihara et al. 2019) over a large sky area of 18.6 deg^2 in six broadbands, U, g, r, i, z and y that cover the wavelength range of $\sim 3000-10000\,\AA$. We focus our study on galaxies in the redshift range $0.1 < z < 0.9$. This dataset is a unique combination of wavelength coverage and depth that enables us to study details of galaxy morphological transformations and their connection to the physical processes that drive galaxy evolution over a time period which covers half of the cosmic history. Such a large-scale study of galaxy morphology and evolution over this redshift range will be unprecedented. Moreover, we study cluster members as well as galaxies in the field, testing the processes that drive morphological transformation of galaxies in different environments.

This thesis is a pilot study that focuses on 1.6 deg^2 of the COSMOS/UltraVISTA region in CLAUDS+HSC-SSP data using the HSC g, r, i and z bands. We investigate how the relation between galaxy stellar mass and size evolves for both SFGs and QGs since $z = 0.9$ and test a suite of processes that may drive this evolution. We address the environmental effects by looking at the morphology of galaxy cluster members in this region on the sky and by incorporating the morphology of galaxies from the cores of five clusters at $0.18 < z < 0.29$ using data from Cluster Lensing And Supernova survey with Hubble (CLASH, Postman et al. 2012), a Hubble Space Telescope (HST) based programme. Spectroscopic information on these HST CLASH galaxies provides us with the confirmation that galaxies are true members of cluster cores and the proxy for the average age of their stellar populations. Galaxy morphology in cluster cores should be particularly affected by physical processes that dominate in the densest regions of the cosmic web. Thus, our spectro-photometric sample enables us to probe morphological transformation of galaxies and the processes that drive it at the high-density tail of the local galaxy density distribution.

We structure this thesis as follows. We describe the data images and the data products used in Chapter 2, and the sample selection in Chapter 3. Chapter 4 describes the methods used to measure the galaxy morphology from data images. We describe the estimation of uncertainties in the measured structural parameters using simulations in Chapter 5. We show the results from this study and compare our results with previous studies in Chapter 6. Chapter 7 is a discussion of some of the features of the results and the physical processes that cause these features. Chapter 8 gives the conclusions of this thesis. Throughout this thesis, we assume a ΛCDM cosmology with present-day $\Omega_{\rm M} = 0.3$, $\Omega_\Lambda = 0.7$ and $H_0 = 68$ km s^{-1} Mpc^{-1}.

Chapter 2

Data

2.1 CLAUDS+HSC-SSP Survey

Several factors have influenced the selection of data for this study. Firstly, it is necessary to have a deep survey in order to carry out this study effectively. A deep survey helps to constrain the measurement of morphology of a galaxy such as its size. The survey depth is also a major factor which determines the lower limit in galaxy stellar mass above which our sample is complete (Section 3.1.1). Secondly, the availability of multi-wavelength data is important. Since various physical parameters (stellar mass, redshift, etc.) of galaxies are derived from the multi-wavelength data, it is better to use a survey with wide wavelength coverage. Thirdly, choosing a widely studied survey region in the sky is beneficial as we can compare the results of this thesis with those of previous and parallel studies. This

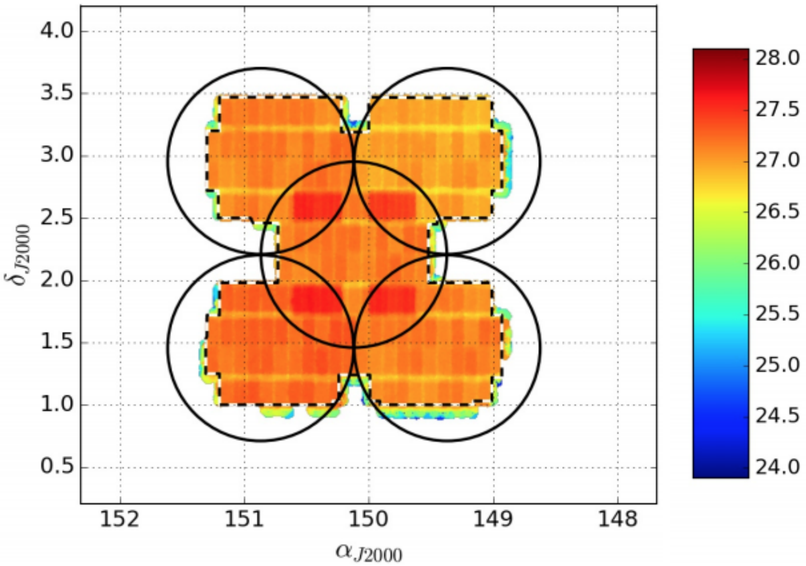

Figure 2.1: *u* band depth and areal coverage of CLAUDS E-COSMOS field. The colours indicate the depth of *u* band in AB. Black circles represent the areal region covered by HSC-SSP *grizy* data. Dashed lines show the extent of the CLAUDS Deep data and also the extent of the current study. Image credits: Sawicki et al. (2019, used with permission).

approach aids us not only to ensure quality control of certain steps implemented in this project, but also to draw scientific conclusions regarding the physical processes driving the observations with better certitude.

Additionally, a survey region with rich ancillary data including spectroscopy is indeed an asset towards our scientific goals. Firstly, spectroscopic data alone can provide precise information about galaxy distance that is critically important for selecting cluster members. Secondly, spectroscopic measurements such as velocity dispersion and line indices provide the information about the depth of galaxy potential well, and break the degeneracy between estimates of various stellar population properties (e.g., age and metallicity, Vazdekis 2008).

Considering the above mentioned factors, we choose to concentrate our study on Cosmic Evolution Survey (COSMOS) field, a well studied region in the sky for galaxy morphology and evolution. It covers an area of ~ 2 square degree equatorial field with extensive multi-wavelength data ranging from X-rays to infrared region of the electromagnetic spectrum coming from various major telescopes such as the Hubble Space Telescope (HST), the Chandra X-ray Observatory, the XMM-Newton Observatory, the National Optical Astronomy Observatory (NOAO), the Canada–France–Hawaii Telescope (CFHT) and the Subaru Telescope (Scoville et al. 2007).

We use the multi-wavelength ($U + grizy$) imaging data from CFHT Large Area U-band Deep Survey (CLAUDS; Sawicki et al. 2019) and the Hyper Suprime-Cam Subaru Strategic Program (HSC-SSP; Aihara et al. 2019). Subaru's HSC-SSP survey consists of three layers of data: wide, Deep and UltraDeep, in five broadband filters (g, r, i, z, y) and four narrowband (NB) filters ($\lambda = 387, 816, 921, 1010\,\mathrm{nm}$). The Deep layer covers an area of 26 deg^2 in four fields: XMM-LSS, E-COSMOS (Extended-COSMOS), ELAIS-N1, DEEP2-F3. The UltraDeep layer covers a region of 4 deg^2 in two fields: COSMOS and the Subaru/XMM-Newton Deep Survey (SXDS). Since Deep and UltraDeep data are both deep and wide, they are optimal for the study of galaxy properties and their evolution over cosmic time and in different environments. However, one of the drawbacks of HSC-SSP survey is that it lacks U-band data, which is important for constraining photometric redshifts and other galaxy properties. For example, U-band photometry is essential for bracketing the Balmer and 4000 Å breaks in order to estimate photometric redshifts (photo-z's) accurately for

Table 2.1: CLAUDS+HSC-SSP filter details. CLAUDS U-band consists of filters u and u^* and their depth is given for the Deep layer. For the HSC-SSP filters, Deep+UltraDeep depth achieved so far is shown. As the survey completes HSC-SSP bands will have better depths. All of these are 5σ depths for extended sources within $2''$ apertures.

Filter	Survey	Layer	Central Wavelegth [nm]	Seeing [arcsec]	Depth [AB mag]
U	CLAUDS	Deep	353.8	0.92	27.1
g	HSC-SSP	Deep+UltraDeep	475.4	0.81	27.0
r	HSC-SSP	Deep+UltraDeep	617.5	0.74	26.6
i	HSC-SSP	Deep+UltraDeep	771.1	0.62	26.4
z	HSC-SSP	Deep+UltraDeep	889.8	0.63	26.0
y	HSC-SSP	Deep+UltraDeep	976.2	0.71	25.0

galaxies at intermediate redshifts ($0 < z <\sim 0.7$, Sawicki et al. 2019). At these intermediate redshifts, U-band data also plays a vital role in constraining star formation rates (SFRs) of galaxies (Sawicki 2012). As a solution to these problems, CLAUDS survey, using the MegaCam Imager of CFHT, covers 18.6 deg^2 in the HSC-SSP Deep layer in U-band with a median depth of 27.1 AB (5σ in $2''$ apertures). The depth reaches 27.7 AB for a region of 1.36 deg^2 in the UltraDeep layer. The MegaCam has two U-band filters: u and u^*. The main advantages of the new u filter over the old u^* filter are better throughputs and larger collecting area (u filter is physically larger and can illumine more CCDs). Thus, we have data from all five HSC-SSP broadband filters and CLAUDS u band filter from the overlapping regions in E-COSMOS as shown in Figure 2.1. Figure 2.2 shows the broadband filters available in CLAUDS+HSC-SSP Survey and their details are given in Table 2.1.

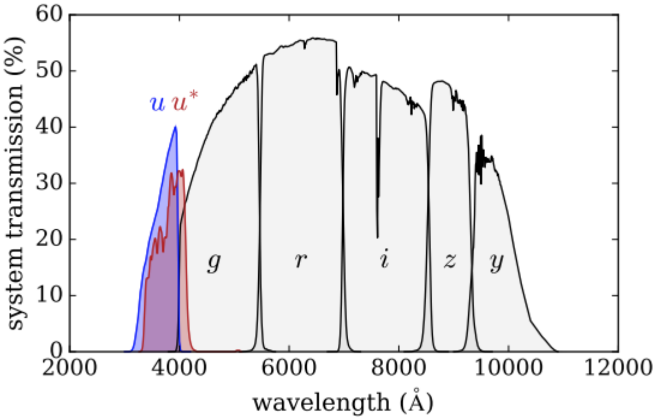

Figure 2.2: System transmission curves of filters available in CLAUDS+HSC-SSP. Image credits: Sawicki et al. (2019, used with permission).

2.1.1 Images

Aihara et al. (2019) and Sawicki et al. (2019) describe in detail the data reduction processes for HSC-SSP and CLAUDS respectively. HSC-SSP data are divided into tracts ($\sim 1.5 \times 1.5$ deg^2) and each tract consists of 9×9 patches. Each image patch consists of 4200×4200 pixels where each image pixel covers $\sim 0.168'' \times 0.168''$ of the sky. These image patches are processed using the HSC Pipeline (Bosch et al. 2018) which involves image coaddition, source detection and global sky subtraction. The algorithm also clips the artefacts detected before creating image coadditions.

CLAUDS uses the MegaPipe data pipeline (Gwyn 2008) at the Canadian Astronomical Data Centre (CADC) with some modifications. The charge-coupled device (CCD) detectors in MegaCam measure 2048×4612 pixels with each pixel corresponding to $0.187'' \times 0.187''$ on the sky. Therefore, the pipeline re-scales the data images to conform to the HSC data.

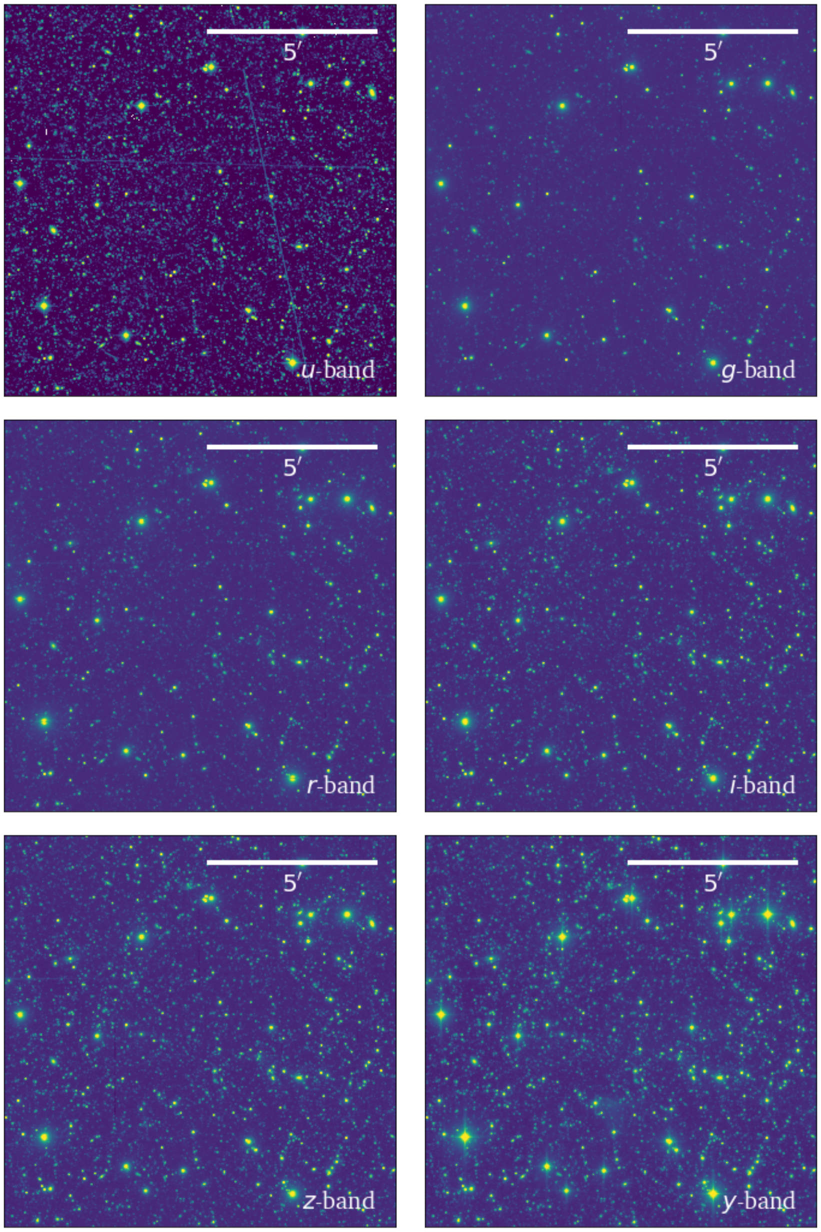

Figure 2.3: CLAUDS+HSC-SSP images of patch: 4,3 from tract: 9814 in u, g, r, i, z and y. Top row: u, g; middle row: r, i; bottom row: z, y. Each image has a dimension of $\sim 1.5^o \times 1.5^o$ and have the same intensity stretch.

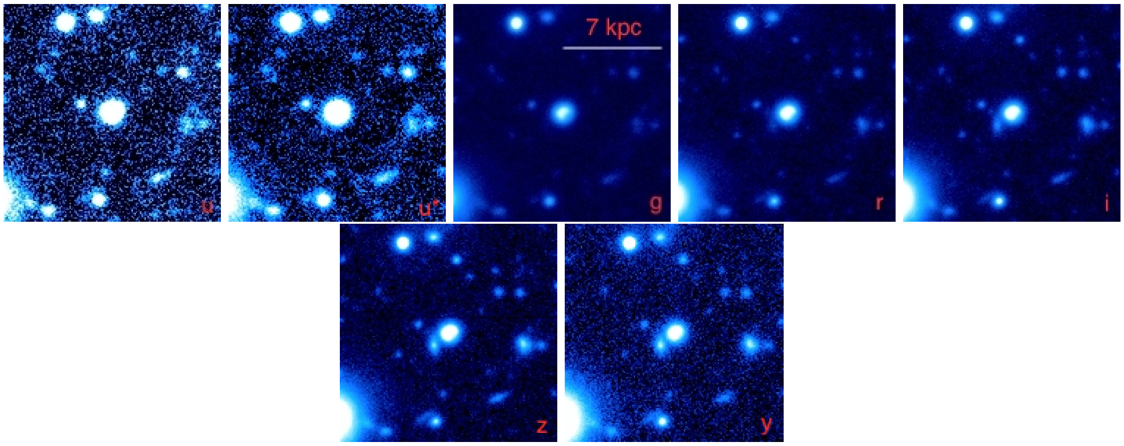

Figure 2.4: CLAUDS+HSC-SSP images of a galaxy at coordinates (α: 150.17897, δ: 2.03213) in u, $u*$, g, r, i, z and y. Image cutouts are of dimensions $\sim 25'' \times 25''$ and have the same intensity stretch.

The rest of the processing is performed similarly to the HSC pipeline. Figures 2.3 and 2.4 show images of a CLAUDS+HSC-SSP tract and a sample galaxy respectively in different broadbands.

Sources in the images have been detected by Sawicki et al. (2019) using SExtractor (Source Extractor) algorithm (Bertin & Arnouts 1996). Additionally, we adopt star-galaxy separation results from Golob et al. (submitted to MNRAS), who identified foreground stars in the images using an algorithm based on machine learning they have developed. This algorithm makes use of photometric and morphological information on detected objects. The algorithm uses a gradient boosted tree (GBT) machine classifier trained on the HST COSMOS morphological catalogue by Leauthaud et al. (2007) to classify objects in CLAUDS+HSC-SSP using their $U + grizy$ magnitudes, colours, central surface brightnesses, and effective radii corrected for PSF (Section 4.3, Moutard et al. 2020). We identify any object for which the classifier returned a value greater than 0.89 as a star.

The image of a point source is blurred out due to the diffraction of light and other factors like atmospheric turbulence (seeing). A point-spread function (PSF) describes this blurring of an image of a point source. It describes the shape of the brightness profile of astronomical point sources like stars as seen on the detector of a telescope. Thus, the full width at half maximum (FWHM) of the PSF is an indicator for the resolution of the image; the smaller the size/width of a PSF, the better the resolution of an image.

The HSC Pipeline uses the PSFEx algorithm[1] (Bertin 2011) to describe the PSF of data images and these PSFs are made using the stars identified from the data. The PSFex adaptation in the HSC Pipeline models PSF from the images of these stars in an iterative way to remove the influence of contamination from neighbouring objects (Bosch et al. 2018). PSFs of any position in the data images are available through the PSF picker[2] utility in the Public Data Release by HSC-SSP. PSF images obtained from PSF picker for all five broadbands at coordinates ($\alpha : 150.1989, \delta : 1.9957$) are shown in Figure 2.5. These PSF images have dimensions $\sim 7.2'' \times 7.2''$ which are big enough to contain the wings of the PSF ($\sim 10\times$ FWHM, Table 2.1).

Although PSFs for every sky coordinate are available through PSF picker, fetching PSFs for every galaxy would be computationally expensive. Hence, we divide every patch into 36 sub-regions of dimensions $117.6'' \times 117.6''$. For all galaxies within a sub-region, we use

---

[1] `http://ascl.net/1301.001`

[2] `https://hsc-release.mtk.nao.ac.jp/psf/pdr2/`

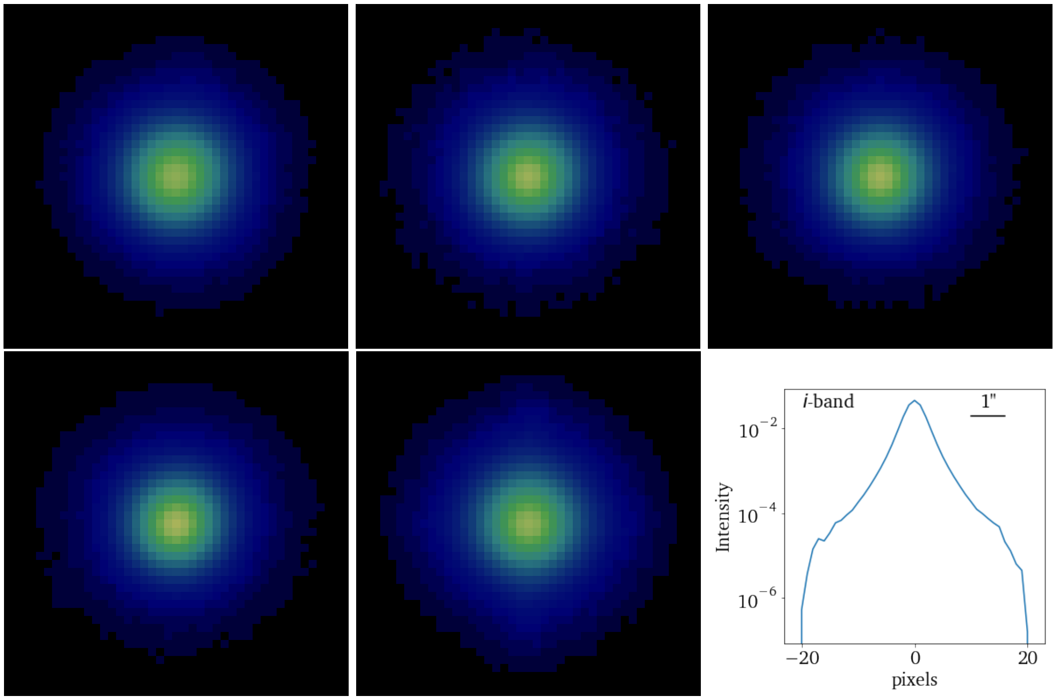

Figure 2.5: PSF images of coordinates (α : 150.1989, δ : 1.9957) which falls in tract: 9814 & patch: 4,3 in g, r, i, z and y bands as obtained from PSF picker. The final panel shows the 1-D profile of the i-band PSF.

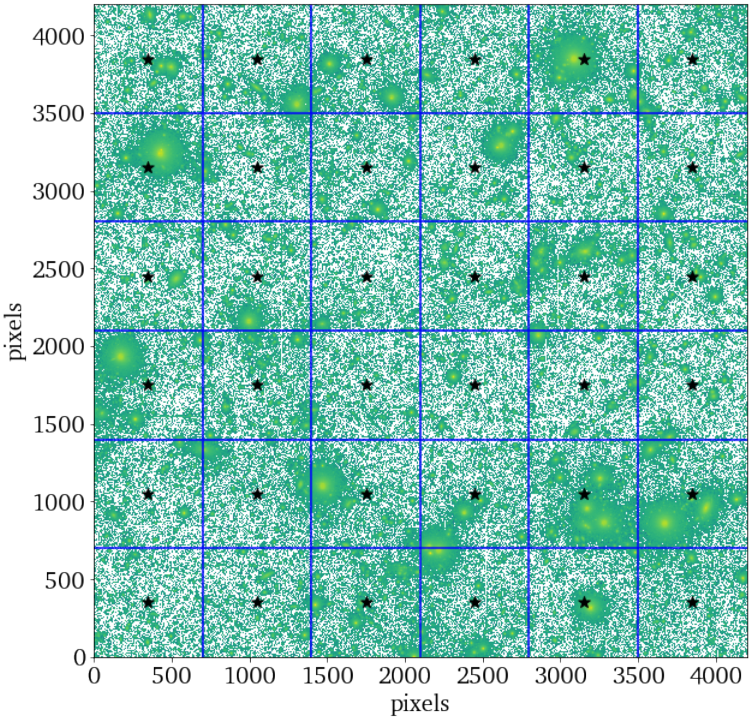

Figure 2.6: *i*-band image of tract-9813 & patch-4,3 divided into 36 sub-regions of size $117.6'' \times 117.6''$ (700 pixels × 700 pixels). The positions of PSFs picked for each sub-region is shown as black stars.

the PSF image at the centre of this region. An example of how this is done in a patch is demonstrated in Figure 2.6.

2.1.2 Available Data Products

We have access to spectroscopic redshifts of only ~ 5000 galaxies which consists less than 20% of the current data (Lilly et al. 2009). Therefore, we use photometric redshifts from a K_s-selected catalogue (Muzzin et al. 2013a) covering 1.62 deg^2 in the COSMOS/UltraVISTA field. This catalogue is based on PSF-matched photometry in 30 photometric bands ranging from 0.15 μm to 24 μm based on GALEX, Subaru, CFHT, VISTA and Spitzer data. The catalogue has 90% completeness limit at $K_s = 23.4$ AB. Photometric redshifts (photo-zs) in the K_s-selected catalogue are calculated using the EAZY software (Brammer et al. 2008), a spectral energy distribution (SED) fitting algorithm. The detailed process of photometric redshift estimation is given in Skelton et al. (2014). The peak of the probability density distribution of the photometric redshift obtained from EAZY by fitting the SED of a galaxy with a linear combination of galaxy stellar population synthesis model templates is used as the photo-z of a galaxy. Since some of the galaxies have spectroscopic redshift measurements from zCOSMOS (Lilly et al. 2007, 2009), EAZY measurements are tested and calibrated by matching to 5105 highest-confidence spectroscopic redshifts.

Stellar masses of galaxies are taken from the K_s-selected catalogue (Muzzin et al. 2013a) for the COSMOS/UltraVISTA field. Galaxy stellar masses in this catalogue are estimated using the FAST code (Kriek et al. 2009) through SED flux fitting using two stellar population synthesis model sets (Bruzual & Charlot 2003; Maraston 2005) assuming exponentially declining star formation history (SFH, star formation rate $\propto e^{-t/\tau}$), solar metallicity, a Chabrier initial mass function (IMF, Chabrier 2003) and a Calzetti dust extinction law (Calzetti et al. 2000). An advantage of FAST is that it can be used in combination with EAZY whereupon it returns best-fitting stellar mass and redshift along with other parameters such as SFR. If the redshift is provided, it fixes the redshift to the closest value in the grid during the fitting process. FAST uses χ^2 statistics to estimate the parameters (Section

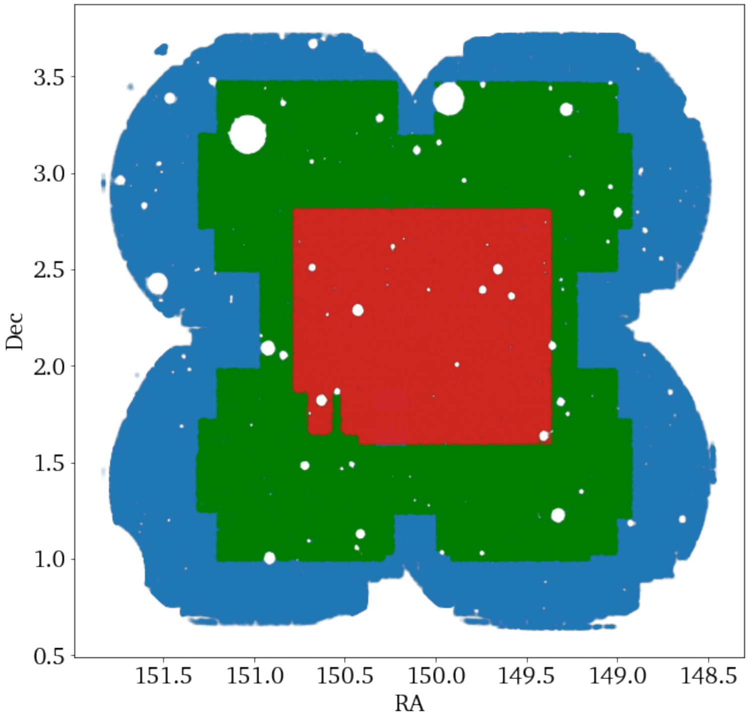

Figure 2.7: Region of the sky studied in this Thesis. COSMOS/UltraVISTA field is shown in red. Photometric redshifts and mass measurements from Muzzin et al. (2013a) are used for the analysis in this region. On the background, we have shown CLAUDS+HSC-SSP COSMOS field (green) and the whole HSC COSMOS field (blue). White circles in the image are regions around bright stars in which photometric measurements are compromised.

4.1).

Thus, we limit this pilot study to the COSMOS/UltraVISTA region in the sky where we have redshift and mass estimations from the K_s-selected catalogue. Figure 2.7 shows the COSMOS/UltraVISTA field in comparison with with the CLAUDS+HSC-SSP region. We also restrict the redshift range of this study to $0.1 < z < 0.9$. We cannot probe galaxies at $z > 0.9$ due to mass incompleteness issues described in Section 3.1.1.

We can study the effects of environment on galaxy morphology, by analysing galaxies in clusters separately. So, we use an optically-selected cluster catalogue (Oguri et al. 2018) based on HSC data to identify clusters in the survey. This catalogue is made using the CAMIRA (Cluster finding Algorithm based on Multi-band Identification of Red-sequence galaxies) algorithm (Oguri 2014). Details of the cluster selection process are described in Section 3.1.3.

2.2 HST CLASH Survey

Cores of galaxy clusters are typically densely populated extreme environments where the effects of environment on galaxy morphology are enhanced. Nevertheless, galaxies in the cluster cores are difficult to study, because their light profiles are contaminated by the light from neighbouring galaxies and intracluster light. The position of the brightest cluster galaxy (BCG) ideally coincides with the centre of a dynamically relaxed cluster. This makes the study of the cluster core all the more difficult because the light from the BCG dominates over other galaxies. Hence, a high resolution data is necessary to study and analyse the morphology of galaxies in these extreme environments. Space-based telescopes such as the HST would be better compared to ground-based telescopes to resolve galaxy light profiles in the cluster centres because, unlike space-based observations, ground-based observations are affected by atmospheric seeing which reduces resolution. HST has a dedicated program to observe cluster cores with significant lensing properties at $z < 0.9$. Named Cluster Lensing And Supernova survey with Hubble (CLASH), it is a deep 16-band HST

Table 2.2: Details of HST CLASH clusters studied in this paper. R_{200} and M_{200} are from Geller et al. (2014) for A383 and of the rest are from Lemze et al. (2013) for the other clusters.

Cluster	RA$_{J2000}$	Dec$_{J2000}$	z_{clust}	R_{200} (caustics) [h^{-1} Mpc]	M_{200} (caustics) [$10^{15}h^{-1}$ M$_{\odot}$]
A383	02:48:03.36	-03:31:44.7	0.187	1.22±0.01	0.51±0.01
A611	08:00:56.83	+36:03:24.1	0.288	1.70±0.26	0.80±0.32
A1423	11:57:17.26	+33:36:37.4	0.213	1.23±0.23	0.28±0.16
A2261	17:22:27.25	+32:07:58.6	0.224	1.36±0.25	0.38±0.23
RXJ2129	21:29:39.94	+00:05:18.8	0.234	1.45±0.22	0.46±0.21

photometric dataset aimed at using the gravitational lensing properties of 25 galaxy clusters to accurately constrain their mass distributions (Postman et al. 2012). The observations were performed using HST's Advanced Camera for Surveys (ACS) and both the UVIS and IR channels of the Wide-Field Camera 3 (WFC3) over a 2.7 year period (Nov 2010 - July 2013). The boadbands of this survey spanning the near-UV to near-IR help us study the cluster cores in wavelengths similar to CLAUDS+HSC-SSP broadbands.

For this study, we choose 5 clusters at cluster redshifts (z_{clust}) ranging from ~ 0.2 to 0.3: A383, A611, A1423, A2261 and RXJ2129. The choice of clusters is due to the availability of spectroscopic data of their members as described in Section 2.2.2. These five clusters have been selected for spectroscopic followup because at least one of them can be observed anytime throughout the year from the MMT Observatory in Arizona. This is illustrated in Figure 2.8 with the aid of a web based program named Staralt[3] by the Isaac Newton Group of Telescopes. Using the Hectospec multifiber spectrograph on MMT, it is possible to get

---

[3] `http://catserver.ing.iac.es/staralt`

spectra of the member galaxies in the entire cluster in a single observation because Hectospec has 300 optical fiber probes with a total field of view (FOV) of ~ 1 deg^2 (Fabricant et al. 2005).

All five clusters are dynamically relaxed systems. A relaxed cluster has not undergone mergers in the recent past, and in such a cluster, gas and galaxies are both virialised: $2K = -U$, where K is kinetic energy and U is potential energy. An important cluster scale is the virial radius of a cluster, which is often approximated to R_{200}. R_{200} denotes the radius of a galaxy at which its density equals 200 times the critical density of the Universe at its redshift and M_{200} is the mass enclosed within R_{200}. Table 2.2 gives the details of the five chosen clusters, their sky coordinates, redshifts and cluster scales (M_{200} and R_{200}). The cluster scales are estimated using the caustic method (Diaferio & Geller 1997). In a phase space defined by projected distance from the cluster centre and line-of-sight velocity relative to the centre, cluster galaxies form sharply defined patterns in the shape of a trumpet. The caustics boundary of this trumpet shape is defined by the escape velocity of galaxies from the cluster. Because the escape velocity depends on the cluster mass which provides gravitational pull, we can utilize caustics to estimate the mass of a galaxy cluster. Unlike the projected mass technique, caustic mass is insensitive to line-of-sight superposed structures (Geller et al. 2013). Although caustic technique makes an assumption of spherical mass distribution for galaxy clusters, this assumption may be justified for the five clusters included in this study as they are relaxed systems.

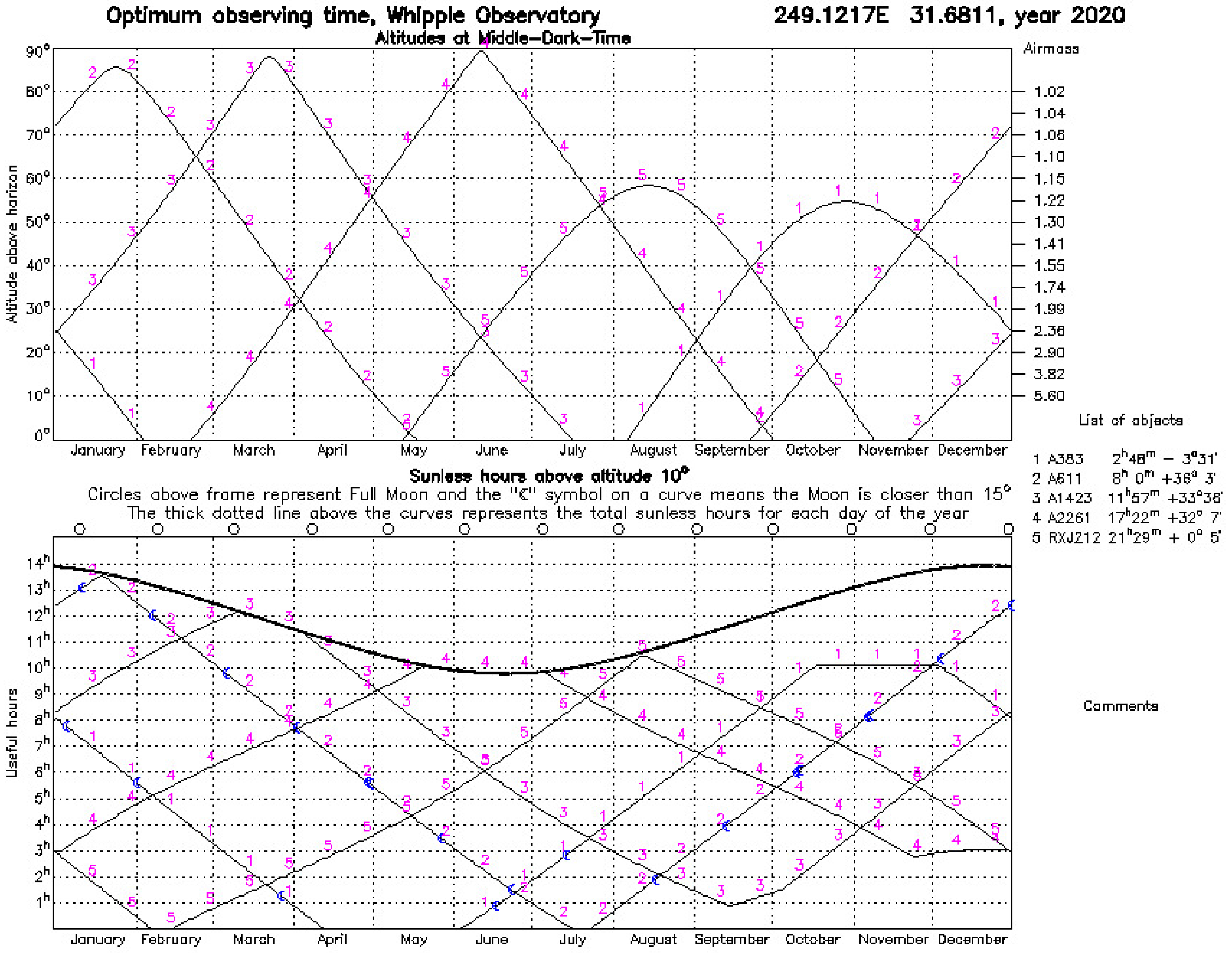

Figure 2.8: Visibility of the five HST CLASH clusters chosen in this study from MMT, Arizona, throughout the year.

2.2.1 Images

We use observations in the f814w band from ACS with a scale length of $0.03''$. It has a 5σ magnitude limit of 27.7 AB for a circular aperture of $0.4''$ in diameter. The details of the data reduction process is described in the CLASH survey paper by Postman et al. (2012). In short, these data images are created by co-aligning and co-adding the observational data using drizzle algorithms (MultiDrizzle pipeline; Koekemoer et al. 2006). Each cluster is observed in two different orientations with a rotation of $\sim 30^o$.

PSF images are available through Tiny Tim (Krist et al. 2011), a software package for generating HST PSFs written in the C language. Incorporating the known aberrations and obscurations of the HST instruments, Tiny Tim simulates a PSF model through diffraction calculation combined with the effects of obscuration and optical aberrations. The software considers the time and date of observation, because HST experiences time-and-altitude-dependent aberration changes resulting in defocus. In this study, we use a 5 times subsampled PSF generated by Tiny Tim with a pixel scale of $\sim 0.01''$ and dimensions $\sim 7.15'' \times 7.15''$ for HST CLASH clusters. Figure 2.9 shows the f814w PSF produced by the Tiny Tim software.

2.2.2 Available Data Products

Photometric redshifts of all galaxies in the HST images are available through HST CLASH cluster catalogues (Postman et al. 2012). Redshifts are provided for galaxies detected us-

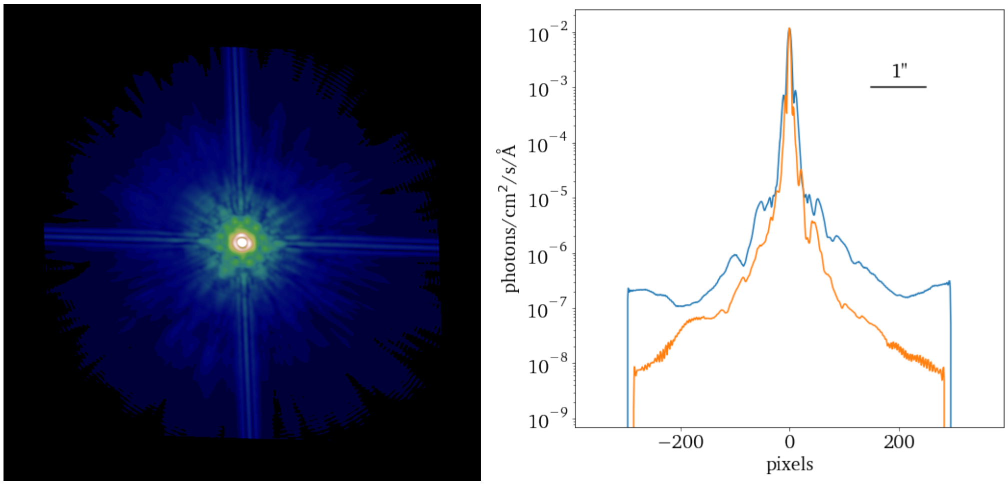

Figure 2.9: Subsampled f814w PSF used for HST CLASH clusters' data. Left: 2-D image of the PSF. Right: Blue shows the 1-D profile along the horizontal axis passing through the centre of the 2-D image and orange is along its diagonal.

ing SExtractor. These redshifts and associated uncertainties are calculated using Bayesian Photometric Redshift (BPZ; Benítez 2000; Benítez et al. 2004; Coe et al. 2006) estimates. We have spectroscopic redshifts for a subset of galaxies in selected HST cluster cores measured using data obtained with the MMT Hectospec multifiber spectrograph (Fabricant et al. 1998). Damjanov et al. (2018) describes the data reduction and redshift measurement procedure in detail. In short, data reduction is performed with HSRED v2.0[4], developed by the Telescope Data Center, which is a revision of the original IDL pipeline by Richard Cool. Spectroscopic redshifts are then estimated by fitting the observed spectra of galaxies using the template spectra library from Kurtz & Mink (1998), which returns a relative amplitude of the cross-correlation peak (r-value; Tonry & Davis 1979), as a measure of the quality of the redshift. These r-values are used to determine whether to use the spectroscopic redshift

---

[4] `http://www.mmto.org/hsred-reduction-pipeline/`

of a given galaxy.

We also have membership details of some of the galaxies (for which we have spectroscopic data) in the images of these five cluster cores based on a friends-of-friends (FoF) algorithm developed by Sohn et al. (2018). Using HectoSpec survey data, Sohn et al. (2018) adopt a standard FoF algorithm which connects neighbouring galaxies with separate spatial and radial velocity linking lengths. If these lengths are smaller than a fiducial length, the algorithm identifies them as friends (neighbours). The FoF algorithm identifies a total of 1605 member galaxies across these clusters out of which we study 139 galaxies that are at the cluster cores covered by the CLASH survey.

Additionally, we have stellar masses of galaxies that are spectroscopically confirmed cluster members. The mass estimation procedure is described in Damjanov et al. (2018). In short, the LePhare code (Arnouts et al. 1999; Ilbert et al. 2006) is used to estimate the stellar mass of a galaxy by fitting its observed photometry applying Bruzual & Charlot (2003) population synthesis models, assuming a Chabrier IMF and Calzetti dust extinction law. Three different metallicities ($Z = 0.004$, 0.008, and 0.02) and exponentially declining SFHs with e-folding times of $\tau = 0.1$, 0.3, 1, 2, 3, 5, 10, 15 and 30 Gyr are assumed while fitting the data. The code constrains the stellar mass-to-light (M/L) ratio using SED shape obtained from observed photometry and converts luminosity to stellar mass.

Chapter 3

Sample Selection

3.1 CLAUDS+HSC-SSP Survey

Since we study galaxy morphology as a function of stellar mass, we need to ensure that the mass distribution of the sample selected in the current work represents the distribution for the real galaxy population (mass completeness). The completeness of the sample can be studied by addressing the selection bias present in the detection of objects in the survey. In magnitude-limited observations, intrinsically brighter objects are over-represented (Malmquist bias, Malmquist 1922, 1925). As the distance increases, the apparent magnitude of the objects becomes fainter. Hence, we lose an increasing number of objects fainter than the magnitude limit of the survey with increasing distance/redshift. This loss of fainter objects also affects the mass distribution of galaxies in the sample, because galaxy stellar mass and luminosity are closely related (M/L ratio, Schechter 1980; Schombert et al. 2019). Consequently, the sample may not reflect the real distribution of galaxies in the field covered by the survey. So, it is important to identify a limit in the stellar mass of galaxies above which our sample is complete.

3.1.1 Redshift and Stellar Masses

We examine the completeness of the survey as a function of stellar mass of galaxies at different redshifts for both star-forming galaxies (SFGs) and quiescent galaxies (QGs) separately. A separate analysis for SFGs and QGs is required because SFGs and QGs have different M/L ratios (e.g., Schechter 1980; McGaugh & Schombert 2014). The upper panel in Figure 3.1 shows the mass completeness of SFGs and QGs at $0.2 < z < 0.4$ and $0.8 < z < 1.0$. The curves in the figure are obtained by fitting a Sigmoid function to the completeness obtained by Golob et al. (in prep.) through simulations. At $z \sim 0.3$, the SFG sample is 90% complete at $\sim 10^{8.6}$ $M_\odot$ and above, whereas at $z \sim 0.9$, 90% completeness limit is at $\sim 10^{9.3}$ $M_\odot$. Similarly, this limit is at $\sim 10^{9}$ $M_\odot$ and $\sim 10^{10.2}$ $M_\odot$ for QGs at $z \sim 0.3$ and $z \sim 0.9$ respectively. Hence, to ensure mass complete data, we first limit our analysis to galaxies with $M_* > 10^{9.5}$ $M_\odot$ for SFGs, $M_* > 10^{10}$ $M_\odot$ for QGs at $z \leq 0.75$ and $M_* > 10^{10.2}$ $M_\odot$ for QGs at $z > 0.75$. Thus, we have assumed that the completeness limit in masses estimated by Golob et al. (in prep.) is also true for the sample studied in this thesis. A direct comparison between galaxy stellar masses used by Golob et al. (in prep.) and those used in this study shows a good agreement in mass estimates (lower panel in Figure 3.1). Because of the mass completeness limit of QGs, we also limit the redshift range of this study to $0.1 < z < 0.9$. Moreover, even if the galaxy sample appears complete at $z > 0.9$, we cannot constrain their stellar mass well due to limitations in available wavelength coverage to bracket several spectral features like 4000 $\AA$ break. Additionally, we restrict the sample to 24^{th} magnitude in each band. This magnitude-based constraint is due to limitations in the algorithm we use for morphology analysis while measuring the structural parameters at fainter magnitudes (Chapter 5). This magnitude cut results in the exclusion of more galaxies from our final sample, preferentially at higher redshifts and lower masses (Figure 3.2). For example, when we use *i*-band data with a magnitude cut $i < 24$ at $0.1 < z < 0.9$, we lose 1.7% of the mass complete SFG sample (at $M_* > 10^{9.5}$ M$_\odot$). The loss is 1.1% for QGs with $M_* > 10^{10}$ M$_\odot$ at the same redshift range.

3.1.2 Classification into Star-forming and Quiescent

The morphology of SFGs and QGs evolves differently due to differences in the processes that drive their evolution (van der Wel et al. 2014; Matharu et al. 2019; Mowla et al. 2019b). Therefore, it is important to separate them before performing the analysis. We primarily use UVJ colour-colour diagrams (Wuyts et al. 2007; Williams et al. 2009; Brammer et al. 2011) based on rest-frame $U - V$ and $U - J$ colours to classify galaxies into SFGs and QGs. The QG population generally occupies redder regions in $U - V$, since they are populated

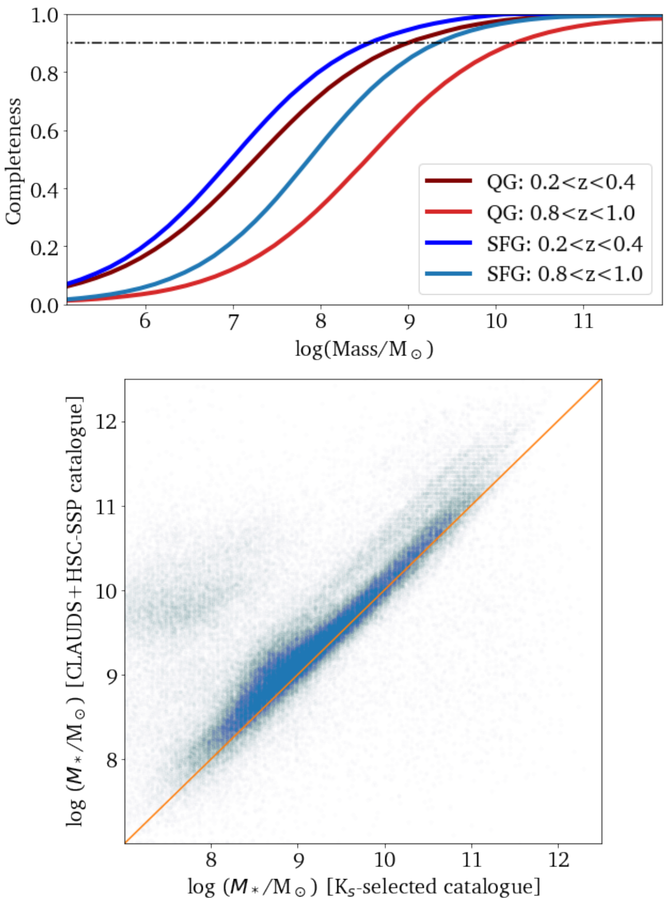

Figure 3.1: Upper: Mass completeness of the CLAUDS+HSC-SSP Survey for QGs and SFGs in two redshift intervals. The horizontal dotted line represents 90% completeness. The image is reproduced from Golob et al. (in prep.). Lower: Comparison between galaxy stellar masses used by Golob et al. (in prep.) and galaxy stellar masses in the K$_s$-selected catalogue used in this study. The orange line indicates the 1:1 relation between galaxy masses.

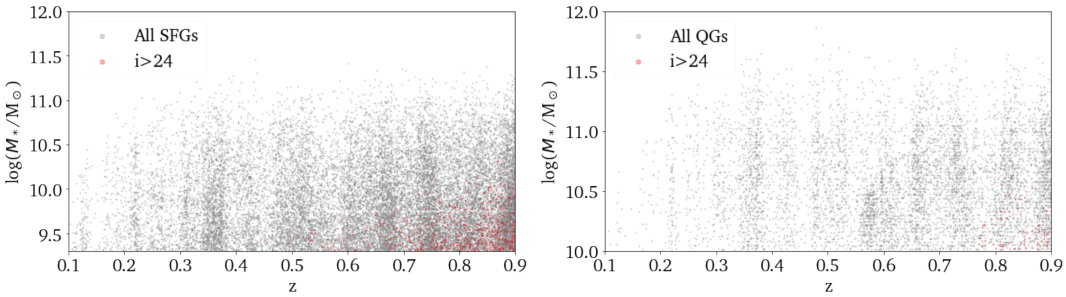

Figure 3.2: Stellar mass of galaxies as a function of redshift. Grey points represent all galaxies while red dots show fainter galaxies ($i > 24$) excluded from the study. SFGs are shown in the left panel and QGs in the right panel.

predominantly by old red stars. However, a young dusty galaxy also appears red and can be misclassified as an old passively evolving galaxy. An advantage of the UVJ diagram is that it helps to distinguish a dusty SFG from a QG because a range in $V-J$ colours exists for a given $U-V$ colour. And also, the $U-V$ colour brackets the 4000 $\AA$ break, a prominent feature in old galaxies. QG colours are bluer beyond the 4000 $\AA$ break (and thus, QGs have bluer $V-J$ colours), but a dusty young galaxy will be redder in both $U-V$ and $V-J$ colours. Therefore, we use UVJ rest-frame colours from Muzzin et al. (2013a) to separate QGs from SFGs in the COSMOS/UltraVISTA region by applying a selection criterion,

$$(U-V) > 0.88 \times (V-J) + 0.69. \tag{3.1.1}$$

This equation assumes a static colour-colour relation at $0 < z < 1$. Although several studies (Muzzin et al. 2013b; Carnall et al. 2018) use this static selection, others rely on various evolving UVJ selections for the quiescent sample (Moresco et al. 2013; Williams

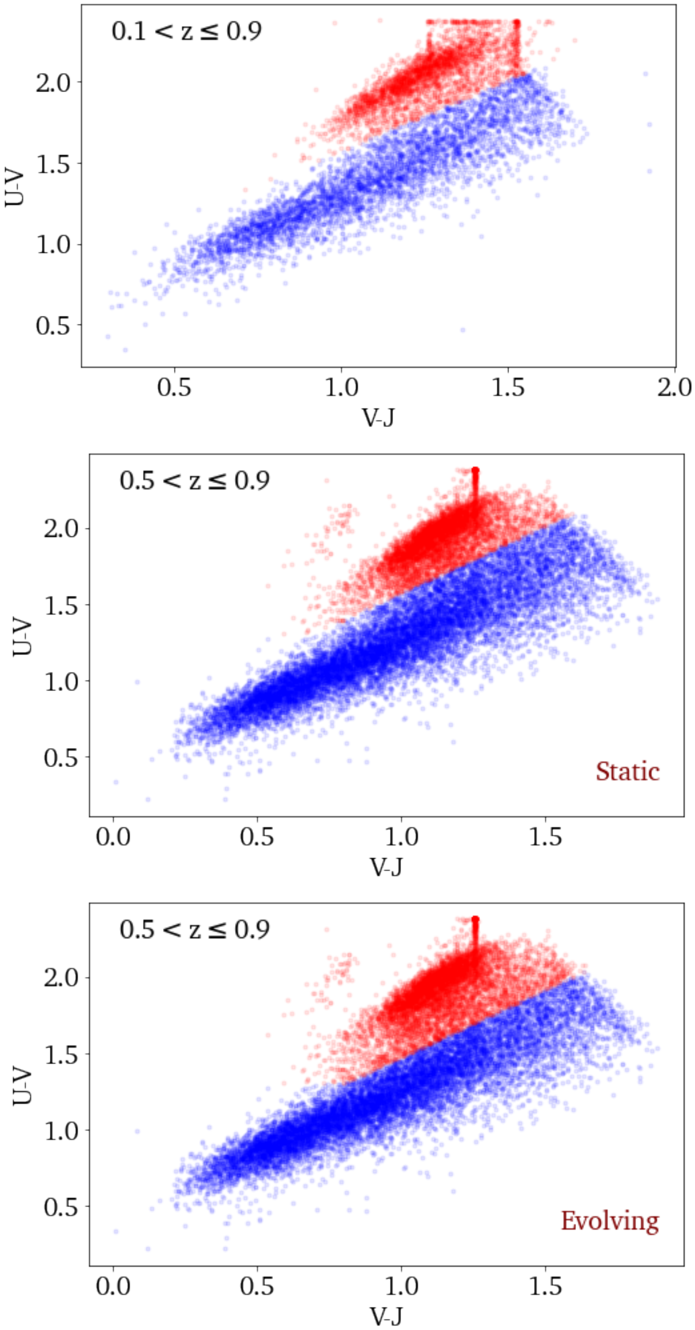

Figure 3.3: Classification of galaxies into SFGs (blue) and QGs (red) in the UVJ diagram. UVJ colours are taken from Muzzin et al. (2013a). The upper panel gives the UVJ selection at $0.1 < z \leq 0.5$. The middle and lower panels show the UVJ selection at $z > 0.5$ using static and evolving selection criteria respectively (Section 3.1.2).

Table 3.1: SFGs and QGs selected using UVJ diagrams in the COSMOS/UltraVISTA region. SFGs in the sample have stellar mass $> 10^{9.5}$ $M_\odot$. QGs have stellar mass $> 10^{10}$ $M_\odot$ at $z \leq 0.75$ and stellar mass $> 10^{10.2}$ $M_\odot$ at $z > 0.75$. Static selection is based on Equation 3.1.1 and evolving selection is based on is based on Equation 3.1.2.

Population	**Static**	**Evolving**
SFG	16936	16013
QG	6829	7434
All	23765	23447

et al. 2009; van der Wel et al. 2014). Hence, we also apply evolving selection criteria from Williams et al. (2009) to isolate QGs from SFGs in the UVJ diagram, which is given by

$$\begin{aligned}(U-V) &> 0.88\times(V-J)+0.69 \qquad [0.0<z<0.5],\\ (U-V) &> 0.88\times(V-J)+0.59 \qquad [0.5<z<1.0].\end{aligned} \tag{3.1.2}$$

We also introduce an additional restriction in the $U-V$ colour in both static and evolving criteria: $U-V > 1.3$. We utilise the K_s-selected catalogue to obtain rest-frame $U-V$ and $V-J$ colours. Figure 3.3 shows the UVJ diagrams for our sample overlapping with the COSMOS/UltraVISTA field and Table 3.1 provides the number of galaxies selected from UVJ diagrams in CLAUDS+HSC-SSP i-band. The plots suggest that the evolving UVJ selection criteria by Williams et al. (2009) misclassify some of the galaxies ($\sim 10\%$) from the blue cloud (star-forming galaxies in the UVJ diagram) as QGs at $z > 0.5$. Hence, we use the static UVJ selection (Equation 3.1.1) to separate QGs from SFGs in this thesis.

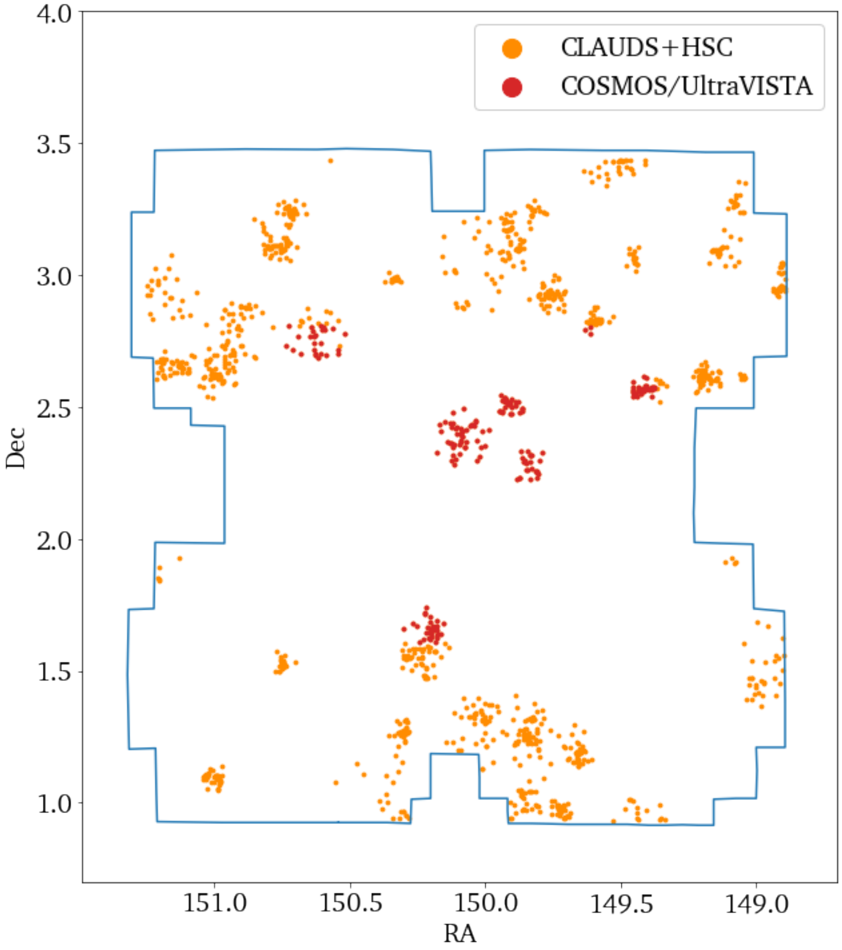

Figure 3.4: Galaxy cluster members identified from the HSC Cluster Catalogue (Oguri et al. 2018). Red dots represent cluster members from the overlapping region with the COSMOS/UltraVISTA field which are analysed in this study. Orange dots denote other cluster members from the the CLAUDS+HSC-SSP field. The boundary of the CLAUDS+HSC-SSP is shown in blue.

3.1.3 Clusters

Clusters represent dense environments in the Universe. Studying the morphology of galaxies in clusters will help us understand the role environment plays in the evolution of galaxies (Section 6.3). We identify clusters in our sample using the HSC-based optically-selected cluster catalogue by Oguri et al. (2018). This cluster catalogue utilises the CAMIRA algorithm (Oguri 2014) to locate clusters in HSC data. The CAMIRA uses the stellar population synthesis (SPS) models by Bruzual & Charlot (2003), calibrated using galaxies with spectroscopic redshifts, to predict colours and stellar masses of the red sequence galaxies. The red sequence is a tight relation in the colour-magnitude diagram of cluster galaxies (Bower et al. 1992b,a) and it is a well-used method in the literature to identify clusters in surveys (Gladders & Yee 2000; Martinet et al. 2017). The red sequence has a slightly negative slope (tilt) as the galaxy colours bracketing the $4000\AA$ break change with magnitude. The tilt is a result of mass dependence of metallicity (Kauffmann & Charlot 1998; Kodama & Arimoto 1997; Stanford et al. 1998). For each galaxy in the observed sample, the CAMIRA algorithm computes the likelihood of it being a red-sequence galaxy at a give redshift by comparing its observed colour and magnitude with the colours and magnitudes of model galaxies that form red sequence at that redshift. Every galaxy is then assigned a non-integer number parameter as a function of redshift originating from these likelihoods. The sum of these number parameters at a given redshift and position on the sky provides the richness parameter. Then, Oguri et al. (2018) identify clusters from the peaks of three-dimensional

Table 3.2: Details of HST CLASH cluster members studied.

Cluster	**Cluster Members**			**Red Sequence Tilt**
	FoF	**Red Sequence**	**Total**	
A383	35	4	39	-0.018 ±0.008
A611	44	20	64	-0.010 ±0.010
A1423	10	39	49	-0.018 ±0.008
A2261	14	35	49	-0.010 ±0.007
RXJ2129	36	26	62	-0.011 ±0.008
Total	139	124	263	

richness maps. While selecting clusters from the cluster catalogue, we introduce a cut in the richness parameter to be greater than 15 to select only rich galaxy clusters. Figure 3.4 shows the clusters selected from the HSC cluster catalogue. There are $\sim$ 80 member galaxies residing in 7 clusters identified at $0.1 < z < 0.9$ in the COSMOS/UltraVISTA region.

3.2 HST CLASH Survey

Members of the five HST CLASH clusters are primarily identified with the help of the FoF algorithm (Sohn et al. 2018) using spectroscopic data as described in Section 2.2.2. The number of FoF identified galaxies totals 139 excluding BCGs. Since the sample size is small, we use the red sequence method (Section 3.1.3) to identify additional quiescent member galaxies in these clusters. We plot the f606w-f814w colour as a function f814w magnitude (Figure 3.5). To avoid fainter galaxies, we limit our analysis to galaxies brighter than 22$^{\text{nd}}$ magnitude in f814w and we show galaxies selected to estimate the red sequence as green stars in the Figure. Once we estimate the cluster red sequence by performing a

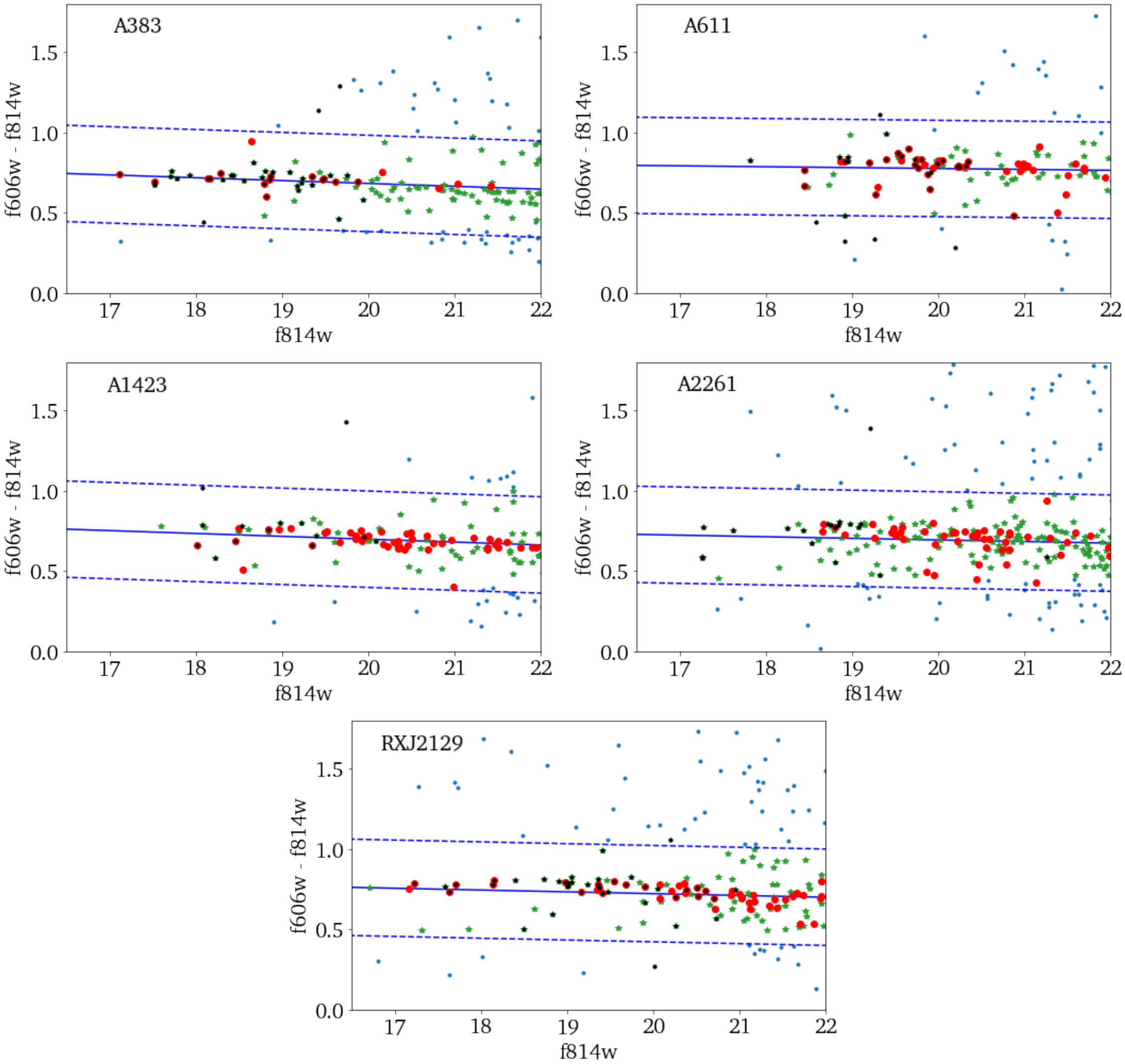

Figure 3.5: Red Sequence selection of CLASH cluster members. Green stars represent galaxies selected for the red sequence fitting. The blue line is the red sequence obtained and blue dashed lines denote ±0.3 mag width of the red sequence. Red dots are galaxies identified as cluster members from the red sequence. Black dots are spectroscopically confirmed members while blue dots show the distribution of other galaxies from the catalogue in the colour-magnitude diagram.

linear fit (blue solid line) to these selected galaxies, we set the width of ±0.3 mag in colour, a widely used red sequence width in the literature (De Lucia et al. 2007; Martinet et al. 2017) to identify cluster members. We add a further cut in terms of photometric redshifts. We only use galaxies whose 95% confidence interval of BPZ redshift covers the cluster redshift. These galaxies selected using red sequence method are shown as red data points in the Figure 3.5. Thus, we have, in total, 263 CLASH cluster galaxies selected using both the FoF and the red sequence method, and the details are given in Table 3.2. Figure 3.6 shows these selected member galaxies in HST CLASH f814w images. We utilise the CLASH cluster members to study how the evolution of galaxies in cluster cores differs from the field (Section 6.3.2).

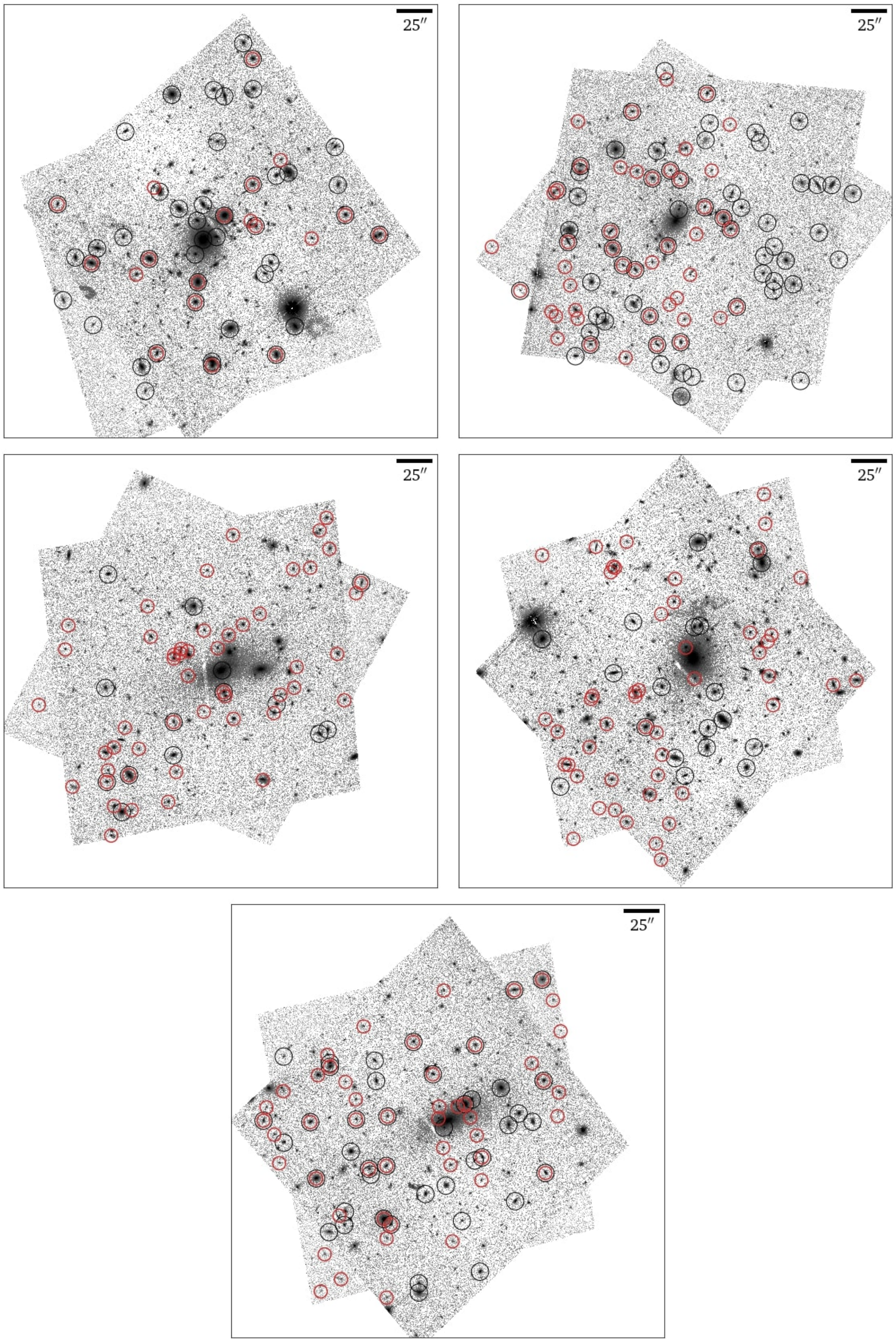

Figure 3.6: f814w images of the five CLASH clusters. Black circles denote spectroscopically identified cluster members and red circles are those selected from the red sequence.

Chapter 4

Methodology

It is important to quantify the morphology of a galaxy to understand galaxy structure and galaxy evolution. We apply the conventional approach by measuring the morphological features of galaxies parametrically. Parametric studies measure the morphology by modelling the light distribution of galaxies as projected into the plane of the sky with a prescribed analytic function (Peng et al. 2010a). On the other hand, non-parametric measurements do not require a model to extract morphological information of galaxies (e.g., Petrosian 1976; Lotz et al. 2004). As non-parametric methods do not include analytic functions that can be extrapolated down to and beyond fainter outer regions, they depend more heavily on the depth of the survey than parametric methods do. Additionally, our parametric approach allows us to compare our results with the literature because many studies that focus on galaxy evolution measure galaxy morphology parametrically (e.g., Williams et al. 2010; van der

Wel et al. 2014; Mowla et al. 2019b).

We can perform this analytic modelling through either one dimensional (1D) or two dimensional (2D) profile fitting. One of the disadvantages of 1D against 2D is that non-axisymmetric components (eg. bars) cannot be described as they are averaged out (de Jong 1996). We may lose information when we use averaged 1D distributions of the 2D projections of 3D objects (galaxies). In addition, convolution of models with the PSF is much less reliable in the 1D than in the 2D (Ciambur 2016). A 2D profile fitting process considers instead the whole projected light distribution of a galaxy on the sky. Therefore, we take a 2D approach in the current study.

A single analytic function may not suffice to describe the morphology of a galaxy completely. A multi-component profile fitting is necessary to extract the disk and bulge components of galaxies as well as to describe their complex structures such as bars and spiral arms. However, a single component profile fitting would suffice in our study because the objective of the study is to analyse global features of galaxies (e.g., size). This chapter describes in detail the process we follow to extract information (size, shape and concentration) on galaxy structural properties.

4.1 GALFIT

There are several galaxy light profile fitting softwares, e.g, GIM2D (Simard 1998), GALFIT[1] (Peng et al. 2002, 2010a), GASPHOT (Pignatelli et al. 2006), BUDDA (de Souza et al. 2012) and ProFit (Robotham et al. 2017). Although GIM2D and GALFIT, widely used softwares in the literature, are similar fitting processes, their performance differs. One of the main advantages of GALFIT over GIM2D is that GALFIT can fit more than one galaxy simultaneously whereas the latter can do it only one at a time. When using GIM2D, one needs to mask out all neighbouring objects in the image, which may also affect the light profile of the galaxy being studied. This results in a poor fitting for strongly blended galaxies (Häussler et al. 2007). Consequently, we deploy GALFIT in this research.

GALFIT is a two-dimensional parametric light profile fitting software tool. This image analysis algorithm is a stand-alone program written in the C language. It can model the brightness profiles of galaxies, stars and other celestial light sources in digital images. GALFIT can perform complex image decomposition tasks. It can simultaneously fit radial profiles of more than one galaxy along with their substructures using a combination of various parametric functions: Sérsic profile (Sersic 1968, see Section 4.2), Nuker Law (Lauer et al. 1995), empirical King profile (Elson 1999), Moffat profile (Moffat 1969), modified Ferrer profile (Binney & Tremaine 1987), exponential disk profile, Gaussian profile and edge-on disk profile (van der Kruit & Searle 1981).

---

[1] `http://ascl.net/1104.010`

Peng et al. (2002, 2010a) explain how to use GALFIT to model galaxy light profiles. In short, GALFIT models the light profile of a galaxy with one or more analytic functions and then convolves the model with the PSF along with a CCD diffusion kernel to reproduce image smearing by Earth's atmosphere, telescope optics and detector properties. GALFIT also allows the users to mask bad pixels in the image. GALFIT uses the Levenberg–Marquardt technique (Moré 1978) to find the optimum fit. This technique helps to fit the complex images with multiple components and a large number of parameters. Finally, GALFIT uses χ^2 statistics to determine the goodness of fit and displays it in terms of reduced χ^2. The goodness of fit is indicated by reduced χ^2 and is defined as

$$\chi^2 = \frac{1}{N_{\mathrm{DOF}}} \sum_{x=1}^{nx} \sum_{y=1}^{ny} \frac{(f_{\mathrm{data}}(x,y) - f_{\mathrm{model}}(x,y))^2}{\sigma(x,y)^2} \tag{4.1.1}$$

where f_{data} is input data, f_{model} is model image, N_{DOF} is the degree of freedom (number of pixels - number of free parameters), nx and ny denote the number of pixels, and *sigma* is the standard deviation of counts at each pixel (uncertainty or noise).

One of the disadvantages of GALFIT is that it is not designed or optimized for automation. Therefore, we need some external automation tools like GALAPAGOS (Barden et al. 2012). In this study, we automate the galaxy fitting process in PYTHON using GalfitPyWrap[2], a PYTHON wrapper for GALFIT, with some custom modifications. The detailed fitting process is described in Section 4.3.

---

[2] `https://github.com/Grillard/GalfitPyWrap`

4.2 Sérsic Profile

The Sérsic power law (Sersic 1968) is a well studied and extensively used radial brightness profile to quantify galaxy morphology (e.g., Trujillo et al. 2001, 2004; van der Wel et al. 2014; Zanella et al. 2016). Proposed by José Luis Sérsic, it is defined as

$$\log\left(\frac{\Sigma(R)}{\Sigma_e}\right) = -b_n\left[\left(\frac{R}{R_e}\right)^{1/n} - 1\right], \tag{4.2.1}$$

where R_e is the effective radius, Σ_e is the surface brightness at R_e and n is the Sérsic index, which defines the concentration of the profile. The coefficient b_n is not a free parameter and is defined in terms of n such that a region within R_e encloses half of the total luminosity of the galaxy. We can approximate the value of the coefficient to be $b_n \approx 1.999n - 0.3271$, if $0.5 < n < 10$ (Graham et al. 2003). Gaussian profile, exponential disk profile and de Vaucouleurs profile (de Vaucouleurs 1953) are special cases of the Sérsic profile with $n =$ 0.5, 1 and 4 respectively. Figure 4.1 shows the Sérsic power law for different values of n. For galaxies with larger n, light is concentrated in the central region, but also the surface brightness is still significant at larger radii (extended wings). Consequently, galaxies with higher n are sensitive to the estimation of background sky levels. On the other hand, profiles with smaller n are flatter in the inner regions and have truncated wings. Sersic profiles are also convenient for classifying galaxies morphologically. A galaxy with $n \sim 4$ is an elliptical (early type) galaxy while $n \sim 1$ denotes a disky (late type) galaxy.

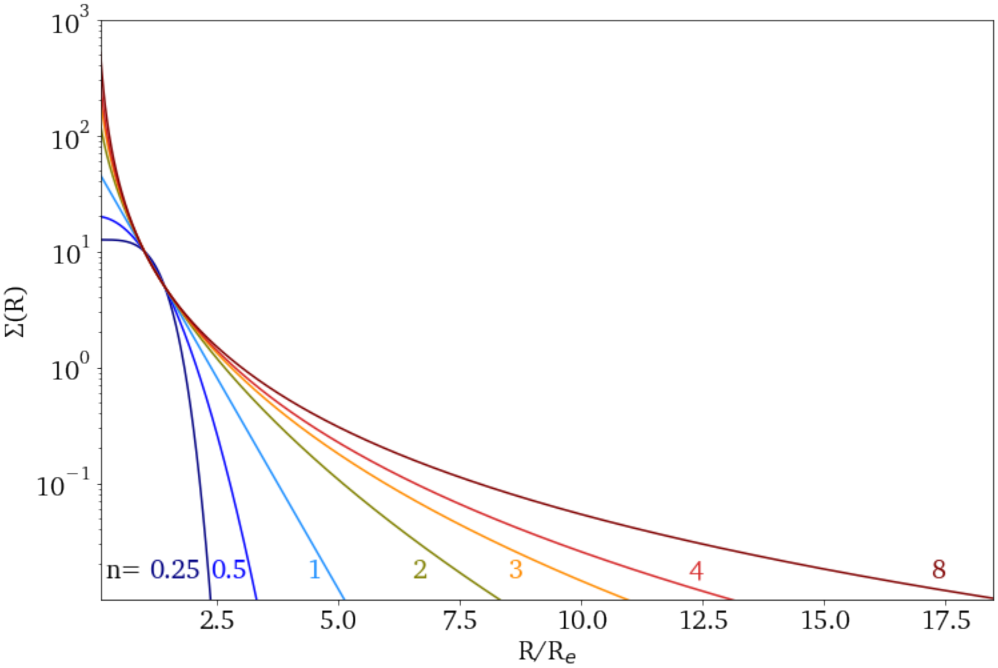

Figure 4.1: Sérsic radial profile for different values of n. Both Σ_e (=10) and R_e (=5) are kept fixed while calculating the surface brightness values at different radii. $n = 0.5$ indicates a Gaussian profile, $n \sim 1$ denotes the light profile of a disky galaxy and $n \sim 4$ denotes a bulgy galaxy.

The total flux of a galaxy is estimated by integrating out the surface brightness to $r = \infty$ and is given by

$$F_{tot} = 2\pi R_e^2 \Sigma_e n \frac{e^{bn}}{(b_n)^{2n}} \Gamma(2n) \frac{q}{R(C_0;m)}, \tag{4.2.2}$$

where the Gamma function

$$\Gamma(2n) = (2n-1)!,$$

q is the axis ratio and $R(C_0;m)$ is a geometric correction factor that takes into account the deviation in the azimuthal shape of the galaxy light profile from a perfect ellipse. $R(C_0;m)$ is defined as the ratio between the area of a perfect ellipse and the area of the ellipsoid of galaxy light profile with the same q when the radius is unity, where C_0 is free parameter that controls diskyness/boxiness of the galaxy light profile and m is the Fourier mode. GALFIT performs a Fourier transformation to describe this deviation from perfect ellipticity in profiles. However, we do not incorporate such deviations described by Fourier transformation in our fitting process and therefore, GALFIT considers $R(C_0;m)$ to be 1. GALFIT generally uses the integrated magnitude as the flux parameter for Sérsic profiles, although one can use surface brightness magnitudes at the centre (x_0, y_0) and at R_e (Peng et al. 2010a). This integrated magnitude is given by

$$m_{tot} = -2.5 \log\left(\frac{F_{tot}}{t_{exp}}\right) + m_{ZP}, \tag{4.2.3}$$

where t_{exp} is the exposure time and m_{ZP} is the zero point magnitude[3]. Generally, a Sérsic profile fitting in GALFIT can have seven classical free parameters: x_0, y_0, m_{tot}, R_e, n, q and θ_{PA}. x_0 and y_0 denote the centroid of the light profile and θ_{PA} is the position angle of the profile. The position angle is defined in such a way that if the semi-major axis is aligned parallel to the y-axis, $\theta_{PA} = 0^\circ$ and, θ_{PA} increases towards counter-clockwise direction.

4.3 Fitting Process

In this study, we fit the galaxy light profiles with a single Sérsic profile using GALFIT. Although the details of the fitting process vary between CLAUDS+HSC-SSP data and HST CLASH data, the fundamental structure remains the same. The fitting pipeline is illustrated in Figure 4.2 and is explained in the following sections (Sections 4.3.1 and 4.3.2).

4.3.1 Cutouts and Masking

We identify galaxies in CLAUDS+HSC-SSP at $0.1 < z < 0.9$ with the help of the CLAUDS+ HSC-SSP catalogue by Moutard et al. (2020). Our simulations show that our fitting procedure does not estimate the structural parameters of galaxies fainter than 24th magnitude accurately (Chapter 5). Therefore, we apply a magnitude cut of 24 in a given band.

We then make postage stamp cutouts of data with size $33.6'' \times 33.6''$ centred at each

---

[3] A photometric zero point magnitude refers to the magnitude of an object which produces one count per second in the detector.

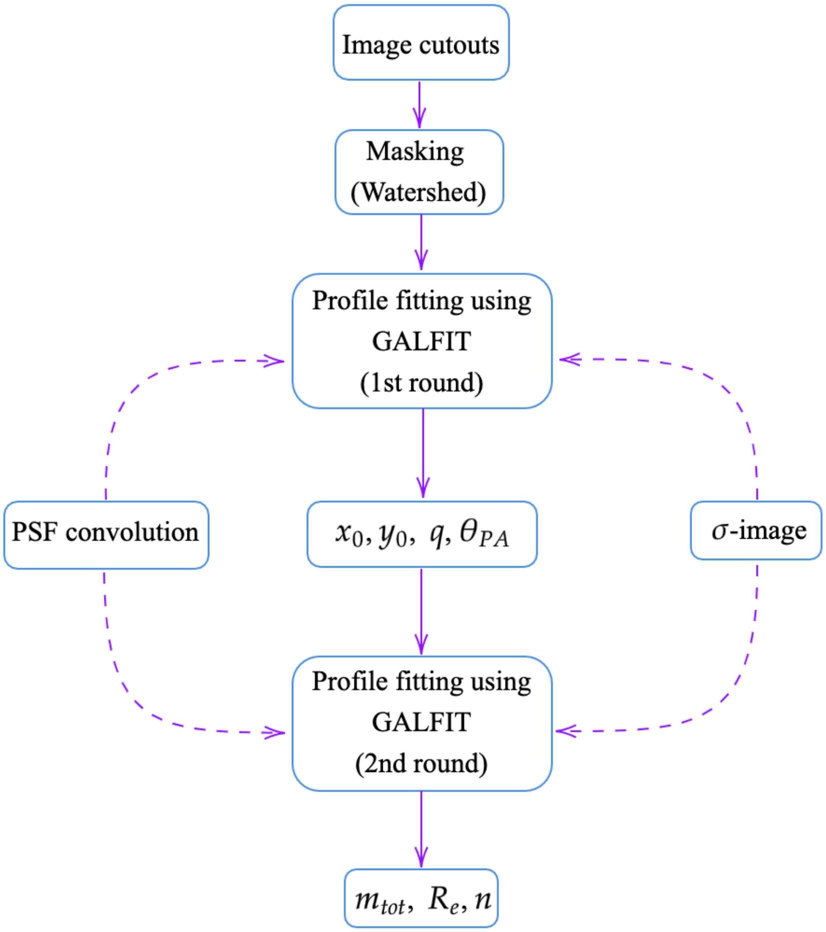

Figure 4.2: Sérsic profile extraction pipeline.

target galaxy. The size of the cutout which is used for fitting is defined by two competing requirements. Firstly, the size of the cutout minimise computational cost in the fitting process. Secondly, the size of the image cutout also ensures that the cutout includes the profiles of the target galaxy and its neighbouring galaxies in the sky.

When we fit the profile of a galaxy, we simultaneously fit its neighbouring galaxies in the image as well. This is to avoid unnecessary bad pixel masking and subsequent loss of data. This simultaneous fitting also allows to subtract the contribution of the wings of the neighouring galaxies' light profile from the light profile of the target galaxy. To perform the simultaneous fitting efficiently, we select a sub-region within the cutout with dimensions $\sim 10.1'' \times 10.1''$. Within this sub-region, we fit all galaxies whose brightness is within 5 magnitudes of the brightness of the target galaxy. Light profiles of any fainter galaxy cannot affect the surface brightness profile fitting of the target.

We perform a similar procedure on HST CLASH data as well. We make image cutouts with size $24'' \times 24''$. We consider all galaxies within a distance of $7''$ from a given galaxy to fit simultaneously with the target galaxy. We then select galaxies that are brighter than 23.5 magnitudes in f814w and not more than 5 magnitudes fainter than the target galaxy.

We mask out all other fainter galaxies and other objects including stars in both CLAUDS +HSC-SSP and CLASH data. We use the Watershed segmentation technique with the aid of the PHOTOUTILS package for PYTHON for this marking purpose. The watershed algorithm treats pixel values in the image as an inverted local topography where the centroids of bright objects will be at local minima of this topography. The algorithm works in analogy to water flooding a basin. It floods the image starting from minima and sets the boundaries for objects where water spills over. Consequently, the algorithm generates a segmentation map for the light sources in the image cutout. The algorithm then deblends all overlapping regions and separates the objects in these regions. Finally, it creates an ASCII file containing pixel coordinates belonging to the 'watershed' of all objects to be masked out.

We perform described masking procedure with every galaxy cutout in our two samples. Some examples for masking are shown in the second panels of each row in Figures 4.3 and 4.4. Our masking schemes are at times severe; they mask some of the structural features of extended galaxies. This drawback is prominent in HST images (see masked images of galaxies A383_6237 and A1423_2741 in Figure 4.4). Nonetheless, such aggressive masks cover only special features in the galaxy outskirts such as star-forming regions in its spiral arms which constitute a small portion of the total light profile of a galaxy. Therefore, it should not affect our effort to describe the overall light profiles of galaxies.

4.3.2 Sérsic Profile Fitting

Once cutouts creation and masking are performed, we run GALFIT to fit the light profile of unmasked galaxies in the cutout using a single Sérsic profile for each galaxy. We do this in two steps similar to a procedure followed by Matharu et al. (2019). In the first run, we keep all seven classical GALFIT parameters free to obtain refined values of galaxy shape

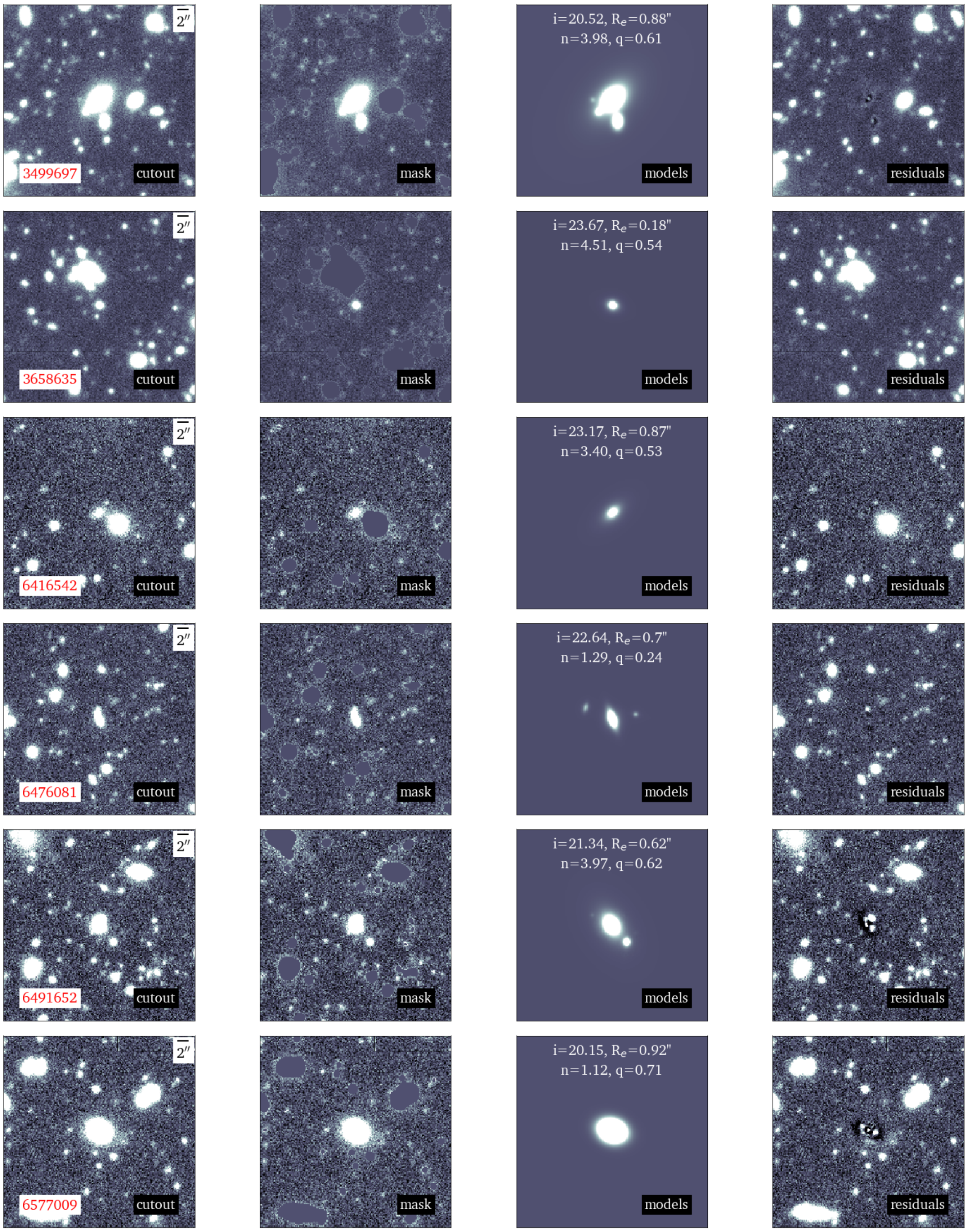

Figure 4.3: Panels in each row show the input cutout image (*i*-band), masked image, best-fit models and residual image of some of the CLAUDS+HSC-SSP galaxies. Numbers in red are galaxy IDs from the CLAUDS+HSC-SSP catalogue by Moutard et al. (2020). The Sérsic parameters of the target galaxies are shown in the third panel of each row.

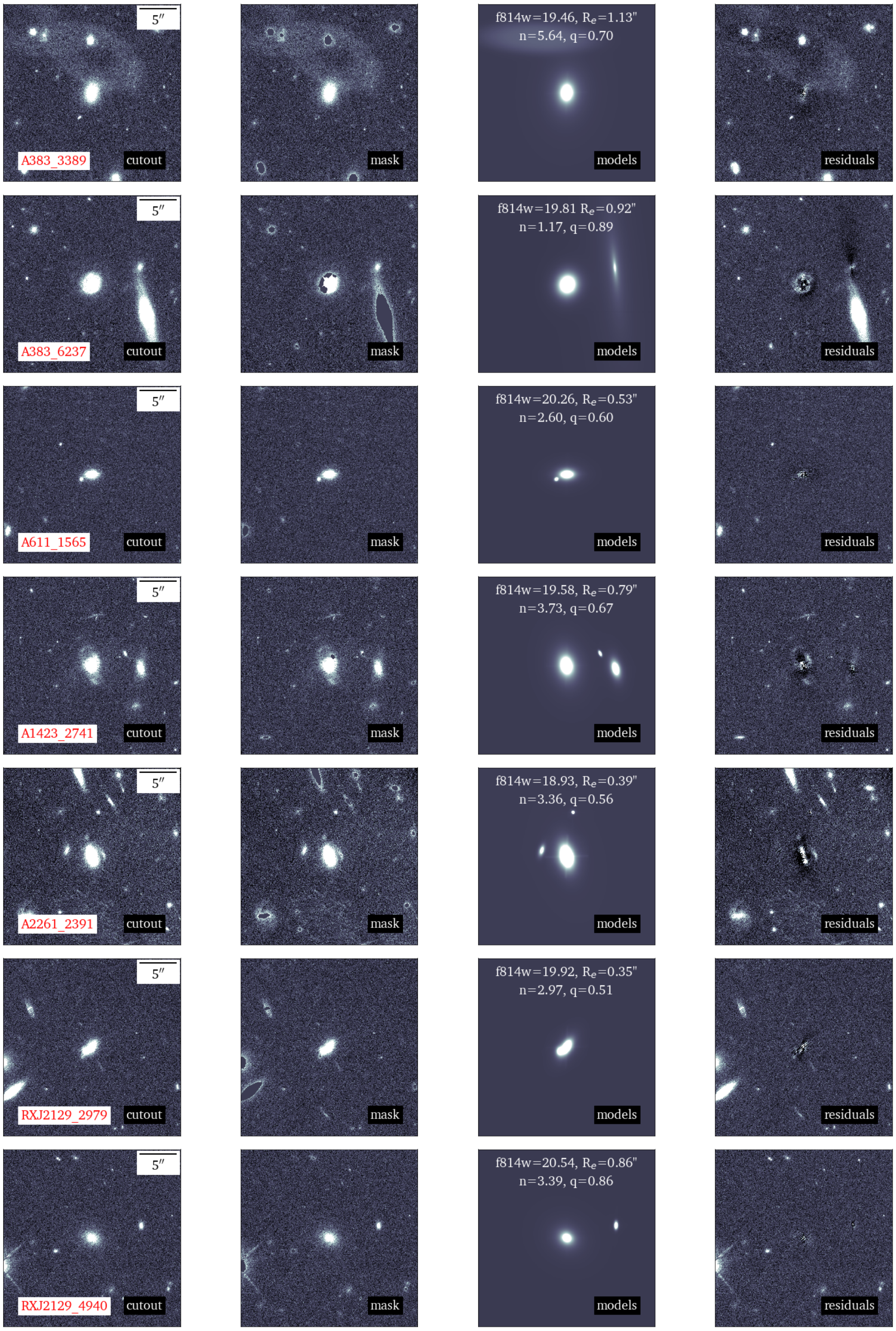

Figure 4.4: Images of some HST CLASH galaxies. Panels are shown in the same way as Figure 4.3.

parameters: x_0, y_0, q and θ_{PA}. We provide the best-fit parameters obtained from the first run as inputs to the second run. In this final run, we fix these refined shape parameters and keep the remaining three structural parameters (m_{tot}, R_e and n) free. Although computationally expensive, this two-step approach helps to reduce failures in the fitting process. We obtain the structural parameters of the target galaxy from the results of the second GALFIT run while discarding the information of all other neighbouring galaxies. We repeat this procedure for all galaxies selected (Chapter 3).

In each run, we provide several input files to GALFIT: image cutout, `inputfile`, mask, PSF image, σ-image. The GALFIT `inputfile` specifies galaxies to be fitted and lists all other input files and details. The mask file (from the Watershed procedure) provides the pixel coordinates of all objects and artefacts in the image to be masked out. GALFIT avoids these pixels while obtaining the best-fitting Sérsic parameters for galaxies. Selections of PSF images for CLAUDS+HSC-SSP and HST CLASH galaxies are described in Sections 2.1.1 and 2.2.1 respectively. Since the HST PSF obtained from TinyTim is three times oversampled, it is not convolved with the CCD diffusion kernel. Hence, we provide the CCD diffusion kernel obtained from TinyTim as an input to GALFIT along with the HST PSF image. GALFIT convolves the PSF with the diffusion kernel after rebinning the PSF data. We provide the σ-image for HSC data, which describes the Poisson uncertainty of data at the pixel level. We do not provide a σ-image for HST data but let GALFIT generate one. This is possible only because we have pixel level information regarding its exposure time and using this information on the exposure time, we can convert the pixels units from counts/s to counts. In the absence of a σ-image, GALFIT automatically generates one for HST data internally based on the gain and read-noise parameters taken from the image header provided that the units of pixel values are in counts.

Additionally, we provide a constraint file that defines the parameter space where GALFIT can search for best-fit values in CLAUDS+HSC-SSP data. This constraint file restricts the parameter space to

$10 \leq m_{tot} \leq 30$,

$0.1 \leq R_e \leq 50$ pixels,

$0.1 \leq n < 20$,

$0.02 \leq q \leq 1$.

We also limit the pixel coordinates of the centroid of the galaxies within ±4 pixels from the SExtractor estimated centroid given in the CLAUDS+HSC-SSP catalogue by Moutard et al. (2020). Finally, we restrict the magnitude space to be within ±2 from the SExtractor values in the CLAUDS+HSC-SSP catalogue. This constraint file ensures that GALFIT does not wander far from the best fitting model and return unphysical parameters through failed fits. However, we do not provide a constraint file while fitting HST galaxies because we do not observe GALFIT wandering off in this case. The reason for this may be the better resolution of the HST data. Alternatively, the better performance of GALFIT here may be because the software creates its own σ-image.

Furthermore, we introduce an additional step when dealing with CLASH cluster cores. Since these systems are relaxed and the image shows the core, the image is dominated by the light from the BCG. Hence, it would be difficult to study the structure of galaxies close to the centre of the clusters. So, we first fit the BCG with a single Sérsic profile and subtract the BCG profile from the data before we run GALFIT on other target galaxies. Figure 4.5 demonstrates Sérsic models of BCGs obtained from the images. Residual images show how the cluster images look after removing BCG models from the data. Although a BCG cannot be fully modelled by a single Sérsic profile because of its complex structure, the residual images show that a single Sérsic profile fitting of BCGs is sufficient to remove majority of its light from the image and thereby, to study the light profiles of its neighbouring galaxies.

We have visually examined a subset of the GALFIT generated output images. Figure 4.3 shows the images of the Sérsic models of some of the galaxies in HSC *i*-band data obtained from our pipeline. In some cases, our fitting results show a significant amount of residuals because of the complex structures present in galaxy light profiles. A single Sérsic profile is not sufficient to describe the details of galaxy morphology. For example, modelling a galaxy with comparable disk and bulge components with a single Sérsic profile will give a residual image with an an under-subtracted core and over-subtracted outer region surrounding the core. This may be the case for the galaxy with ID: 3499697 (top row in Figure 4.4). The presence of residuals is even more prominent in HST images (Figure

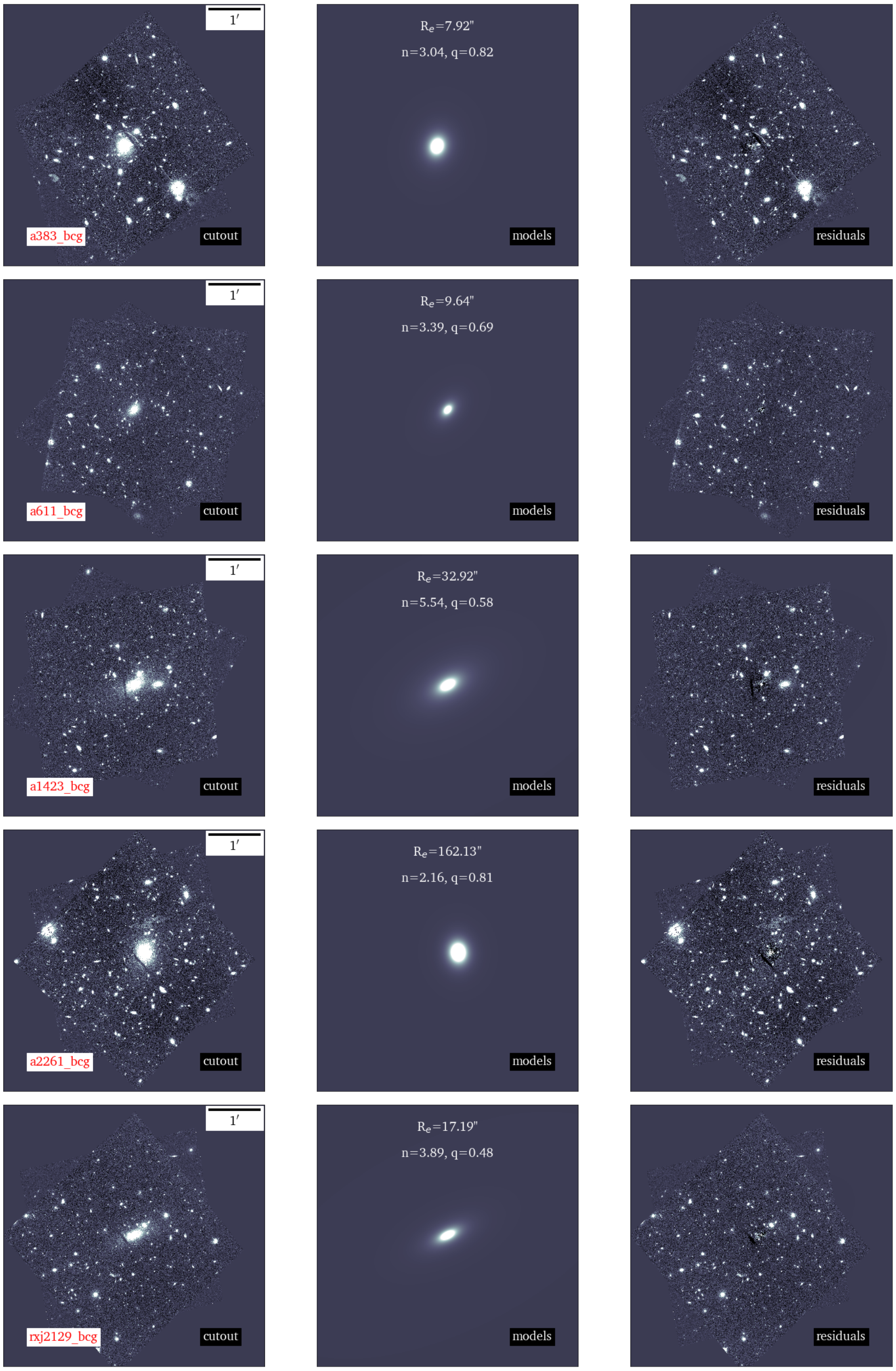

Figure 4.5: Modelling BCGs in HST CLASH clusters. Panels in each row show the input cutout image, best-fit model and residual image. Sérsic parameters of the BCGs are given along with model images.

4.4). One of the reasons for this is better resolution of HST. Nonetheless, our modelling procedures yield satisfactory results to study global morphological features of galaxies such as their sizes and shapes.

4.4 Measurements

We have extracted Sérsic parameters for bright galaxies (brighter than 24th magnitude in a given band) covering $0.1 < z < 0.9$ redshift range in the CLAUDS+HSC-SSP COSMOS field using g, r, i and z bands. However, we identify galaxies with any of the parameters at the extremes of the allowed parameter space as outliers and remove them from the analysis. We do this refinement to ensure that the structural models describe the galaxy light profiles as closely as possible. Hence, we only consider galaxies with estimated Sérsic parameters that meet the following criteria:

$|m_{tot}(\text{out}) - m_{tot}(\text{in})| < 2,$

$0.2 < R_e < 30$ pixels,

$0.2 < n < 15,$

$0.1 < q < 1,$

where $m_{tot}(\text{in})$ is the SExtractor derived magnitude from the CLAUDS+HSC-SSP catalogue by Moutard et al. (2020) and $m_{tot}(\text{out})$ is the magnitude of the best-fitting model. We

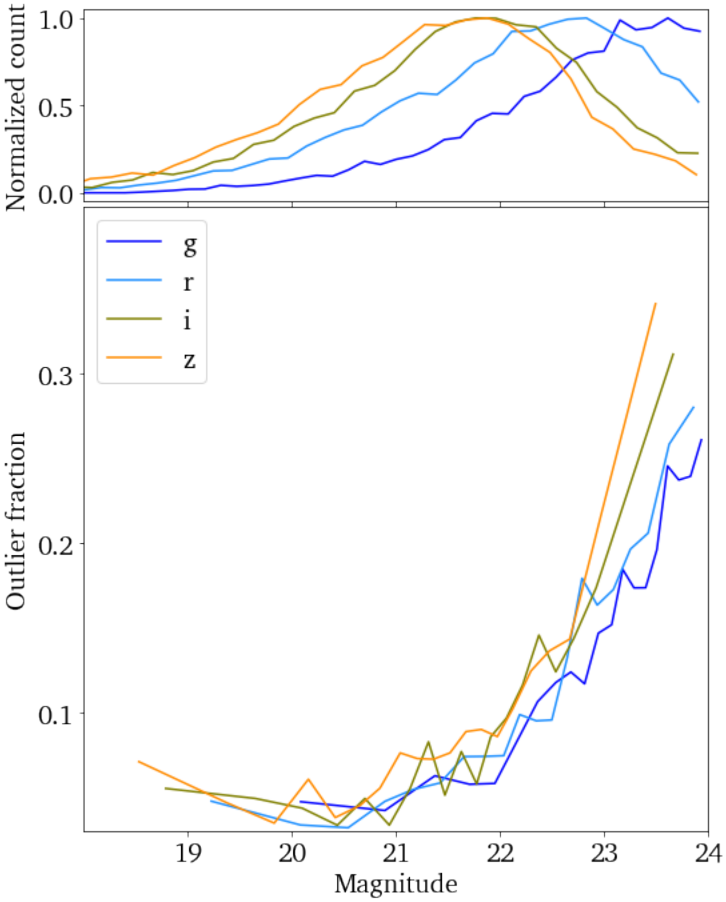

Figure 4.6: Fraction of galaxy profiles considered as outliers according to the definition in Section 4.4. The upper panel shows the distribution of magnitudes of the whole sample at $0.1 < z < 0.9$ with $M_* > 10^{9.5}$ $M_\odot$ in each band.

consider all others as outliers/bad fits. These outlier fractions are $\sim$ 14.1%, 11.9%, 10.1% and 9.9% in g, r, i and z bands respectively (Figure 4.6). Figures 4.7 and 4.8 illustrate how this outlier removal affects the overall parameter distributions. Red data points in the figures represent the outliers while the blue data represent the rest.

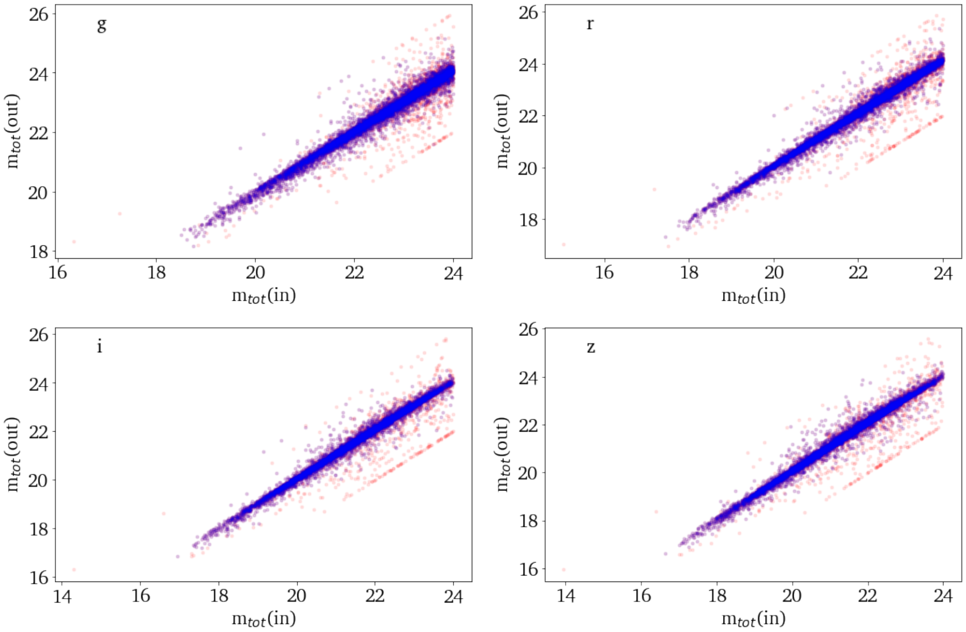

Figure 4.7: Comparison between input and output magnitudes of galaxies fitted in different CLAUDS+HSC-SSP bands. Blue points represent good fits while red represent discarded GALFIT derived galaxy models. See Section 4.4 for details.

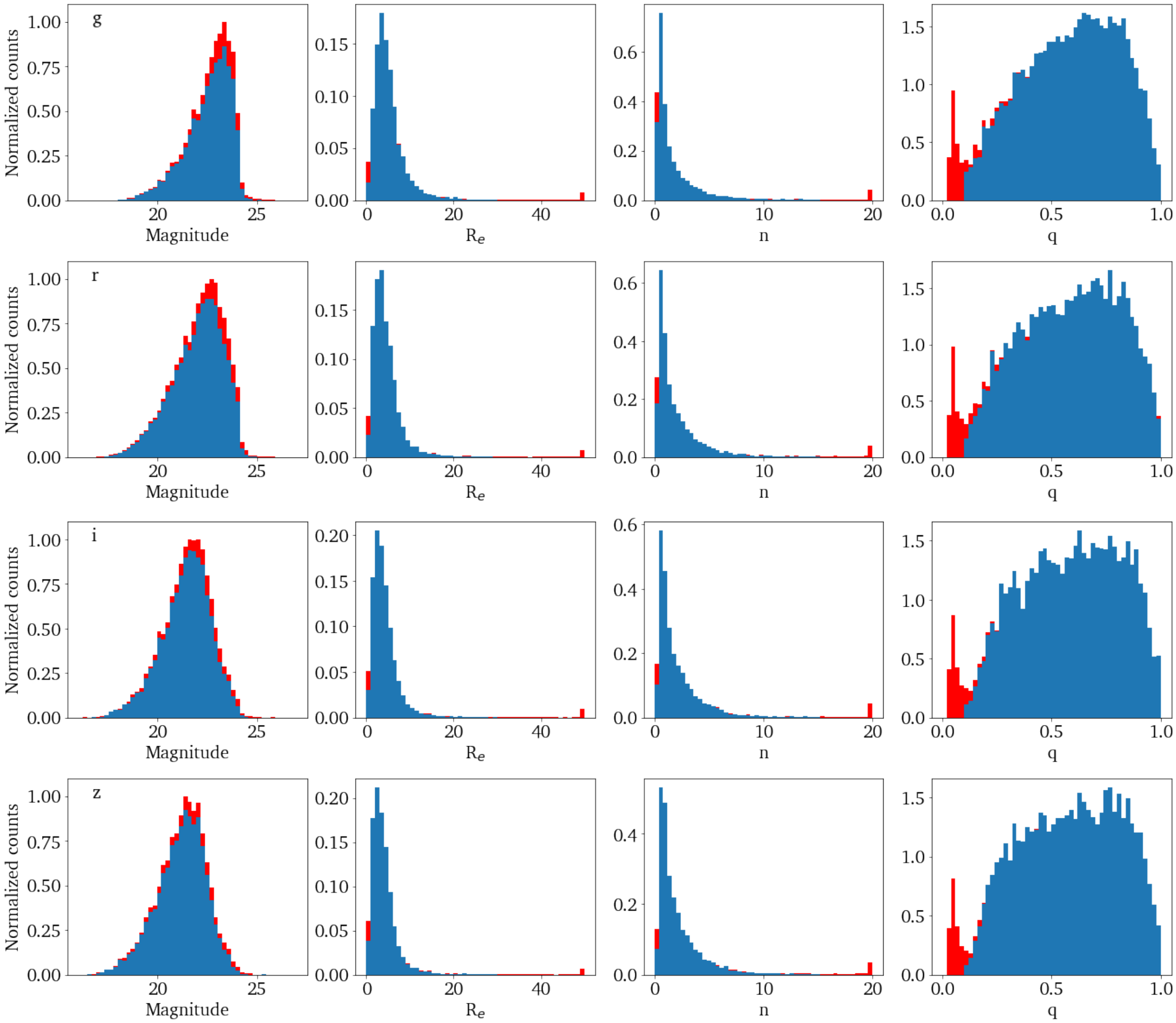

Figure 4.8: Distribution of best-fitting Sérsic model parameters obtained from GALFIT. Discarded outliers (red) are stacked on top of good fits (blue).

4.4.1 Wavelength Correction

Several studies find that the colour gradients and the evolution in these gradients affect galaxy size measurements (Szomoru et al. 2011; Wuyts et al. 2012; Kelvin et al. 2012; van der Wel et al. 2014). Galaxies tend to have larger sizes in bluer bands compared to redder bands due to this colour gradient present in the radial light profiles of galaxies. Therefore, it is important to estimate the sizes of all galaxies at the same rest-frame wavelength. Following other studies in the literature (e.g., van der Wel et al. 2014; Mowla et al. 2019b), we correct our sizes to 5000 $\AA$ in rest-frame. Although van der Wel et al. (2014) provide wavelength corrections for SFGs and QGs, we find that the wavelength dependence of size measurements in their data does not represent the dependence present in our measurements. Therefore, we introduce a different wavelength correction based on the colour gradient we find in our data.

Figures 4.9 and 4.10 demonstrate how we estimate the wavelength correction to convert the size measurements to sizes at rest-frame 5000 $\AA$ for SFGs and QGs respectively. We use size measurements in the g and z bands to find the wavelength dependence of R_e. We avoid the y-band because its depth is shallower than other HSC bands. Similar to previous studies (e.g., van der Wel et al. 2014), we also find that colour gradients increase with the stellar masses of galaxies (Panel A in Figure 4.9). For SFGs, colour gradients also depend on their redshift. We fit linear regression lines to describe the relation between the colour gradients in size measurements and the stellar mass in three redshift bins. Colour gradients

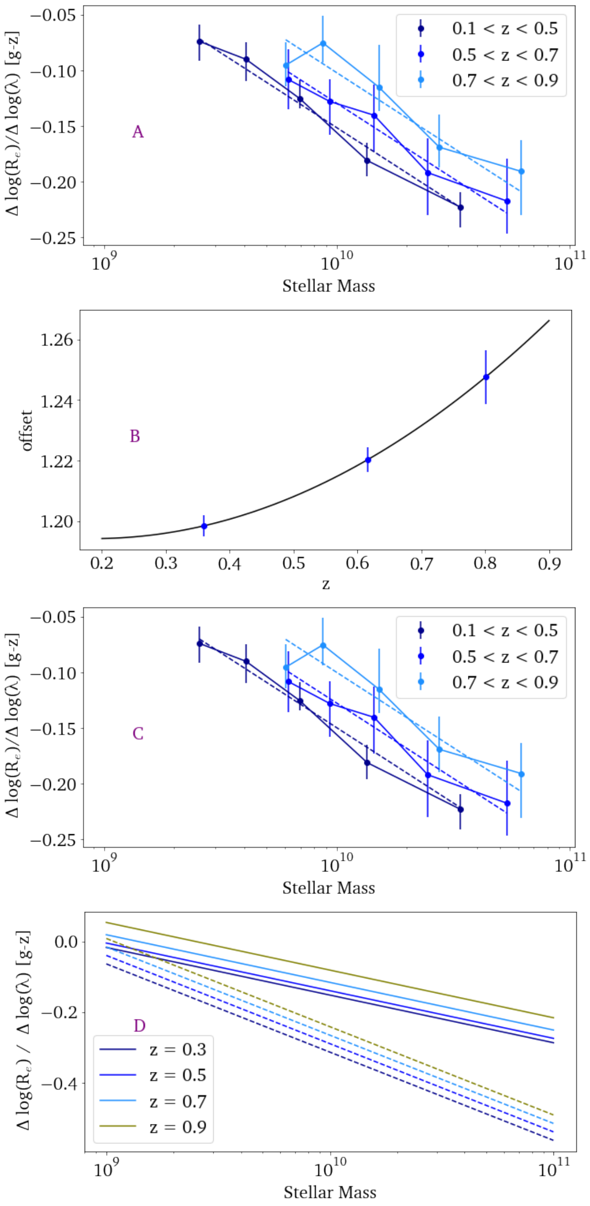

Figure 4.9: A: Wavelength dependence of size measurements of SFGs in redshift and mass bins. Colours indicate the redshift bins. Colour gradient of each galaxy is estimated using their size measurements in g and z bands, and the median gradient in each mass bin is shown as a data point. Errors on the median are estimated using bootstrapping. Dashed lines represent the linear fits to the wavelength gradient curves. B: Redshift evolution of the offsets from the linear fits given in Panel A. Best-fitting quadratic equation is shown in black. C: Wavelength gradient regression lines (dashed lines) using Equation 4.4.1. The slopes of these lines are from Panel A and intercepts are from Panel B. D: The wavelength dependence of R_e found in the study (solid lines) is shown along with the dependence found by van der Wel et al. (2014, dashed lines).

show similar mass dependence at different redshifts but the values of the colour gradients (offset or the y-intercept of the linear relation) vary with redshift. We study the redshift dependence of the colour gradients and find that a quadratic function can describe this dependence (Panel B). Combining the slope of the colour gradient in the size measurements from Panel A and the intercept/offset from Panel B, we express the colour gradient in SFGs in terms of stellar mass and redshift as

$$\frac{\Delta \log R_e}{\Delta \log \lambda} = 1.2 + 0.14z^2 - 0.05z - 0.135 \log(M_*/M_\odot). \tag{4.4.1}$$

Panel C shows this relation against the observed colour gradients in SFG size measurements. We compare this relation with the relation found by van der Wel et al. (2014) in Panel D. We do not find a strong mass dependence of the gradients as van der Wel et al. (2014) find. An added advantage in this study is that we use more than 11000 SFGs to estimate the colour gradient against 777 galaxies used by van der Wel et al. (2014). Furthermore, we have analysed galaxies in three redshift bins but van der Wel et al. (2014) have only two redshift bins at $z < 1$. We then estimate the sizes of SFGs in rest-frame 5000 $\AA$ as

$$R_e = R_{e,x} \left(\frac{1+z}{1+z_p} \right)^{\frac{\Delta \log R_e}{\Delta \log \lambda}}, \tag{4.4.2}$$

where $R_{e,x}$ denotes the size measurement in a given band and z_p is the pivot redshift in that band. The pivot redshift in a given band refers to the redshift at which we observe the

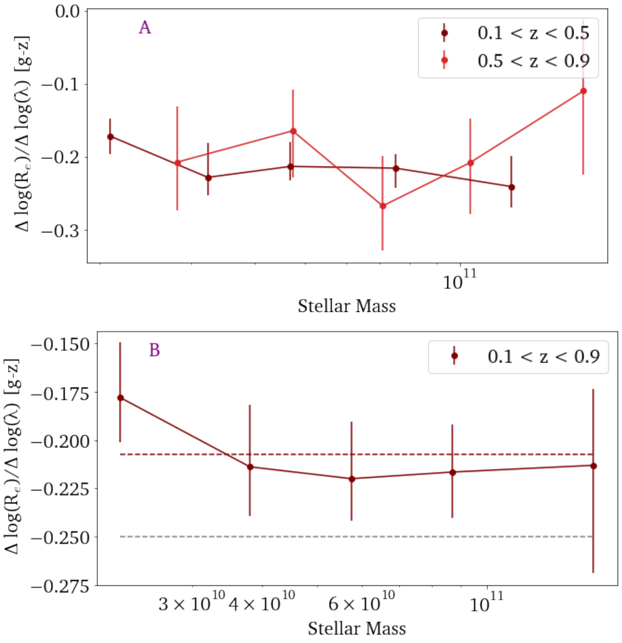

Figure 4.10: A: Wavelength dependence of size measurements of QGs in redshift and mass bins. We do not find any significant mass or redshift dependency. B: Average colour gradient in size measurements of QGs (red dashed line) by combining two redshift bins from the Panel A. The gradient given by van der Wel et al. (2014) is shown as a grey dashed line.

rest-frame 5000 $\AA$ of sources in that band.

Similar to van der Wel et al. (2014), we do not find any significant dependence of the colour gradient on mass or redshift for QGs (Panel A in Figure 4.10). Using the size measurements of about 2500 QGs in g and z bands at $0.1 < z < 0.9$, we find an average size gradient of $\Delta \log R_e / \Delta \log \lambda = -0.21 \pm 0.1$ against -0.25 given by van der Wel et al. (2014, Panel B). We then estimate the size of QGs in rest-frame 5000 $\AA$ using Equation 4.4.2.

4.4.2 Comparison with Literature

We compare galaxy size measurements in this thesis with earlier measurements from the literature. We do this comparison by using the measurements by van der Wel et al. (2014), who measure galaxy sizes in 3D-HST+CANDELS fields with a single Sérsic index in J-band. Similar to this thesis, they use GALFIT for the profile fitting process. Since our measurements and the ones presented in van der Wel et al. (2014) are in different bands, the comparison is made at the rest-frame 5000 $\AA$. We correct the J-band measurements in the literature to rest-frame 5000$\AA$ following the instructions given in van der Wel et al. (2014). For measurements of QGs in 3D-HST+CANDELS, the correction applied is

$$R_e = R_{e,J} \times \left(\frac{1+z}{2.5}\right)^{-0.25}, \tag{4.4.3}$$

and for SFGs,

$$\frac{\Delta \log R_e}{\Delta \log \lambda} = -0.35 + 0.12z - 0.25 \log \frac{M_*}{10^{10} M_\odot}, \tag{4.4.4}$$

where M_* is stellar mass of galaxies in solar masses. We match 989 galaxies (725 SFGs and 264 QGs) and compare the results with our i-band measurements corrected to 5000 $\AA$ (Figure 4.11). We can see that there is a good agreement between our ground-based (HSC) measurement of sizes of both SFGs and QGs with the published (HST) values.

There is no publicly available measurements of sizes for galaxies in our sample of CLASH clusters. Hence, we cannot compare these results with previous works directly.

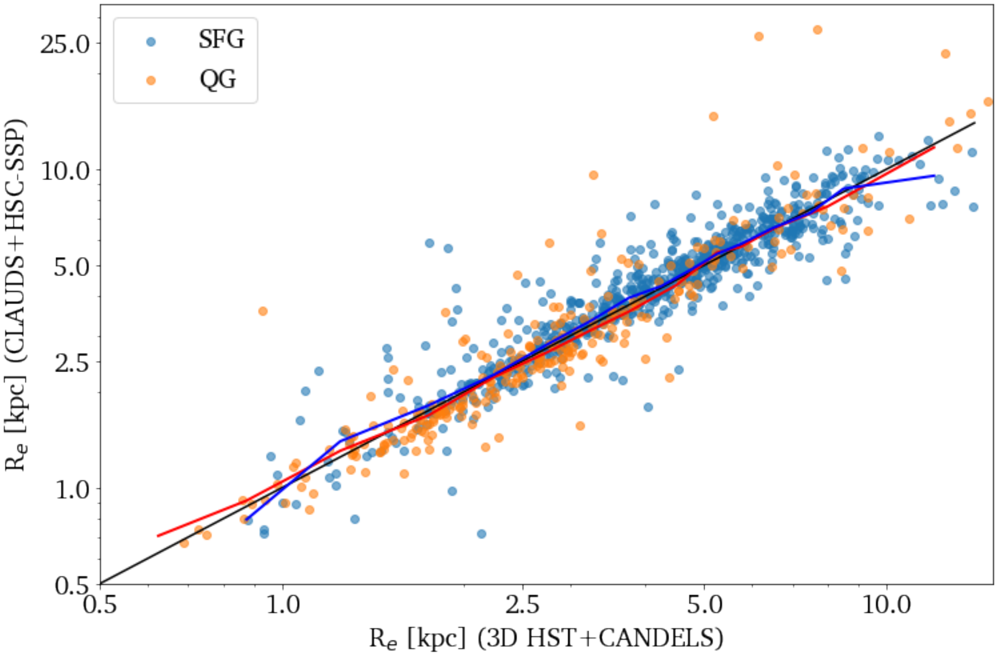

Figure 4.11: Comparison between size measurements (*i*-band) in the current study and size measurements by van der Wel et al. (2014), both corrected to 5000 Å. The blue line shows the median for SFGs and the red for QGs while the black line represents the 1:1 relation. There is a good agreement between the measurements in this study and the published size measurements by van der Wel et al. (2014) for both SFGs and QGs.

However, based on the agreement we observe in HSC data with van der Wel et al. (2014), we conclude that our HST measurements also can be trusted.

Chapter 5

Simulations

We test the robustness of our galaxy light profile fitting pipeline through simulations. Based on the results of these simulations, we introduce a magnitude limit on our analysis. Moreover, our simulations provide the estimate for the uncertainties present in our measurements (Section 4.4). Such estimation of uncertainty through simulations is important because GALFIT only provides random errors in the measurements. While estimating the uncertainties, the software assumes that the residual image obtained by subtracting the model from the image cutout is characterized by Poisson noise. Thus, the uncertainties obtained from GALFIT represent the total uncertainties only if the analytic models used to model galaxy light profiles describe the galaxy surface brightness profiles in the cutout perfectly and the residual image is uniform throughout. However, this is far from the case when it comes to the images of real galaxies. A single Sérsic profile cannot describe the complex structural details present in the light profiles of galaxies (Chapter 4). Additionally, the sky background itself is not always uniform especially if there is a presence of bright objects such as stars in the close vicinity of target galaxies in the image. Hence, we cannot assume that the random errors provided by GALFIT completely define the uncertainties present in our measurements. We rely on simulations to understand some of the systematic errors present in the measurements and explore their dependence on the properties of galaxy surface brightness profiles.

5.1 Simulation Process

The simulation pipeline is shown in Figure 5.1. In short, we generate mock/model galaxies with a selected set of Sérsic parameters and plant them in the real data images. We model these simulated galaxies using GALFIT in a similar fashion we follow to extract morphology of real galaxies described in Chapter 4. We then compare the fitting results with the real/input structural parameters of the simulated galaxies.

Naturally, the first step in this process is the selection of structural parameters for simulating mock galaxies. It is important that these artificial galaxies represent the real galaxy population in the COSMOS field. Therefore, we use the structural details of COSMOS galaxies from the Zurich Structure and Morphology Catalogue[1] (ZSMC). ZSMC contains HST ACS-f814w band based structural details of galaxies. There are two sets of measure-

---

[1] `https://irsa.ipac.caltech.edu/data/COSMOS/gator_docs/cosmos_morph_zurich_colDescriptions.html`

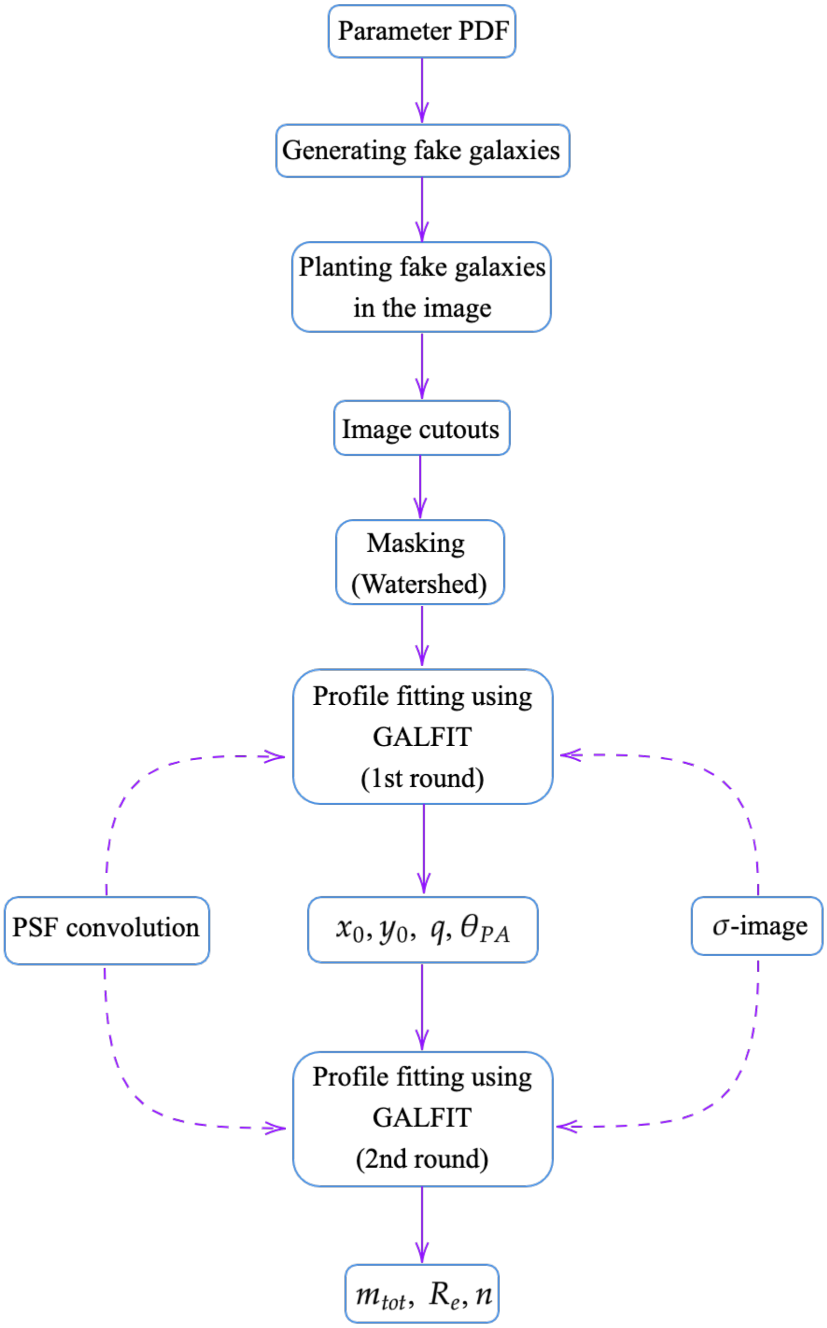

Figure 5.1: Simulation pipeline.

ments available in the catalogue: Zurich Estimator of Structural Types (ZEST, Scarlata et al. 2007) measurements and GIM2D measurements (Sargent et al. 2007). We choose GIM2D measurements for our parameter selection. These ZSMC GIM2D based structural parameters are derived from a single Sérsic profile fitting performed on galaxies. We estimate a multivariate probability distribution function (PDF) of GIM2D derived size (R_e), Sérsic index (n) and axis ratio (q) along with g, r, i, z and y[2] magnitudes from CLAUDS+HSC-SSP catalogue using kernel density estimation. However, we note that the ZSMC galaxies may not well represent the CLAUDS+HSC-SSP galaxies studied in this thesis, because the distributions of redshifts and magnitudes differ between both samples. We then randomly draw parameters from this PDF to simulate galaxies. We also make sure that we do not draw a parameter set where any of the parameters has a non-physical value (for example, $R_e < 0$ pixels). Figure 5.2 shows the distribution of parameters obtained from the parameter PDF.

In the next step, we model artificial galaxies with a randomly chosen parameter set from the PDF using GALFIT. We then plant these galaxies in the real image with a randomly chosen position angle (θ_{PA}) ranging from -89° to 89°. A random value of θ_{PA} ensures that they are placed in the images with orientations similar to the real galaxies. Once a galaxy is planted, we extract its morphology by fitting a single Sérsic profile to its light profile using GALFIT. This extraction process is the same as the galaxy fitting pipeline described in

---

[2] Although this thesis does not study galaxy morphology in the y-band, we include the band in the simulations to show that the pipeline performs poorly in the y-band.

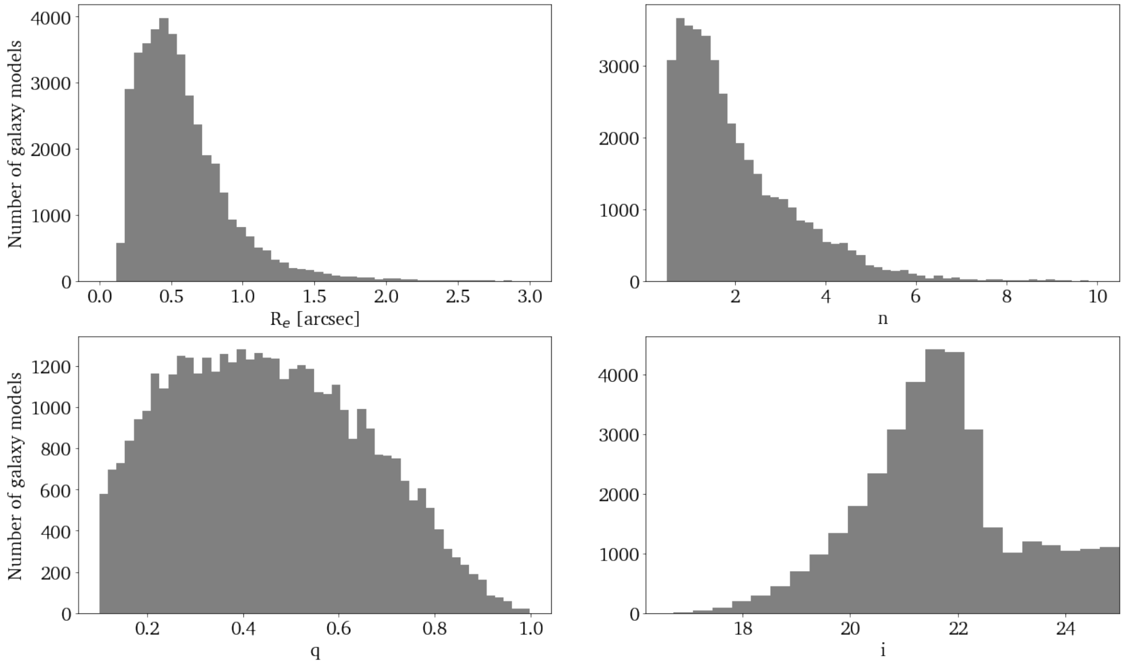

Figure 5.2: Distribution of Sérsic parameters drawn from multivariate PDF used for simulations. We use galaxy magnitudes from CLAUDS+HSC-SSP catalogue and other Sérsic parameters from ZSMC to generate the multivariate PDF.

Chapter 4. For HST images, we subtract the BCG model from the data images once a mock galaxy is placed in the real image. We then make an image cutout centred on the simulated galaxy. Cutout dimensions are 200×200 pixels for HSC images and 800×800 pixels for HST images, which are same as those used for galaxy size measurements described in Chapter 4. We then run GALFIT twice to extract the structural information of the planted mock galaxy. We perform these planting and fitting processes of artificial galaxies one at a time to avoid artificial overcrowding of galaxies in the data image. Examples of simulated galaxies and their best-fitting models obtained from the pipeline are shown in Figure 5.3.

We simulate and fit around 10,000 galaxy models in each band spread across 5 patches from tract 9813 in the CLAUDS+HSC-SSP COSMOS field. These five patches are selected to cover both the Deep and UltraDeep regions in the simulations. Two patches are in the UltraDeep region whereas the rest are at least partially in the Deep region. Figure 5.4 shows where these patches are located on the sky with respect to the UltraVISTA region and the HSC Deep and UltraDeep fields. Similarly, we simulate more than 20,000 galaxies spread across all five HST CLASH clusters. Radial positions of simulated galaxies in each cluster are shown in Figure 5.5.

One of the caveats of our simulation is that the artificial galaxies have light profiles that can be perfectly described by a single Sérsic profile. We acknowledge that these are not the case with real galaxies. As a result, our simulated galaxies do not represent the real galaxies in every structural detail. Hence, our estimations provide only a lower limit

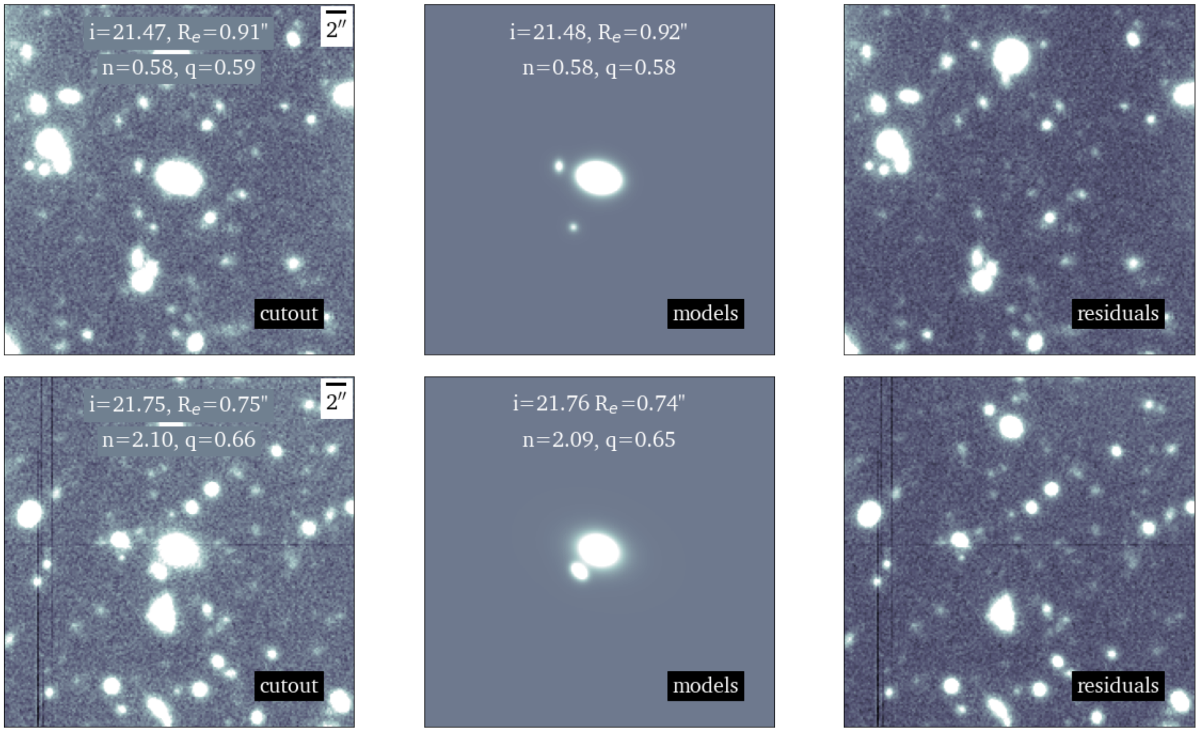

Figure 5.3: Examples of simulated galaxies in *i*-band. The left panel in each row shows the cutout image where the artificial galaxy is planted at the centre. Input parameters are given in the panel. The middle panel shows the best-fitting Sérsic models of the simulated galaxy and its neighbours in the image obtained using our fitting pipeline. Model parameters of the target galaxy are shown within the panel. The right panel shows the residual image.

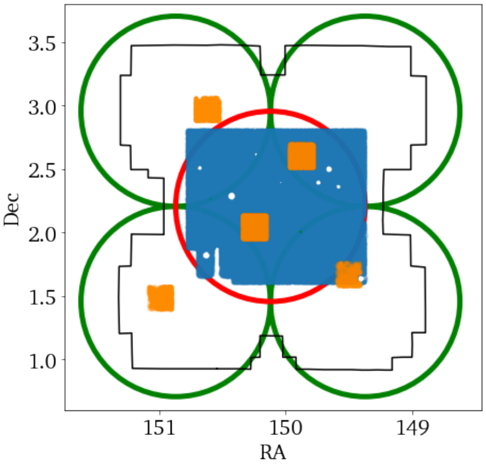

Figure 5.4: Orange regions show the CLAUDS+HSC-SSP patches selected for the simulations. The blue colour represents the UltraVISTA region and black borders indicate the CLAUDS+HSC-SSP COSMOS field. Red and green circles show the locations of the HSC Deep and UltraDeep field pointings.

on the uncertainties present in measurements of Sérsic parameters. Nonetheless, this estimate is sufficient for the present study as we are interested in the global features of galaxy morphology.

5.2 Simulation Results

5.2.1 CLAUDS+HSC-SSP Survey

We examine output parameters obtained from simulations and compare them with input parameters to see how robust our pipeline is in recovering the original values. Figure 5.6 shows how the GALFIT derived output parameter values compare with input values for *i*-band data. A visual analysis of these plots tells us that some of the fitting processes failed as

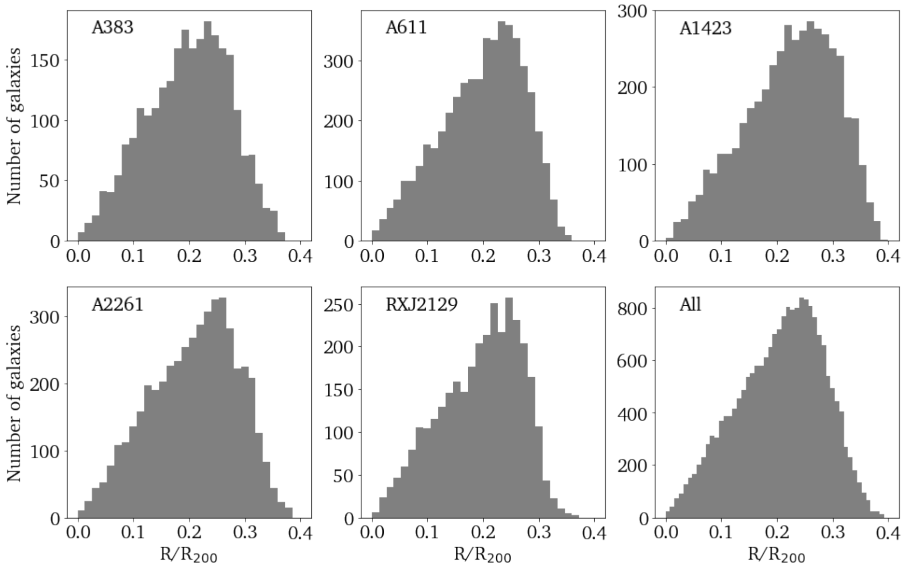

Figure 5.5: Histograms showing the radial distribution of simulated galaxies planted in each HST CLASH cluster. Radial distances from the centres of the clusters are normalised by the virial radii of the clusters. The final panel shows the same by combining all clusters. This amounts to a total of $\sim 20,000$ galaxies.

the output parameters occupy the edges of the permitted parameter space. Hence, we apply the same conditions described in Section 4.4 to identify outliers (shown in red in Figure 5.6). They represent less than 6% of all data points in the Figure.

To investigate the robustness of the pipeline, we further define simulation success ratio as

$$\text{Success ratio} = 1 - \frac{\text{Number of outliers}}{\text{Total number of simulated galaxies}} \tag{5.2.1}$$

and we plot this ratio in all the five HSC bands in Figure 5.7. A success ratio of 0.9 indicates that 10% of the simulated galaxies end up being outliers in the fitting results. We notice

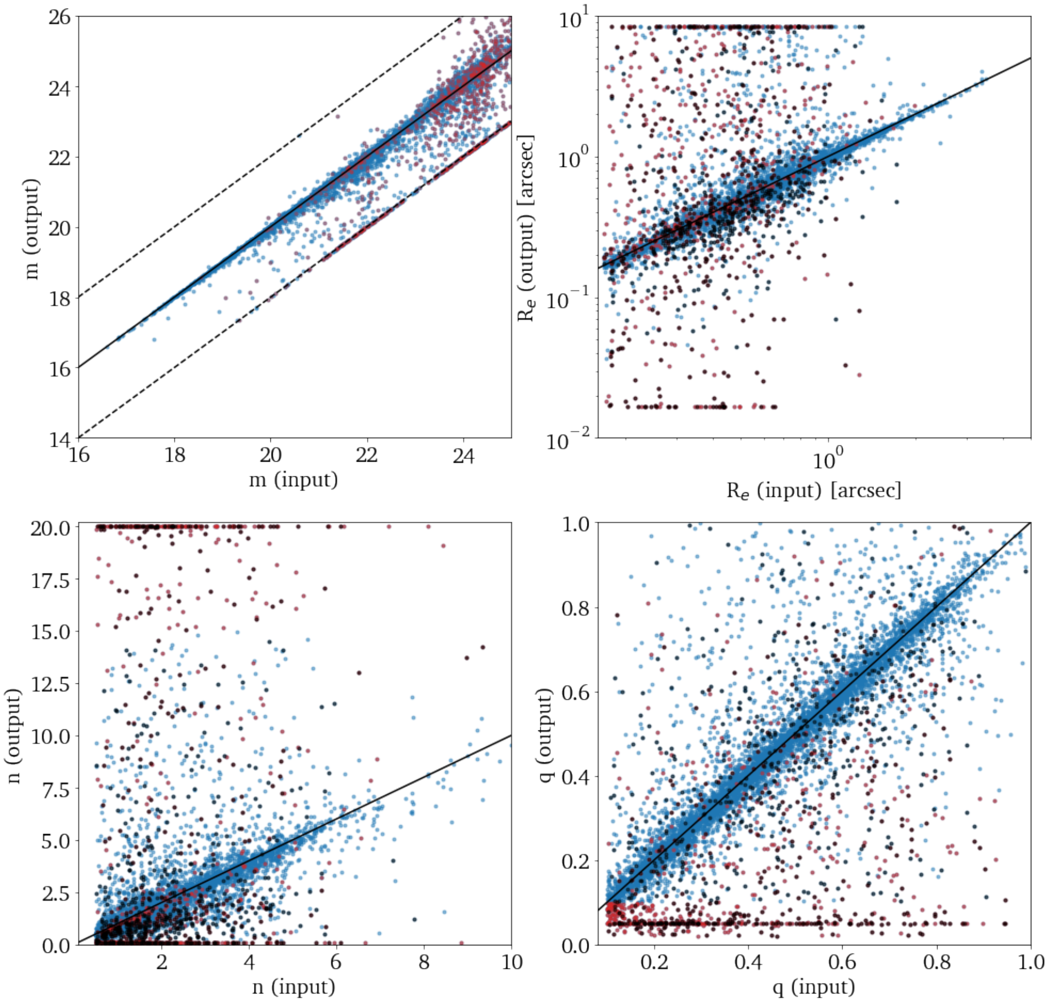

Figure 5.6: Comparison between simulation input and output parameters in *i*-band. Red colours indicate the outliers identified (Section 5.2.1). Black dots represent galaxies with input magnitude fainter than 24 mag. Black lines represent the 1:1 relation between input and output values. Black dashed lines in the first panel represent a magnitude difference of ±2 AB.

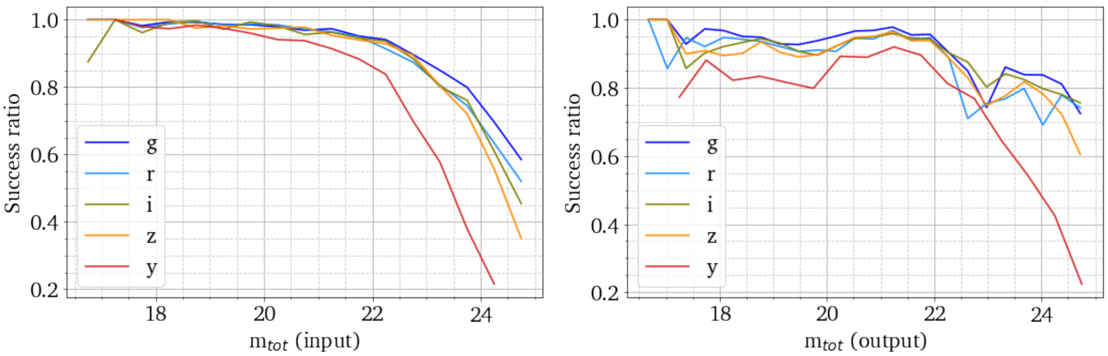

Figure 5.7: Simulation success ratio (Equation 5.2.1) as a function of input (left) and output (right) magnitudes in CLAUDS+HSC-SSP bands.

that the success ratio falls below 0.7 beyond 24th (input) magnitude in HSC *i*-band. Hence, we limit our study to galaxies brighter than 24th magnitude. However, in the real data, our analysis is based on the output parameter space, and in the output parameter space, the outlier fraction is below 20% up to 24th (output) magnitude in the HSC bands except the *y*-band. It is also important to note that our pipeline performs poorly in *y*-band compared to all other bands. This is as expected because *y*-band data is comparatively shallower (25 AB against 27 AB in *g*-band). Hence, we do not use *y*-band data to study galaxy morphology in this thesis. We also separately analyse the success ratio of simulations in five chosen patches (Figure 5.8). Clearly, at fainter input magnitudes, the pipeline performs better in patch 4c3, which is at the centre of the UltraDeep field.

One of the motivations for this simulation is to quantify the systematic uncertainties present in our estimates of galaxy light profile parameters based on single Sérsic profile fitting. These uncertainties depend on the intrinsic properties of galaxy light profiles themselves. For example, the robustness of our code may depend on how disky or concentrated

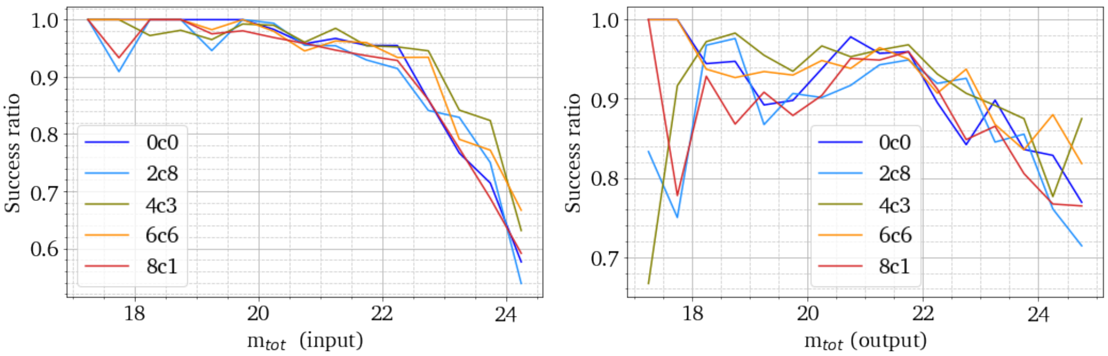

Figure 5.8: Simulation success ratio in the *i*-band as a function of input (left) and output (right) magnitudes in the five HSC patches selected for simulations.

galaxy profile is. Therefore, we need to identify these systematic uncertainties based on the inherent properties of galaxies. It is possible to do so in simulations because we know the actual (input) parameters of artificial galaxies we generated. However, we cannot apply this to the real data where we do not know the inherent structural parameter values of the real galaxies. Hence, we have to base our uncertainty analysis on output parameters. In this process, we use the relative differences in parameters between their input and output values to quantify uncertainties. The relative difference for a given parameter x is defined as

$$\Re_d(x) = \frac{x(\text{input}) - x(\text{output})}{x(\text{output})}. \tag{5.2.2}$$

We then analyse the distribution of $\Re_d(x)$ as a function various output parameters (m_{tot}, R_e and n). For this analysis, we divide the simulation results into nine output magnitude bins, five output size bins and five output Sérsic index bins (Table 5.1)

We then analyse the distribution of $\Re_d$ of m_{tot}, R_e, n and q in each bin. Figure 5.7 shows

m_{tot}	R_e [pix]	n
-17	0-0.5	0.2-1
17-18	0.5-1	1-2
18-19	1-1.5	2-4
19-20	1.5-2	4-8
20-21	2-	8-15
21-22		
22-23		
23-24		
24-		

Table 5.1: Bins in the output Sérsic parameter space of galaxies in CLAUDS+HSC-SSP simulations to estimate measurement uncertainties.

these distributions for *i*-band using violin plots[3]. Violin plots for other HSC bands are given in Appendix A. We consider 16th and 84th percentiles of $\Re_d$ as the lower and upper limits of the uncertainties of a measured Sérsic parameter (k) in a given output parameter (x) bin. For example, in a given output parameter bin of m_{tot} (x), we estimate the uncertainties present in the output parameters (k): m_{tot}, R_e, n and q. However, for computational reasons, we calculate an average distance to these percentiles from the median value of $\Re_d$ to estimate uncertainties,

$$\sigma_x(k) = \frac{84^{\text{th}}\ \text{percentile} - 16^{\text{th}}\ \text{percentile}}{2}. \tag{5.2.3}$$

Thus, for a given galaxy, we estimate $\sigma_x(k)$ based on bins in output values of m_{tot}, R_e and

---

[3] The width of a violin plot, which is smoothed by a kernel density estimator, shows the density distribution of the data ($\Re_d$), and its length shows the extent of this distribution.

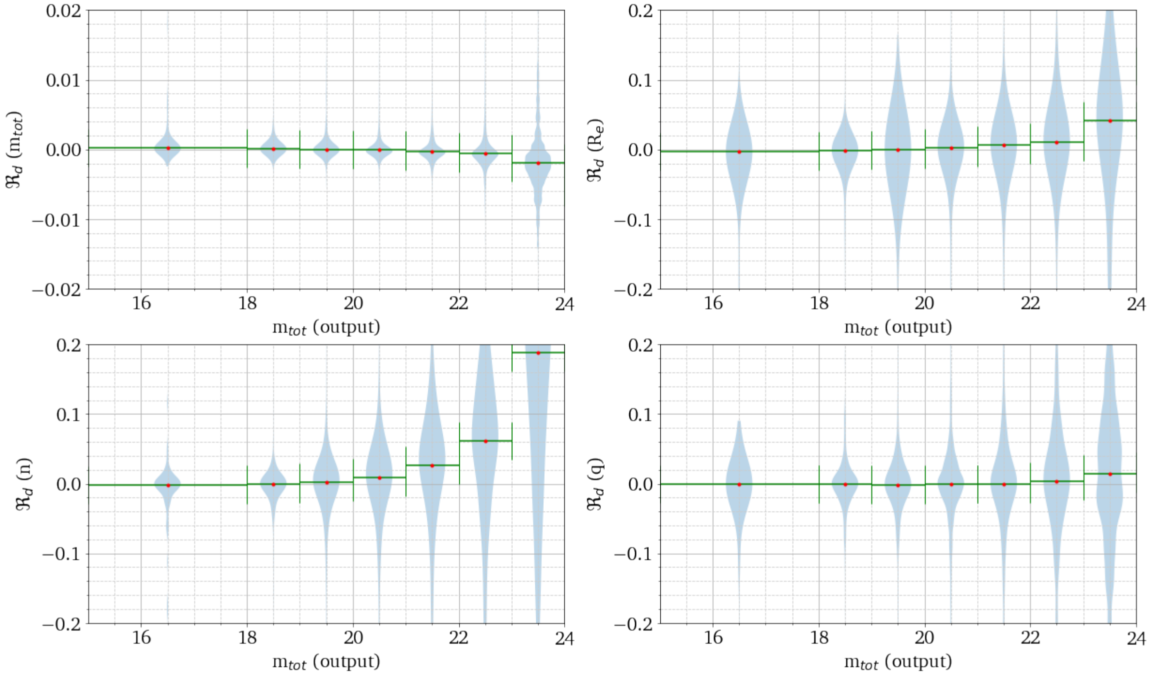

A

Figure 5.9: Violin plots of the relative difference ($\Re_d$) in parameters as a function of output parameters in *i*-band. The width of the violin plots shows the distribution of $\Re_d$ and their length represents the extent of this distribution. Red dots denote the median values of $\Re_d$ in a given output parameter bin while horizontal green error bars indicate the width of each bin. A: $\Re_d$ as a function of output magnitude; B: $\Re_d$ as a function of output size; C: $\Re_d$ as a function of output Sérsic index. Note that the scaling in y-axis is not uniform across the panels.

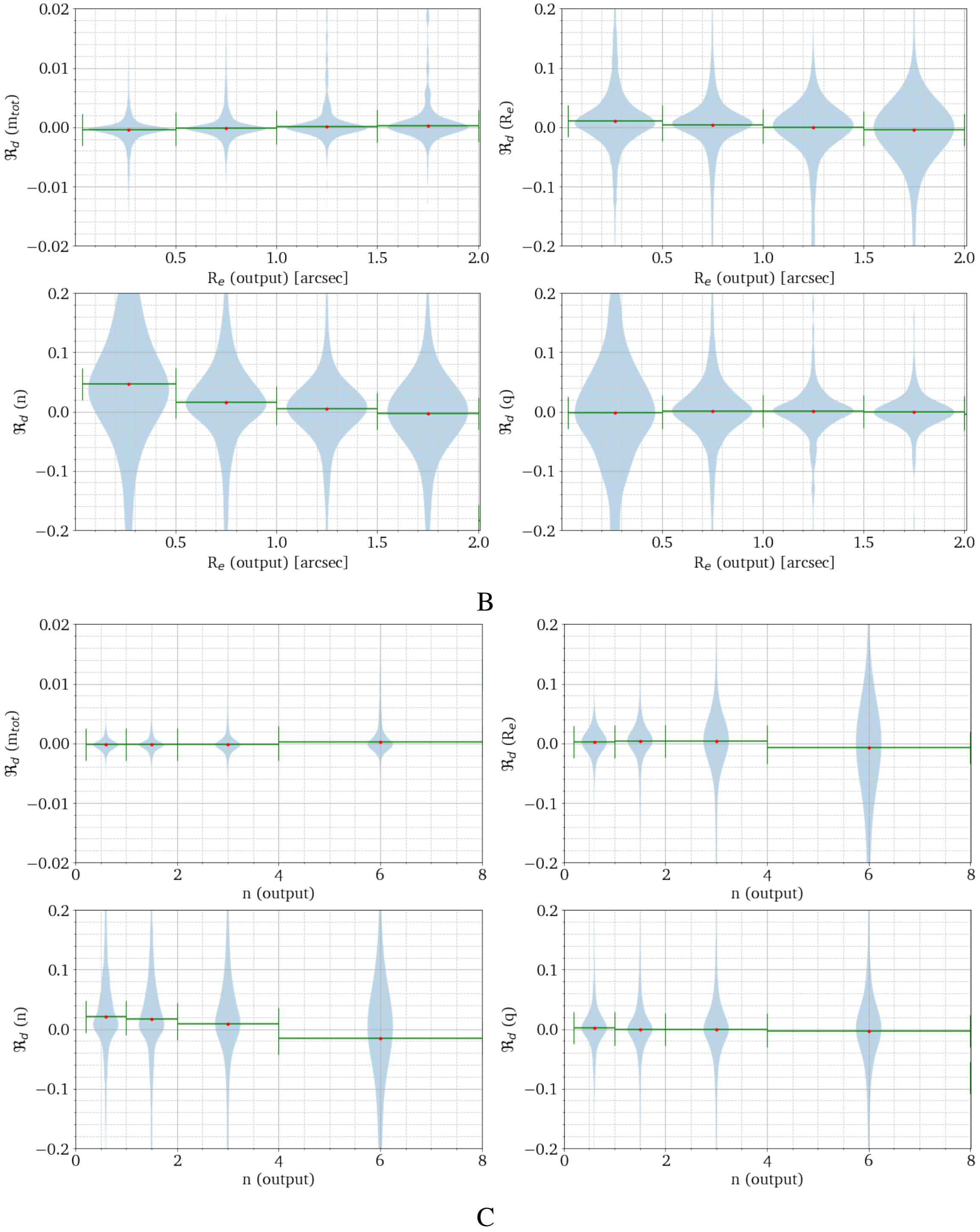

Figure 5.9: Violin plots of the relative difference ($\Re_d$) in parameters as a function of output parameters in *i*-band (continued).

n. We then compute the total systematic uncertainty present in the measurement of a Sérsic parameter k of a galaxy as

$$\sigma_{sys}(k) = \sqrt{\sigma_m^2(k) + \sigma_{R_e}^2(k) + \sigma_n^2(k)}. \tag{5.2.4}$$

We recognize that σ_{R_e} and σ_n are not independent of each other. Nonetheless, we treat them as separate entities in the current study to simplify calculations. We will explore the covariance in our future works. Currently, the total uncertainty present in the measurement of a Sérsic parameter is calculated as

$$\sigma(k) = \sqrt{\sigma_{ran}^2(k) + \sigma_{sys}^2(k)}, \tag{5.2.5}$$

where σ_{ran} is the random uncertainty obtained from GALFIT.

Violin plots (Figure 5.9) show that the estimation of the magnitude is robust for all types of galaxies. The pipeline is also generally successful in measuring galaxy sizes and axis ratios. However, the Sérsic indices are not recovered with the same accuracy as other parameters especially at fainter magnitudes ($m_{tot} > 22$). The algorithm tends to underestimate the Sérsic index of galaxies at these magnitudes. We need to consider this result when we analyse the evolution in Sérsic index of galaxies.

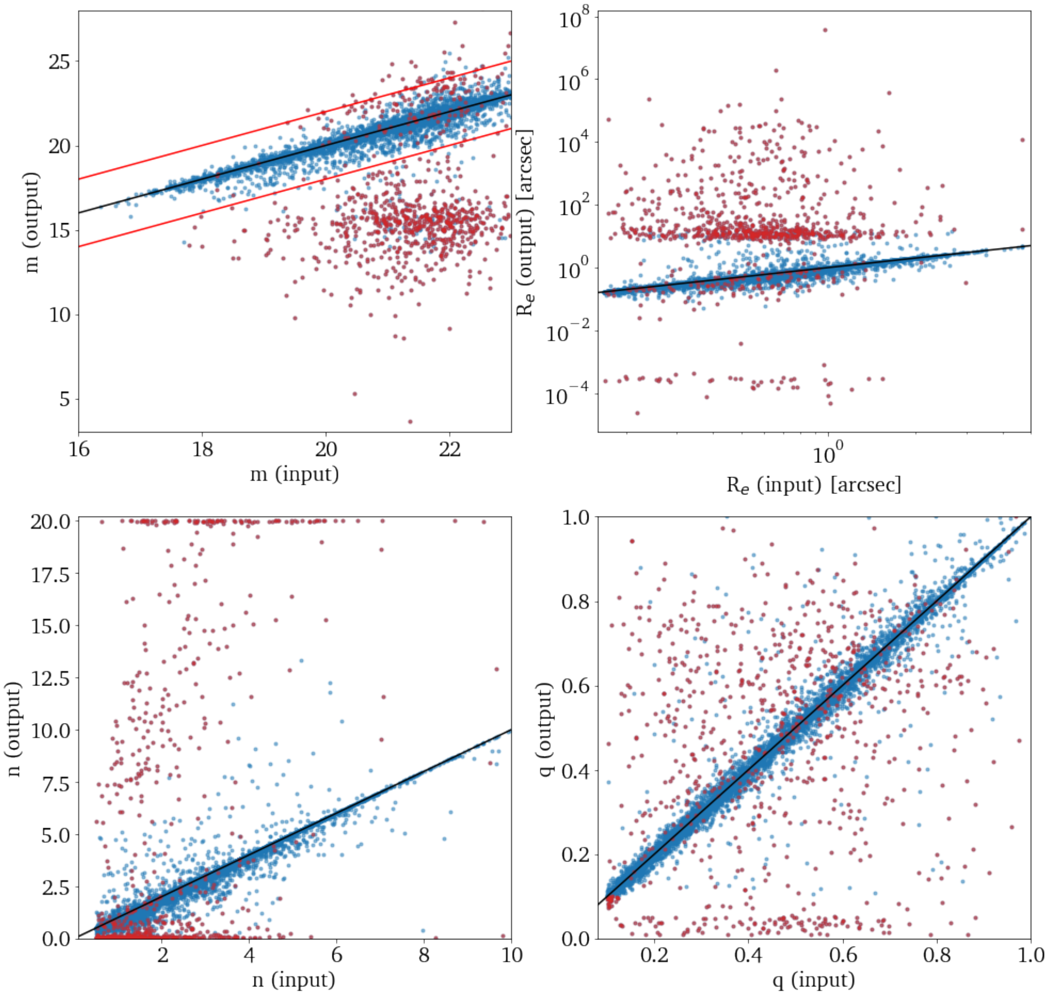

Figure 5.10: Comparison between simulation input and output parameters in HST images. Red colours indicate the identified outliers (Section 5.2.2). Black lines represent the 1:1 relation between input and output values. Red lines in the first panel represent a magnitude difference of ±2 AB.

5.2.2 HST CLASH Survey

The results of simulations of HST images are shown in Figure 5.10, where output parameters are compared with input values. Generally, our pipeline successfully recovers the input values. However, similarly to HSC simulations, distributions of output parameters from the simulations on HST data show outliers. Thus, we trim our results using the following cuts in the output parameters:

$0.2 < R_e < 500$ pixels,

$0.2 < n < 15$,

$0.1 < q < 1$,

and we identify all galaxies which do not satisfy these conditions as outliers. We have shown them in the figure as red data points. These outliers represent a total of $\sim 4\%$ of all simulated galaxies. A major difference between HSC and HST simulations is that we do not use a constraint file while running GALFIT on HST data, because GALFIT does not fail generally while fitting the HST galaxies with a Sérsic profile even without a constraint file. There are $\sim 4\%$ galaxies whose output magnitudes are beyond ± 2 AB from their input values (the first panel in Figure 5.10). However, we are successful in identifying 90% of them using the above-mentioned cuts in the output values of R_e, n and q without any information on their input magnitudes. Many of the outliers in HST data have their magnitudes overestimated (the first panel in Figure 5.10). We define the success ratio

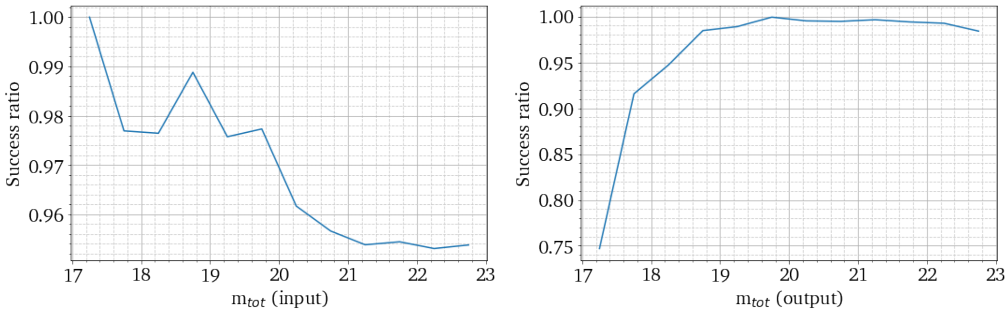

Figure 5.11: Simulation success ratio as a function of input (left) and output (right) magnitudes in the HST f814w band.

similar to simulations on the HSC data, and this is shown as a function of input magnitudes in the left panel of Figure 5.11. We have a success ratio of more than 95% up to 23$^{\text{rd}}$ magnitude in the HST ACS-f814w band.

Uncertainty estimations are performed similarly to those in HSC simulations. However, we consider an additional term in the total uncertainties: σ_r. This parameter refers to the systematic uncertainty present in the measurements based on the position of a galaxy in the image with respect to the position of the BCG. We incorporate this environmental information into uncertainty estimation, because the number density of galaxies may vary depending on the radial distance from the BCGs. Hence, we have four bins in radial distance from the BCG, six output f814w magnitude bins, five output size bins and five output Sérsic index bins (Table 5.2).

We estimate the systematic uncertainty present in parameter k as

$$\sigma_{sys}(k) = \sqrt{\sigma_r^2(k) + \sigma_m^2(k) + \sigma_{R_e}^2(k) + \sigma_n^2(k)}. \tag{5.2.6}$$

R/R_{200}	m_{tot}	R_e [$''$]	n
$0.0-0.1$	-18	$0.0-0.5$	$0.2-1$
$0.1-0.2$	$18-19$	$0.5-1.0$	$1-2$
$0.2-0.3$	$19-20$	$1.0-1.5$	$2-4$
$0.3-0.4$	$20-21$	$1.5-2.0$	$4-8$
	$21-22$	$2.0-$	$8-$
	$22-$		

Table 5.2: Bins in projected radial distance from the BCG and the output Sérsic parameters of galaxies in HST CLASH simulations to estimate measurement uncertainties.

The total uncertainty is then calculated using Equation 5.2.5. The distributions of $\Re_d$ for various parameters are shown as violin plots in Figure 5.12.

The algorithm performs better in estimating the Sérsic parameters in HST data (Figure 5.12) compared to CLAUDS+HSC data (Figure 5.9). The performance of the algorithm is robust in measuring the magnitude, size, Sérsic index and axis ratio of galaxies of all types and at all distances from the cluster centre. However, we note that the radial distance from the cluster centre might affect the estimation of the parameters in the real data because of the presence of the BCG. In the current simulations, we model the BCG before planting a mock galaxy in the image and subtract these pre-estimated BCG model from the data once a mock galaxy is planted. We will improve our simulations in the future by modelling BCGs after planting the mock galaxies to understand how the modelling of the BCG affects the light profiles of its neighbouring galaxies.

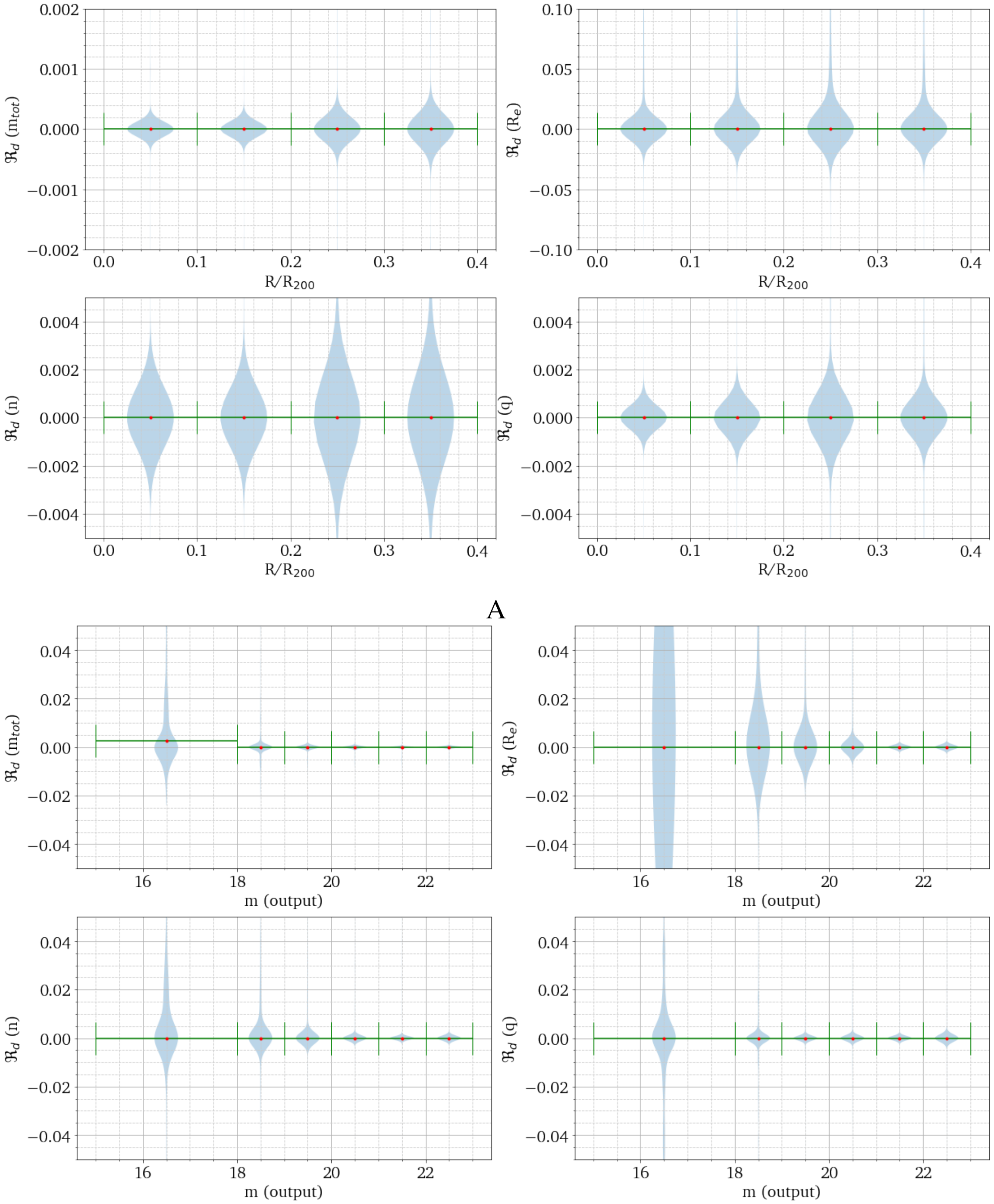

A

B

Figure 5.12: Violin plots of the relative difference ($\Re_d$) in parameters as a function of output parameters in the HST f814w band. A: $\Re_d$ as a function of radial distance from BCG; B: $\Re_d$ as a function of output magnitude; C: $\Re_d$ as a function of output size; D: $\Re_d$ as a function of output Sérsic index. Note that the scaling in y-axis is not uniform across the panels.

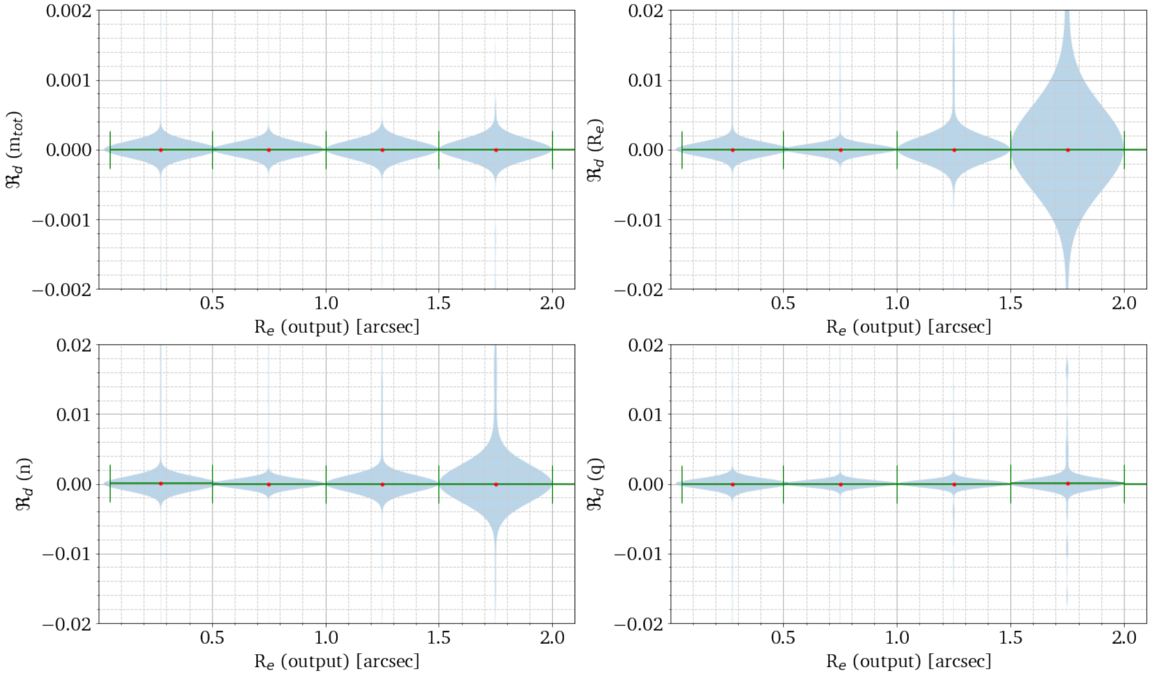

C

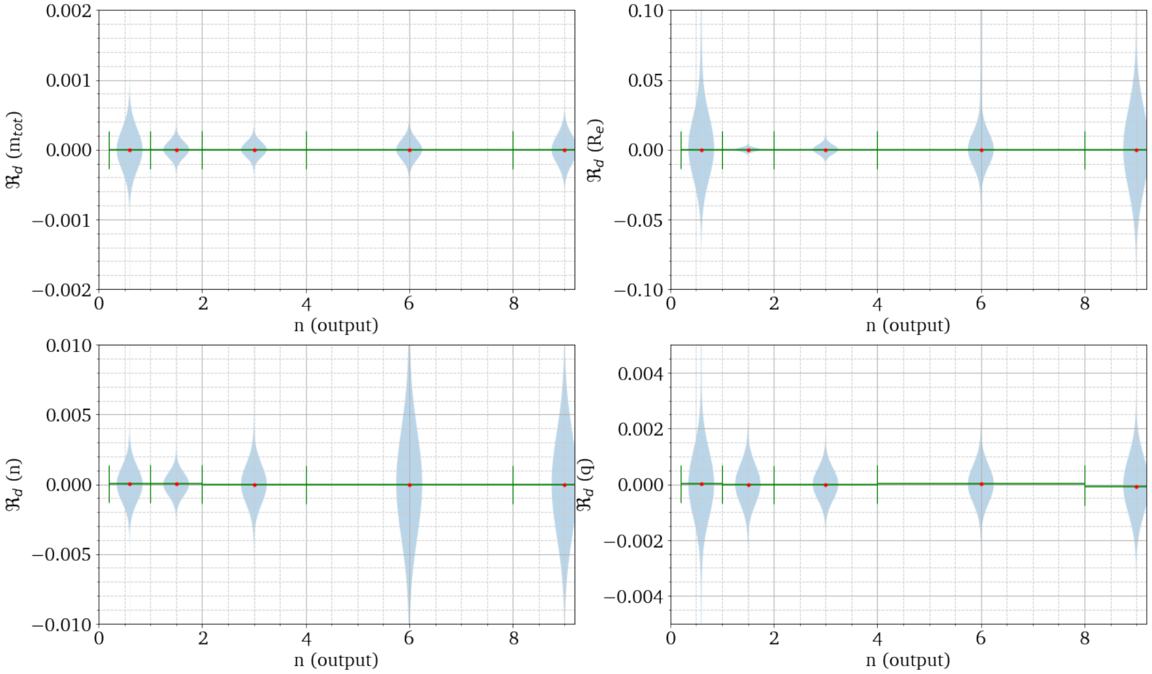

D

Figure 5.12: Violin plots of the relative difference ($\Re_d$) in parameters as a function of output parameters in the HST f814w band (continued).

Chapter 6

Results

6.1 Size-Mass Relation

Numerous studies show that the dependence between galaxy size and stellar mass is different for SFGs and QGs (eg., Shen et al. 2003; Williams et al. 2010; van der Wel et al. 2014; Lange et al. 2015; Faisst et al. 2017; Roy et al. 2018; Mowla et al. 2019b; Matharu et al. 2019, 2020). We also see this dependence in our CLAUDS+HSC-SSP COSMOS data. Figure 6.1 shows how median galaxy sizes at rest-frame 5000 $\AA$[1] evolve with stellar mass for both SFGs (blue points) and QGs (red points) across five different redshift bins. The larger data points represent median sizes in various mass bins. There is a clear difference between SFGs and QGs where SFGs tend to have larger sizes compared to QGs. In agreement with previous studies, the linear relation between galaxy size and stellar mass in log-log space

---

[1] We estimate the sizes in rest-frame 5000 $\AA$ using Equation 4.4.2 (Section 4.4.1).

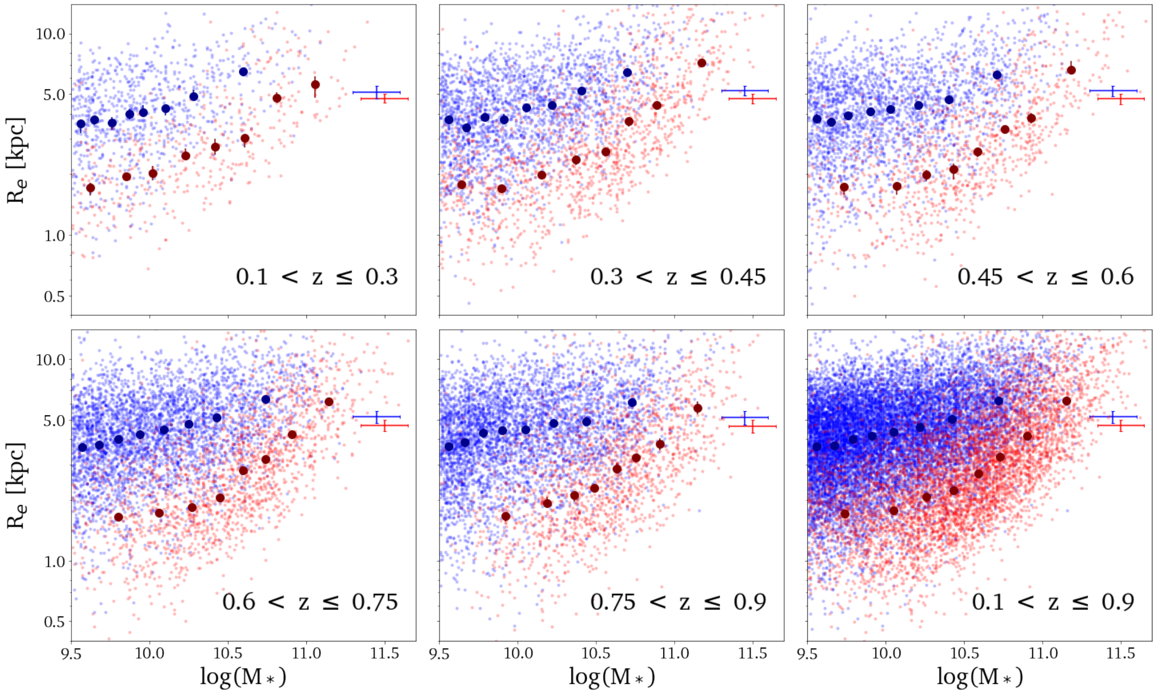

Figure 6.1: Relation between size and stellar mass of galaxies in CLAUDS+HSC-SSP COSMOS in *i*-band corrected to rest-frame 5000 $\mathring{A}$. Stellar masses are taken from Muzzin et al. (2013a) as described in Section 2.1.2. Masses are shown in units of solar mass ($M_\odot$). The first five panels are for galaxies in five different redshift bins whereas the last panel shows the relation for the whole sample. SFGs are shown in blue and QGs in red. Median sizes in equally populated mass bins are denoted by larger data points. Error bars on the median sizes are obtained through bootstrapping. Error bars in each panel show the median uncertainty present in the measurement of size and mass of SFGs (blue) and QGs (red).

has a significantly shallower slope for SFGs than for massive QGs[2]. A weaker relation indicates that the surface mass density of SFGs ($\log \Sigma_{M_*} = \log(M_*) - 2\log R_e - log(2\pi q)$) increases significantly with mass. However, the size-mass relation is complex for QGs: massive galaxies have a steeper relation while the low mass end shows a shallow or no dependence on mass. Thus, the surface mass density of QGs increases until a certain stellar mass ($\sim 2 \times 10^{10}$ $\mathrm{M}_\odot$) after which the surface mass density decreases with increasing mass ($\Sigma_{M_*} \propto M_*^{-0.4}$). Shen et al. (2003) show that a similar complex relation exists for SFGs as well; they found a steeper size-mass relation for SFGs with masses $10.6 < \log(M_*/M_\odot) < 12$ in the local universe ($z < 0.3$). Our data also hint at a slightly steeper relation towards the highest mass bin ($10.54 < \log(M_*/M_\odot) < 11.45$) for SFGs but due to lack of very massive SFGs in our current data we cannot analyse them separately until we expand our analysis to the full 18.6 deg^2 of CLAUDS+HSC-SSP survey (Section 2.1). Hence, we treat SFGs as a single group in this study.

We analyse the size-mass relation of both SFGs and QGs by assuming a linear relation in log scale,

$$\log R_e(m_*) = \log A + \alpha \log m_*, \tag{6.1.1}$$

where

$$m_* = \frac{M_*}{5 \times 10^{10} M_\odot}, \tag{6.1.2}$$

---

[2] Massive QGs have stellar mass higher than a pivot mass, M_p. We will discuss the pivot mass in Section 6.1.2 in detail.

and α is the slope. The y-intercept, $\log A$, gives the size of a galaxy with the normalization mass, $5\times10^{10}M_{\odot}$. Previous studies such as van der Wel et al. (2014) and Mowla et al. (2019b) also use this normalization mass in their analysis, which makes the comparison between the results straightforward. While fitting the relation, we apply a Bayesian approach to include uncertainties in both size and mass estimates (see Kelly 2007). By using this technique, we assume,

$$\eta = \log A + \alpha\xi + \varepsilon, \tag{6.1.3}$$

where

$$\xi = \log m_* - \mathrm{xerr},$$

$$\eta = \log R_e(m_*) - \mathrm{yerr},$$

and ε is the intrinsic random scatter about the regression line. η is a dependent variable while ξ is an independent variable. xerr and yerr are random errors sampled from a normal distribution with the width equal to the uncertainties (σ_{m_*} and σ_{R_e}) in the measurement of mass and size respectively. We assume the 1-σ uncertainty in mass, $\sigma_{\log m_*}$ to be 0.15 dex quoted by van der Wel et al. (2014) because they also use the same mass measurements (Muzzin et al. 2013a) for their analysis. We then fit a linear regression model with a Bayesian approach using PYTHON package, LINMIX[3]. The algorithm relies on Markov chain Monte Carlo (MCMC) methods to obtain best-fitting parameters. Figure 6.2 shows

---

[3] `https://linmix.readthedocs.io/en/latest/src/linmix.html`

the best-fitting linear regression lines for SFGs and massive QGs in five redshift bins (Sections 6.1.1 and 6.1.2). We use the size (R_e) measurements at rest-frame 5000 $\AA$ while fitting the size-mass relation. Best-fitting parameters (intercept $\log A$ and slope α) of the regression lines are shown in Figure 6.3. The figure also shows results from the CANDELS survey (van der Wel et al. 2014) and the COSMOS-DASH survey (Mowla et al. 2019b), which - like our results - are based on size estimation at rest-frame 5000 $\AA$.

The redshift evolution of the intercept is significant. We fit this evolution in the intercept as

$$R_e(M_* = 5 \times 10^{10} M_\odot) = A(1+z)^\beta \tag{6.1.4}$$

and display the best-fitting curves in the upper panel in Figure 6.3. Different lines indicate how we obtain the size-mass relation: solid lines when we use i-band corrected to rest-frame 5000 $\AA$ and dashed lines when we use a combination of r, i and z bands. Although both dotted dash line and solid line in red are obtained using i-band corrected to rest-frame 5000 $\AA$, the two size measurements are based on two size-mass relations for QGs above different pivot masses (Section 6.1.2). Tables 6.1 and 6.2 list the best-fitting parameters of the size-mass relation and size evolution of SFGs and QGs respectively.

One of the advantages of this study over many previous studies is the wavelength coverage of the survey. The HSC r, i and z bands cover rest-frame 5000$\AA$ at $0.1 < z < 0.9$. Based on the wavelength range of the HSC broadbands, we divide our data into three redshift ranges: $0.1 < z \leq 0.38$, $0.38 < z \leq 0.69$ and $0.69 < z \leq 0.9$. We use the r-band galaxy

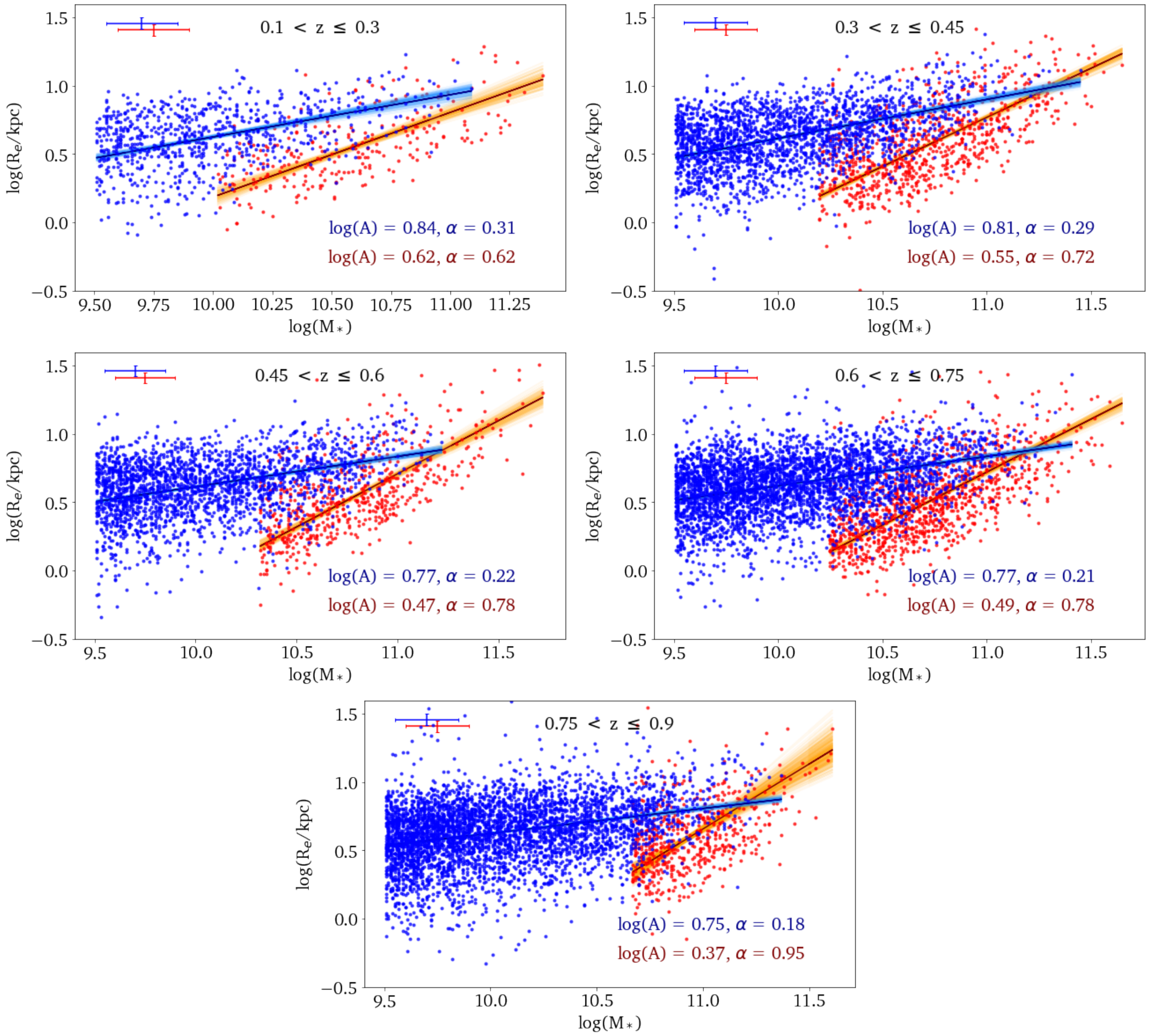

Figure 6.2: Linear fits to the size-mass relations of galaxies in CLAUDS HSC-SSP COSMOS at rest-frame 5000$\AA$. We measure sizes in *i*-band images and apply the correction described in Section 4.4.1. Blue and maroon lines represent the best-fitting linear regression. Its parameters are given in each panel. We only consider massive QGs ($M_* > M_p$) selected using Equation 6.1.6 (Section 6.1.2). Light blue and orange lines show random draws from the posterior from MCMC for SFGs and QGs respectively. Median errors in the measurement of size and mass for SFGs (blue) and QGs (red) are shown in the top left corner of each panel. Uncertainties on fitting parameters are given in Tables 6.1 and 6.2.

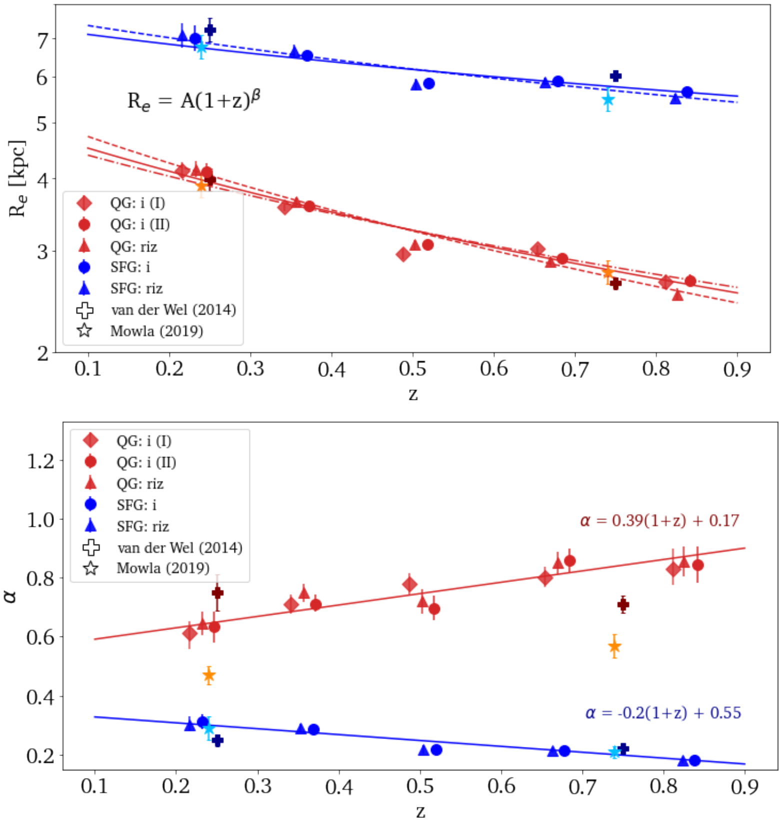

Figure 6.3: Redshift evolution of best-fitting parameters from Figure 6.2: intercept (upper panel) and slope (lower panel). Red represents QGs while blue is for SFGs. Different symbols are used to represent the method used to obtain the size-mass relation (Sections 6.1.1 and 6.1.2 for details). All sizes are in rest-frame 5000 *Å* based either on corrected *i*-band data (*i*) or on a combination of data from *r*, *i* and *z* bands (*riz*). Parameters from the literature are also shown. Some of the data points (triangles, diamonds and stars) are slightly shifted towards the left for clarity. The curves in the upper panel represent the best-fitting power law to the redshift evolution of average galaxy size for $M_* = 5 \times 10^{10}$ M$_\odot$. The dashed curve represents the evolution obtained using *riz* and the solid curve using the *i*-band. The dotted dash line denotes the size evolution obtained for QGs using Method I as described in Section 6.1.2. The lines in the lower panel represent the best-fitting linear relation between slope (circular data points) and redshift.

surface brightness fitting results for the first redshift bin, the *i*-band for the second and the *z*-band for the third to ensure that for each galaxy the selected band brackets the rest-frame 5000$\AA$. This multi-band approach does not need any wavelength correction unlike using a single band (*i*-band). Hence, we can use it to test the validity of the wavelength correction we estimated in Section 4.4.1 by fitting the size-mass relation using the combination of rest-frame 5000 $\AA$ size measurements obtained from the *r*, *i* and *z* bands, as appropriate for a given redshift. The results are shown in Figure 6.3 as open triangles and the values of the best-fitting parameters are given in Tables 6.1 and 6.2. A nearly perfect agreement between multi-band results and results from *i*-band corrected to rest-frame 5000 $\AA$ validate the wavelength correction introduced in this study. Size-mass relation plots in the five redshift bins using multi-band data are given in Appendix B.

Star-forming Galaxies				
z	i		riz	
	Intercept	**slope (α)**	**Intercept**	**slope (α)**
$0.10-0.30$	$0.845^{+0.043}_{-0.021}$	$0.312^{+0.052}_{-0.027}$	$0.849^{+0.041}_{-0.021}$	$0.303^{+0.05}_{-0.023}$
$0.30-0.45$	$0.816^{+0.018}_{-0.009}$	$0.287^{+0.026}_{-0.013}$	$0.823^{+0.02}_{-0.011}$	$0.291^{+0.029}_{-0.016}$
$0.45-0.60$	$0.766^{+0.02}_{-0.01}$	$0.219^{+0.025}_{-0.013}$	$0.765^{+0.02}_{-0.01}$	$0.218^{+0.027}_{-0.013}$
$0.60-0.75$	$0.771^{+0.011}_{-0.006}$	$0.215^{+0.016}_{-0.008}$	$0.769^{+0.012}_{-0.007}$	$0.215^{+0.016}_{-0.009}$
$0.75-0.90$	$0.753^{+0.013}_{-0.006}$	$0.183^{+0.017}_{-0.008}$	$0.742^{+0.013}_{-0.006}$	$0.181^{+0.018}_{-0.009}$
A	7.41 ± 0.42		7.76 ± 0.49	
β	-0.45 ± 0.11		-0.56 ± 0.12	

Table 6.1: Details of the best-fitting size-mass relation of SFGs. We use either i-band data (i) corrected to rest-frame 5000 $\mathring{A}$ or a combination of r, i and z bands (riz) to estimate galaxy sizes at rest-frame 5000 $\mathring{A}$. Intercepts show the logarithmic sizes of galaxies with a fixed mass of $5\times10^{10}M_{\odot}$. We fit a power law to the intercepts: $R_e = A(1+z)^{\beta}$. The best-fitting parameters of this power-law (A and β) are also given. See Section 6.1.1 for details.

Quiescent Galaxies						
z	i				riz	
	Method I		Method II			
	Intercept	Slope (α)	Intercept	Slope (α)	Intercept	Slope (α)
$0.10-0.30$	$0.616^{+0.027}_{-0.012}$	$0.614^{+0.093}_{-0.055}$	$0.614^{+0.027}_{-0.014}$	$0.634^{+0.107}_{-0.055}$	$0.618^{+0.027}_{-0.014}$	$0.646^{+0.078}_{-0.04}$
$0.30-0.45$	$0.552^{+0.016}_{-0.007}$	$0.709^{+0.064}_{-0.031}$	$0.553^{+0.013}_{-0.006}$	$0.712^{+0.056}_{-0.026}$	$0.561^{+0.015}_{-0.007}$	$0.749^{+0.059}_{-0.031}$
$0.45-0.60$	$0.471^{+0.018}_{-0.009}$	$0.777^{+0.073}_{-0.036}$	$0.487^{+0.019}_{-0.009}$	$0.696^{+0.082}_{-0.039}$	$0.487^{+0.017}_{-0.008}$	$0.719^{+0.085}_{-0.042}$
$0.60-0.75$	$0.48^{+0.013}_{-0.006}$	$0.802^{+0.068}_{-0.032}$	$0.463^{+0.015}_{-0.008}$	$0.857^{+0.077}_{-0.038}$	$0.458^{+0.014}_{-0.007}$	$0.851^{+0.076}_{-0.038}$
$0.75-0.90$	$0.422^{+0.02}_{-0.01}$	$0.831^{+0.122}_{-0.056}$	$0.424^{+0.022}_{-0.011}$	$0.843^{+0.122}_{-0.061}$	$0.401^{+0.021}_{-0.011}$	$0.855^{+0.102}_{-0.052}$
A	4.81 ± 0.50		4.99 ± 0.24		5.30 ± 0.27	
β	-0.97 ± 0.23		-1.06 ± 0.11		-1.21 ± 0.11	

Table 6.2: Details of the best-fitting size-mass relation of QGs. We use either i-band data (i) corrected to rest-frame 5000 Å or a combination of r, i and z bands (riz) to estimate galaxy sizes at rest-frame 5000 Å. Intercepts show the logarithmic sizes of galaxies with a fixed mass of $5 \times 10^{10} M_{\odot}$. We fit a power law to the intercepts: $R_e = A(1+z)^{\beta}$. The best-fitting parameters of this power-law (A and β) are also given. Methods I and II differ from each other due to the pivot point estimation. See Section 6.1.2 for details.

6.1.1 Star-Forming Galaxies

We study the size-mass relation of SFGs both using corrected i-band (i) and using a combination of r, i and z bands (riz) to bracket 5000 $\mathring{A}$ (Figure 6.3 and Table 6.1), to find very similar results with both approaches. Our results on the average size evolution of SFGs (i.e., the evolution in the intercept of the size-mass relation) are consistent with the majority of previously reported findings. A slower size evolution of SFGs compared to QGs has been reported by Lilly et al. (1998), Ravindranath et al. (2004), Barden et al. (2005), van der Wel et al. (2014) and Mowla et al. (2019b). Williams et al. (2010) find a faster size evolutionary scenario ($\beta = -0.73 \pm 0.14$) for SFGs than the data used in this study ($\beta = -0.45 \pm 0.11$); the reason may be the wider redshift range that they probe ($0.5 < z < 2$). A faster evolution at $z > 1$ can influence the results by Williams et al. (2010). Moreover, the SFG size evolution shown in their Figure 4 is consistent with our data over $0.5 < z < 1$. van der Wel et al. (2014) also get slightly steeper curves with β of -0.72 ± 0.09 for SFGs against -0.45 ± 0.11 in this study. However, van der Wel et al. (2014) also cover a wider redshift range ($0 < z < 3$). A direct comparison shows that their intercepts at $z < 1$ are in agreement with our results implying that both van der Wel et al. (2014) and this study find a weaker size evolution at $z < 0.9$ (Figure 6.3). Hence, the steeper evolution published by van der Wel et al. (2014) is probably due to the faster pace of evolution observed at higher redshifts ($z > 0.9$). Finally, Lilly et al. (1998), Ravindranath et al. (2004) and Barden et al. (2005) also report either a slow or no evolution of the average size of SFGs since $z \sim 1$.

The majority of previous studies does not find any significant redshift evolution of the slopes (α) of the SFG size-mass relation. However, we find a weak evolution of SFG slopes since $z \sim 0.9$. The slope of the size-mass relation for SFGs increases linearly from 0.18 at $0.75 < z \leq 0.9$ to 0.31 at $0.1 < z \leq 0.3$. The difference between average sizes of SFGs with order of magnitude difference in stellar mass is $R_e(M_* = 10^{10.5}\mathrm{M}_\odot) - R_e(M_* = 10^{9.5}\mathrm{M}_\odot)$ = 1.78 kpc at $0.75 < z \leq 0.9$ but this difference increases by $\sim 72\%$ (3.07 kpc) at $0.1 < z \leq 0.3$. Other studies also indicate similar evolution in the slope of the size-mass relation for SFGs at $z \lesssim 2-3$ in the COSMOS field (COSMOS/UltraVISTA, Faisst et al. 2017; COSMOS-DASH, Mowla et al. 2019b). We find the best-fit linear relation for the redshift evolution of α obtained by using i-band sizes corrected to rest-frame 5000 $\AA$ (the lower panel in Figure 6.3). There is clearly a negative correlation between α and z where $\alpha = -(0.2 \pm 0.03)(1+z) + (0.55 \pm 0.05)$. We will discuss the possible cause of this evolution in the slopes of the size-mass relation for SFGs in Section 7.1.

6.1.2 Quiescent Galaxies

Figure 6.1 shows that the the size-mass relation is complex for QGs. The strength of the correlation increases with stellar mass. Some studies use a fixed galaxy mass to separate massive QGs from lower mass QGs at all redshifts (van der Wel et al. 2014; Mowla et al. 2019b). However, Mowla et al. (2019a) allow this pivot mass (M_p) to vary while fitting the size-mass relation for a sample containing both SFGs and QGs. They use a smoothly broken power law to fit the median size-mass relation demonstrating that the pivot mass changes with redshift. Therefore, we also use a smoothly broken power law,

$$R_e(M_*) = R_p \left(\frac{M_*}{M_p}\right)^{\alpha_1} \left[\frac{1}{2}\left\{1+\left(\frac{M_*}{M_p}\right)^{1/\Delta}\right\}\right]^{(\alpha_2-\alpha_1)\Delta}, \tag{6.1.5}$$

where R_p is the size at M_p, α_1 is the slope of size-mass relation at the low mass end, and α_2 is the slope at higher masses. We apply a smoothing factor (Δ) for the transition between slopes at the pivot point. As quoted by Mowla et al. (2019a), we also set $\Delta = 1/6$ to reduce the degeneracy between the slopes and the smoothing factor (we consider the random uncertainty present in the mass measurements to be ± 0.15 dex). The change of slope occurs between masses, M_1 and M_2 such that $\log M_2 - \log M_p = \log M_p - \log M_1 \sim \Delta$. We fit Equation 6.1.5 to our QG sample in five different redshift bins to obtain M_p (Method A, Figure 6.4).

We have different lower limits in stellar mass depending on the redshift of galaxies as we use mass-complete samples for characterizing the size-mass relation with increasing redshift. In the first three redshift bins, we use QGs with $M_* > 10^{9.5}$ $\mathrm{M}_\odot$ that are complete in mass and thus, we have a larger sample of low-mass galaxies ($M_* < M_p$) in these three redshift bins compared to other two bins at higher redshifts. Hence, we investigate the slopes (α_1) of the size-mass relation at lower masses ($M_* < M_p$) using the data from the nearest three redshift bins and find that α_1 is 0 within uncertainties. Hence, we fit the smoothly broken power law function on all redshift bins by fixing α_1 to be 0. Details of the

Redshift	**Method A**			**Method B**		
	log M_p	**log R_p**	α_2	**log M_p**	**log R_p**	α_2
0.10-0.30	9.95 ± 0.26	0.33 ± 0.08	0.44 ± 0.03	10.06	0.36 ± 0.04	0.46 ± 0.03
0.30-0.45	10.17 ± 0.12	0.33 ± 0.05	0.57 ± 0.02	10.16	0.33 ± 0.03	0.56 ± 0.02
0.45-0.60	10.34 ± 0.14	0.36 ± 0.06	0.58 ± 0.03	10.26	0.33 ± 0.04	0.56 ± 0.02
0.60-0.75	10.29 ± 0.14	0.33 ± 0.07	0.60 ± 0.02	10.38	0.36 ± 0.03	0.62 ± 0.02
0.75-0.90	10.50 ± 0.14	0.42 ± 0.06	0.59 ± 0.03	10.48	0.41 ± 0.03	0.58 ± 0.03

Table 6.3: Details of smoothly broken power-law fits to QGs in COSMOS data. In method A, both M_p, R_p and α_2 are free parameters but only R_p and α_2 are free parameters in Method B. We fix M_p according to the parametric evolution of the pivot points described by Equation 6.1.6 in Method B. We keep α_1 fixed to be 0 in both methods. For mass completeness, we consider QGs with $\log(M_*/M_\odot) > 9.5$ at $z < 0.6$, $\log(M_*/M_\odot) > 10$ at $0.6 < z \leq 0.75$ and $\log(M_*/M_\odot) > 10.2$ at $0.75 < z \leq 0.9$. See Section 6.1.2 for details.

power law fits are provided in Table 6.3.

From the fitting results, it is clear that the pivot points change with redshift. With exclusion of the redshift bin between 0.6 and 0.75, the pivot point evolves towards lower masses since $z \sim 0.9$. Hereafter, we refer to QGs with $M_* > M_p$ as massive QGs.

We then fit the size-mass relation of galaxies more massive than M_p using a Bayesian approach incorporating the uncertainties in stellar mass as well[4]. We do not study other QGs in this thesis due to mass incompleteness. Figure 6.3 shows the results of size-mass relation fitting of massive QGs as red diamonds and the best-fitting parameters are given in Table 6.2 (Method I). However, a relatively larger uncertainty in β (±0.23) could be caused by the failure in constraining the pivot points at higher redshifts. Hence, we investigate the

---

[4] We perform smoothly broken power-law fits only to obtain the pivot points in the size-mass relation of QGs. We do not use uncertainties in mass measurements while finding the pivot points. Since we can include the uncertainties in mass and size in the Bayesian approach, we use this method to analyse the size-mass relation of massive QGs similar to the analysis of the size-mass relation of SFGs.

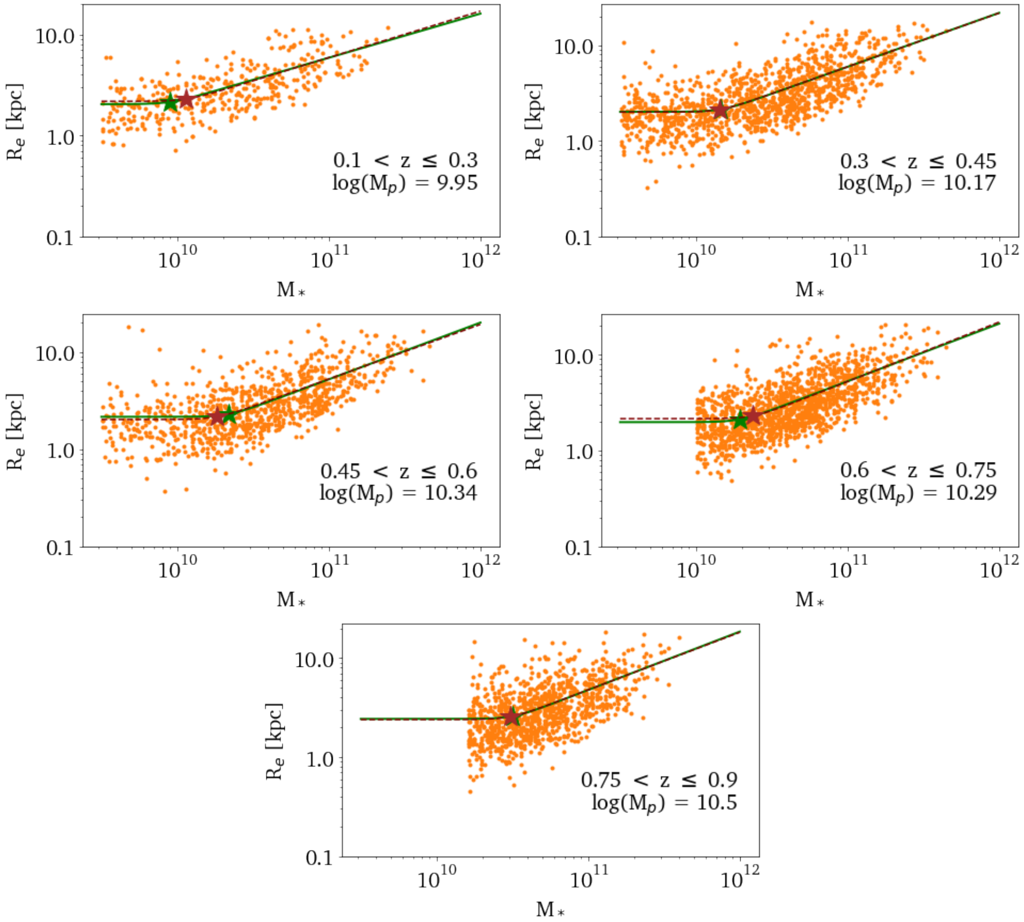

Figure 6.4: A smoothly broken power-law fit to the size-mass relation of QGs to obtain the pivot mass. The different panels show the relation in different redshift bins. The best-fitting power law model is shown as a green curve. The pivot mass obtained from the model (Method A) is indicated by a green star and its value is given in each panel. The brown dashed curves represent broken power-law fits where we fix the pivot point obtained from Equation 6.1.6 (Method B) and their pivot points are shown as brown stars. Details on the pivot points are provided in Table 6.3.

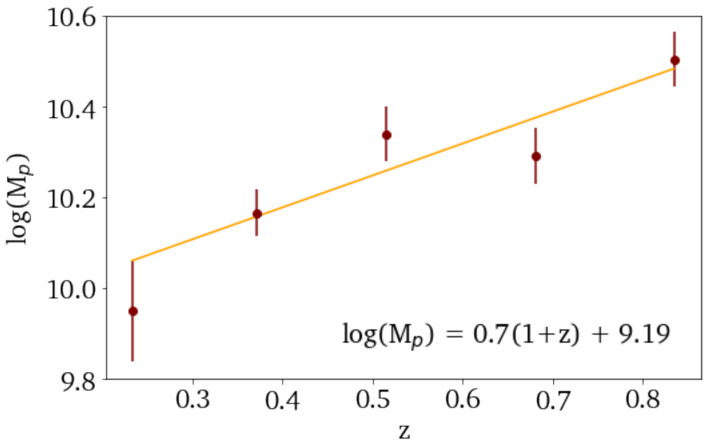

Figure 6.5: Redshift evolution of M_p for QGs. The orange line represents the best-fitting linear model.

redshift evolution of M_p. We perform a linear fit to this evolution,

$$\log M_p = (0.7 \pm 0.19)(1+z) + (9.19 \pm 0.29) \tag{6.1.6}$$

(Figure 6.5). We show the smoothly broken power-law fit performed by fixing the pivot points based on Equation 6.1.6 (Method B) as dashed lines in Figure 6.4. Details of the pivot points obtained through Methods A and B are provided in Table 6.3. The evolution of the best-fitting parameters of the size-mass relation using the pivot points obtained through Method B are also shown in Figure 6.3 as filled circles (Method II) and the corresponding power-law fit ($A(1+z)^{\beta}$) as a solid red curve in the upper panel. The power-law fit now describes the QG sizes with smaller scatter as reflected in the uncertainty of β (±0.11). Thus, we decide to use the best-fit value of M_p from the parametric evolution of the pivot points in the analysis of the size-mass relation (Method II).

We also study the size-mass relation using the combination of r, i and z bands (riz) to bracket rest-frame 5000 $\AA$ wavelength using the smoothly-evolving pivot points from the Method II. We show its results in Appendix B and the best-fitting parameters (intercept and slope) of the size-mass relation are shown as red triangles in Figure 6.3. The power-law fit to the size evolution is shown as a red dashed curve in the upper panel of the Figure. The results from the riz method agree with the i-band results discussed earlier. This agreement supports the wavelength correction we introduced to i-band size measurements to obtain the sizes of QGs at 5000 $\AA$ in the rest-frame.

The size-mass relations obtained for QGs at $0.1 < z < 0.9$ in this study generally agree with previous studies. We find a redshift evolution of the characteristic size (for $M_* = 5 \times 10^{10}$ $\mathrm{M}_\odot$) of QGs to be a power-law ($A(1+z)^\beta$) with the exponent, $\beta = -1.06 \pm 0.11$. van der Wel et al. (2014) find an evolution with $\beta = -1.24 \pm 0.08$ since $z \sim 3$, Williams et al. (2010) find $\beta = -0.96 \pm 0.13$ since $z \sim 2$ and Morishita et al. (2014) report $\beta = 1.06 \pm 0.19$ for QGs at $0.5 < z < 3$. Mowla et al. (2019b) also find a similar evolution since $z \sim 3$ while studying QGs in different mass bins ($\beta \approx 0.8 - 1.3$).

Additionally, in agreement with the literature, the slopes of the size-mass relation are steeper for massive QGs ($M_* > M_p$) in five redshift bins covering $0.1 < z \leq 0.9$ redshift interval than for SFGs and low mass QGs in the same redshift bins. The slopes found in this study are comparatively higher than many of the published results in the literature. For example, Mowla et al. (2019b), Newman et al. (2012) and Faisst et al. (2017) report slopes of 0.58 ± 0.04, 0.59 ± 0.07 and 0.55 ± 0.05 respectively for QGs at $0.5 < z < 1$, whereas the slopes of the size-mass relation for QGs found in this study at the same redshift range is 0.7-0.9. However, van der Wel et al. (2014) find an average slope of 0.75 at $z < 3$. We suspect the difference in slopes in some studies is due to differences in the methodologies used in various studies (e.g., Newman et al. (2012) use $R_e(1+q)/2$ for the size measurements, and van der Wel et al. (2014) take into account contimation between the SFGs and QGs, which is not done by Mowla et al. (2019b)).

We find a weak evolution in the slope of the size-mass relation for QGs at $0.1 < z < 0.9$ (Figure 6.3); the slope becomes shallower with time. We fit a linear relation between the slope and redshift: $\alpha = (0.39 \pm 0.11)(1+z) + (0.17 \pm 0.17)$ (Figure 6.3). Although some other studies find similarly weak evolution of the slope for the QG size-mass relation (Mowla et al. 2019b), the majority of the studies shows no evolution (e.g., van der Wel et al. 2014; Newman et al. 2012). Possible reasons for the lack of evolution in the slopes are the wider redshift coverage of the analysis and relatively smaller sample size at $z < 1$. The earlier studies on the size-mass relation of QGs generally do not probe the slope evolution by splitting the QG sample into several redshift bins at $z < 1$.

6.2 Sérsic Index

Since the Sérsic index (n) tells us how centrally concentrated a galaxy light profile is, its change with redshift indicates the evolution in the galaxy morphology. A lower value of

n indicates a disky or disk-dominated galaxy while a higher value suggests an elliptical or bulge dominated galaxy. However, it is important to note that we use a single Sérsic profile to describe galaxy light profiles. Since most galaxies have both disk and bulge components, n obtained from a single Sérsic profile fitting describes the overall concentration of galaxy light profiles including contributions from disks and bulges. We cannot study the contributions from various components (e.g., bulges) to the overall galaxy light profiles through a single Sérsic profile fitting alone. Moreover, the Sérsic index is less robust compared to size measurements (Section 5.2). The measurement of n is influenced heavily by various factors such as the size of the galaxy, the depth of the survey, proximity to other bright objects in the sky, etc. Nevertheless, values of n measured in this study using a single profile study may be still useful to study the overall morphological evolution of galaxies.

Figure 6.6 shows the median n of both SFGs and QGs in eight equally populated mass bins at five redshift bins. As expected, QGs have a higher median value of n compared to SFGs in any given mass bin at any redshift since $z \sim 0.9$. There is a clear segregation between SFGs and QGs in $\log n - \log M_*$ space. Sérsic indices of both SFGs and QGs show a mass dependence but this dependence is more prominent for massive SFGs ($> 10^{10} M_\odot$) compared to SFGs at lower masses ($< 10^{10} M_\odot$). Figure 6.7 shows how n is related to galaxy sizes. SFG morphology shows a negative correlation between n and R_e but the correlation is positive for QGs. A negative correlation for SFGs indicates that the bulges become more dominant in SFGs with smaller sizes than SFGs with larger sizes. Since bulges are more

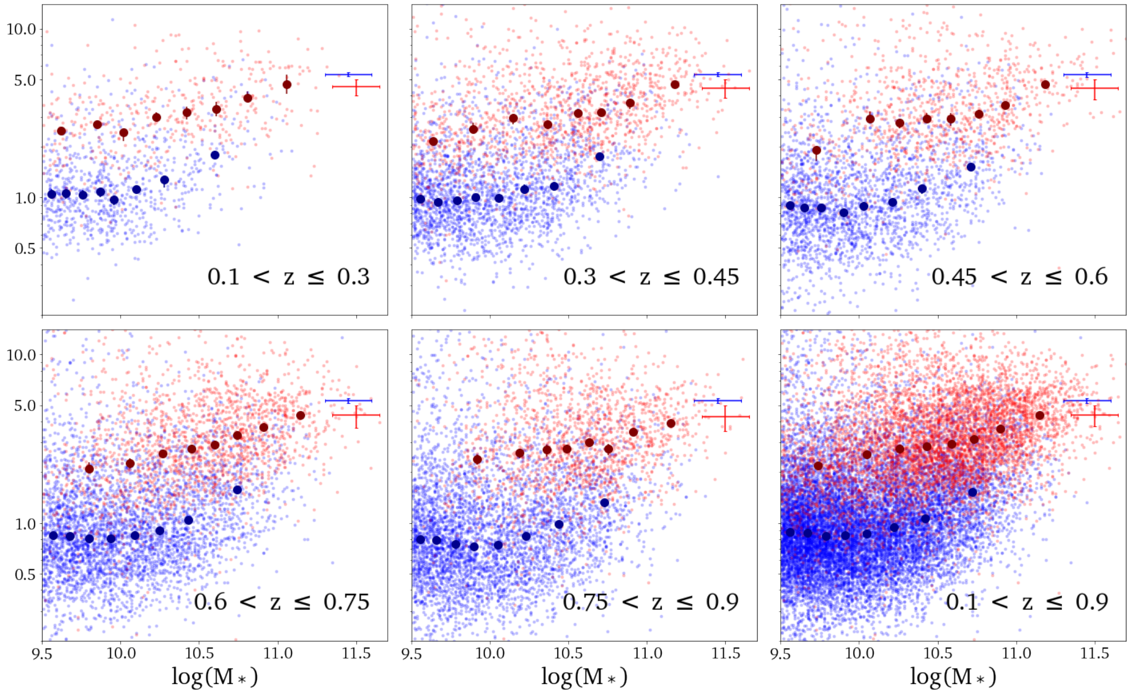

Figure 6.6: Relation between Sérsic index and stellar mass of galaxies. Sérsic indexes are used from r, i and z images depending on their redshifts in order to bracket rest-frame 5000 $\AA$. The first five panels are for galaxies in five different redshift bins whereas the last panel shows the relation for the whole sample. SFGs are shown in blue and QGs in red and the median uncertainties present in the measurements of mass and n are shown as error bars in the top right corner of each panel. Median Sérsic indices in different mass bins are denoted by larger data points with corresponding error bars from bootstrapping.

centrally concentrated, their dominance yields smaller sizes compared to disk-dominated galaxies. QGs, which are largely elliptical galaxies with higher n in our sample, show a positive relation with R_e; their profiles become more centrally concentrated (higher n) as they grow in size. A galaxy with higher n will have larger wings and hence, has larger size compared to a galaxy with lower n (Figure 4.1).

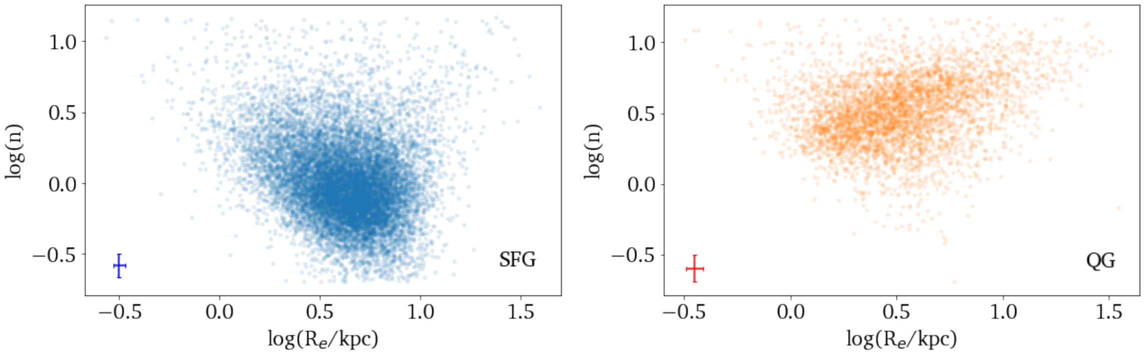

Figure 6.7: Sérsic indices of SFGs (left) and QGs (right) plotted against their sizes. Median uncertainties present in the measurement of n and R_e are shown as error bars in each panel.

6.3 Environment

Environment plays an important role in the evolution of galaxies (Section 1.2.3). In the local Universe, QGs are generally found in denser environments and SFGs in low density regions (e.g., Peng et al. 2010b). Several studies show that the environmental effects on the star-formation activity of galaxy population are similar to those in the local Universe till $z \sim 2$ (Guo et al. 2017; Chartab et al. 2020). Moreover, denser environments aid in galaxy interactions such as mergers, accretion and tidal stripping (e.g., Hausman & Ostriker 1978; Farouki & Shapiro 1981; Aguilar & White 1986; Ferguson & Binggeli 1994; Oser et al. 2010, 2012). Environment can also affect quenching mechanisms which will also contribute towards the size evolution of the galaxy population through progenitor effects (e.g., Gunn & Gott 1972; Balogh et al. 2000; Mayer et al. 2006; Peng et al. 2015; D'Onofrio et al. 2015).

There is no consensus in the literature on how environment affects the sizes of galaxies since $z \sim 2$. While studies such as Cooper et al. (2012), Lani et al. (2013), Delaye et al. (2014) and Andreon (2018) report that galaxies in clusters are larger in size than their counterparts in the field at $0 \leq z \leq 2$, Valentinuzzi et al. (2010b,a) find that cluster galaxies are smaller than those in the field in a similar redshift range. Several other studies do not find any significant difference between cluster and field galaxies (Rettura et al. 2010; Newman et al. 2014; Sweet et al. 2017) at $1 < z < 2$.

6.3.1 COSMOS Clusters

We study the morphology of the rich cluster members (Section 3.1.3) to investigate the effects of environment on the galaxy size-mass relation. We have size measurements for 75 QGs from 7 clusters: 65 are at $z < 0.4$ and the rest are at $z \sim 0.73$. We plot the size-mass relation of these galaxies in the i-band corrected to rest-frame 5000 $\AA$ in Figure 6.8 and provide the details of the best-fitting parameters in Table 6.4. We find that the slopes of the size-mass relation in log-log space for cluster galaxies are similar to those of the parent CLAUDS+HSC-SSP COSMOS QG population (Section 6.1). Moreover, the intercepts of the size-mass relation of the cluster members also correspond to those of the parent QG sample in their respective redshift bins. The sizes of galaxies in the clusters are similar to their parent COSMOS QG population. This non-difference in galaxy sizes between cluster environment and the parent COSMOS population agrees with results by earlier studies probing higher redshifts ($1 < z < 2$, Rettura et al. 2010; Newman et al. 2014; Sweet et al.

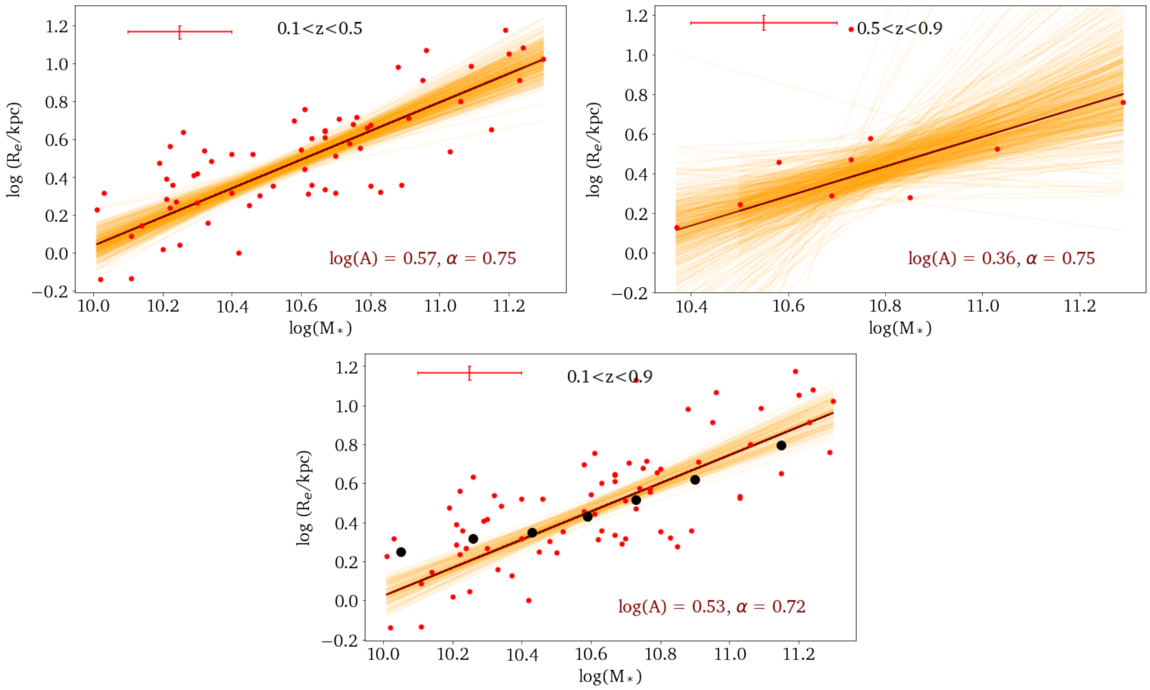

Figure 6.8: Linear fits to the size-mass relations of galaxies from COSMOS clusters in rest-frame 5000$\AA$ by applying the wavelength correction to the *i*-band data. The upper panels show the relation in two different redshift bins while the lower panel combines them both. The black filled circles in the lower panel show the median sizes of the parent COSMOS QG population. Other details are the same as for Figure 6.2.

2017), although several other studies find a dependence on environment in galaxy size distributions since $z \sim 2$ (e.g., Valentinuzzi et al. 2010b; Cooper et al. 2012; Lani et al. 2013).

6.3.2 HST-CLASH Clusters

The cores of HST CLASH clusters enable us to investigate extremely dense environments. Our cluster core data covers a region within $R/R_{200} \sim 0.4$ from the BCG in each cluster. Unlike for the COSMOS data, we do not separate the CLASH cluster galaxy population into SFGs and QGs. We do this because, due to our sample selection methods (spectroscopic

Sample	Redshift	Intercept	Slope
COSMOS	0.1-0.5	$0.566^{+0.028}_{-0.027}$	$0.755^{+0.094}_{-0.088}$
	0.5-0.9	$0.359^{+0.068}_{-0.066}$	$0.746^{+0.356}_{-0.265}$
	0.1-0.9	$0.535^{+0.026}_{-0.026}$	$0.721^{+0.083}_{-0.097}$
CLASH	0.18-0.29	$0.395^{+0.031}_{-0.023}$	$0.325^{+0.132}_{-0.148}$

Table 6.4: Details of best-fitting size-mass relation of galaxies in COSMOS clusters and HST-CLASH clusters. For COSMOS clusters, we use *i*-band data corrected for rest-frame 5000 $\AA$ to the estimate sizes used in the relation. Intercepts show the logarithmic sizes of galaxies with a fixed mass of $5 \times 10^{10} M_{\odot}$.

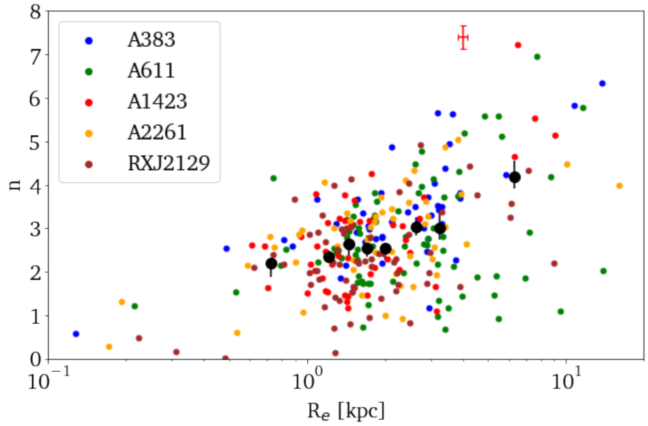

Figure 6.9: Sérsic indices of HST CLASH cluster members plotted against their sizes. Median uncertainties present in the measurement of n and R_e are shown as error bars.

and the red-sequence methods together, Section 3.2), the majority of the cluster members being studied here are expected to be QGs. Figure 6.9 shows how n is correlated with size. There is a positive correlation between n and R_e similar to QGs in COSMOS (Figure 6.7).

Assuming that the density of the environment decreases with distance from the BCG[5], we analyse Sérsic parameters of galaxies (R_e, n and q) against their projected distance

---

[5] We assume that BCGs are at the centres of the five HST CLASH clusters as they are relaxed systems.

from the centres of the clusters (Figure 6.10). Median sizes of galaxies do not vary with their position in the cluster cores. However, we find that all galaxies closer to the BCG ($R/R_{200} < 0.1$) are smaller than 5 kpc. In contrast, $11 \pm 4\%$ of the galaxies at distances $R/R_{200} > 0.1$ have larger sizes ($R_e > 5$ kpc). To check the significance of the absence of larger galaxies close to the cluster centre, we draw (with replacement) 10000 sub-samples from galaxies at $R/R_{200} > 0.1$ with size equal to the sample size at $R/R_{200} < 0.1$. Among these simulated sub-samples, the absence of large galaxies ($R_e > 5$ kpc) are found only in $\sim 0.5\%$ of the sub-samples thereby indicating that the absence of large galaxies towards cluster centre is significant.

Similarly, we do not find any significant difference in median Sérsic indices with the projected distance from the cluster centre (middle panel in Figure 6.10). However, at closer distances from the BCG, almost all galaxies have $n > 2$ ($87 \pm 4\%$). Thus, galaxies closer to BCG are generally ellipticals or bulge dominated. At farther distances from the centre of the clusters ($R/R_{200} > 0.2$), the percentage of galaxies with $n > 2$ decreases ($67 \pm 4\%$) and there are several disky galaxies with $n < 1.5$ ($18 \pm 3\%$) at these distances. We also analyse the axis ratio (q) of galaxies (lower panel in Figure 6.10). We find that median value of q does not vary significantly with projected distance from the cluster centre although galaxies in the cluster cores are more spherically symmetric than elongated.

We investigate the age of galaxies for which we have spectroscopic data using an age indicator, D_n4000. The D_n4000 index is a ratio of the flux in two spectral windows above

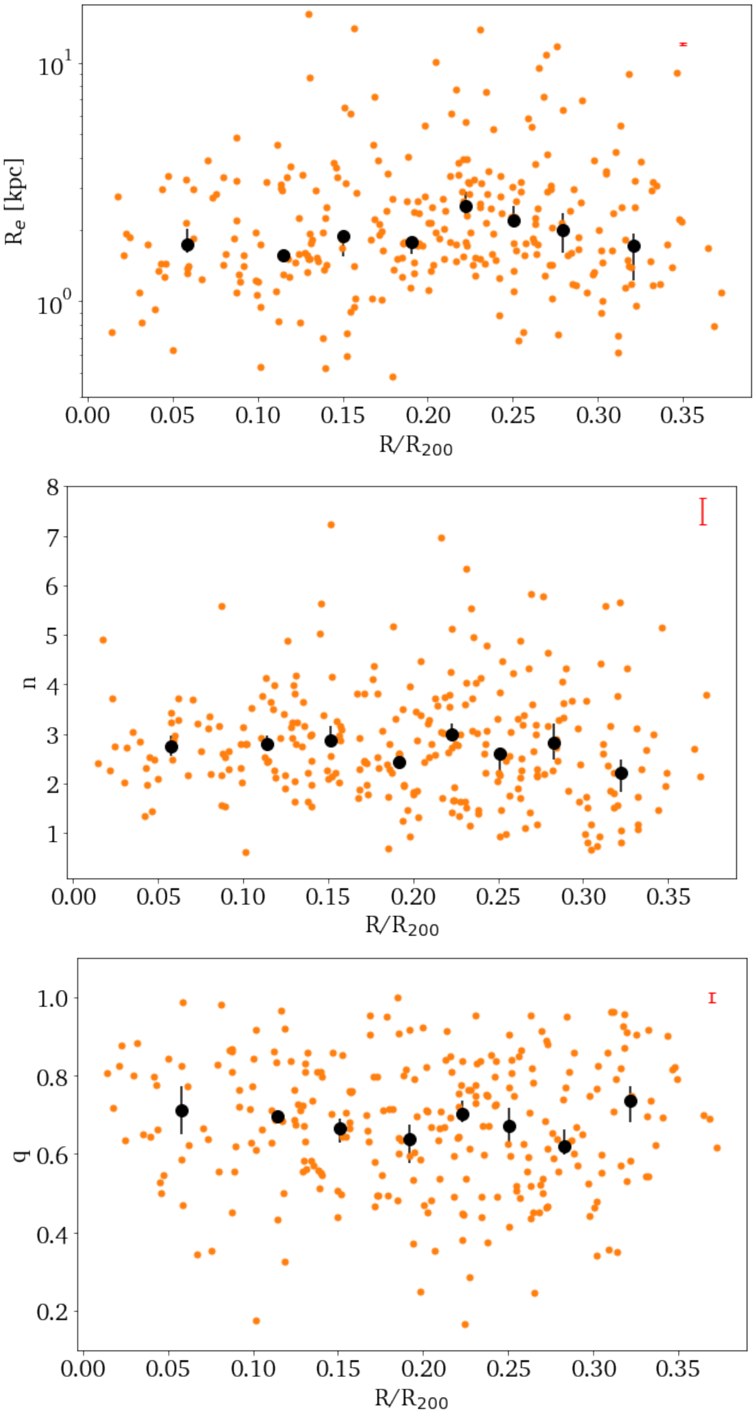

Figure 6.10: Sérsic parameters, size (upper), Sérsic index (middle) and axis ratio (lower), plotted against projected radial distance of galaxies from the BCG. Radial distances are normalised by their cluster virial radii. Median uncertainty present in the measurement of Sérsic parameters is shown as a red error bar in the top right corner of each panel. The black data points represent the median values of the parameters in eight equally populated radial distance bins ad the error bars on the median are obtained through bootstrapping.

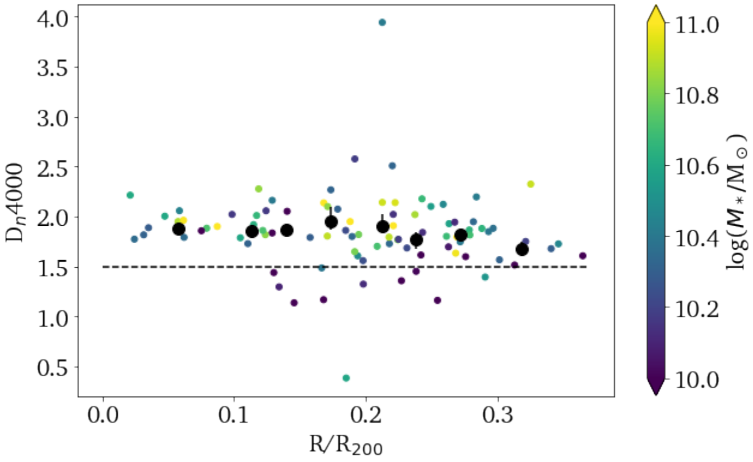

Figure 6.11: Galaxy age proxy, D_n4000 index is plotted against projected radial distance of galaxies from BCG. Radial distances are normalised by their cluster virial radii. Colours indicate the stellar mass of galaxies. Black data points represent the median values of the parameters in eight equally populated radial distance bins. Error bars are obtained through bootstrapping. Black dashed line separates younger galaxies from the older population. Any galaxy that lies below this line is considered young.

and below the 4000 $\AA$ break in galaxy spectra (Balogh et al. 1999; Zahid et al. 2018). The index is generally used as a proxy for the age of galaxies because it increases with the age of the stellar population[6] (Kauffmann et al. 2003; Zahid et al. 2015). We consider galaxies with $D_n4000 > 1.5$ as old and the rest as young (Li et al. 2006). An SFG will have the D_n4000 index well below 1.5 because its D_n4000 does not change significantly with time. However, once the star formation in a galaxy is quenched, the D_n4000 index changes rapidly with time (increases beyond 1.5), and this change is stronger for galaxies with higher metallicities (Zahid et al. 2019). Figure 6.11 shows the age of the galaxies as a function of the distance from the cluster centre. Galaxies at the cluster core are generally

---

[6] The 4000 $\AA$ break is produced by the flux absorption at $\lambda < 4000\AA$ by the metals present in the atmospheres of old stars (age $\gtrsim 10^8$ years). In QGs, this break becomes prominent due to the lack of flux from young massive stars.

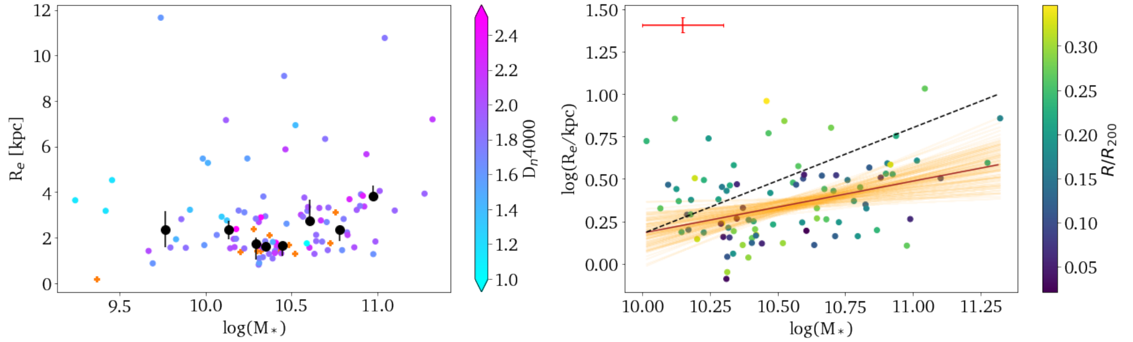

Figure 6.12: Size-mass relation of HST CLASH cluster galaxies. Black points in the left panel show the median sizes in eight equally populated mass bins along with their bootstrapped error bars. Colours of the data points in the left panel indicate their age (D_n4000). Galaxies with no measured age are shown as orange crosses. The right panel shows the best-fitting linear relation for galaxies more massive than $10^{10} M_\odot$. Colours indicate their projected distance from the cluster centres. The black dashed line shows the size-mass relation for massive QGs from COSMOS at $0.1 < z \leq 0.3$. The red error bar in the top left corner denotes the median uncertainties present in the size and mass estimation. Other details are the same as in Figure 6.2.

older galaxies and the median age does not change with distance. We notice the absence of a younger population near the cluster centre ($R/R_{200} < 0.1$). Younger galaxies generally have lower masses ($\log(M_*/\mathrm{M}_\odot \lesssim 10.2$) and are mainly found at larger distances ($R/R_{200} > 0.1$) from the cluster centre.

We study the size-mass relation of HST CLASH cluster core galaxies (Figure 6.12). We find that the median sizes of galaxies in the cluster cores do not show any strong correlation with stellar mass (the left panel). This is further illustrated in the right panel where we fit a linear relation to the galaxies more massive than 10^{10} M$_\odot$ (83 galaxies). Details of the best-fitting parameters are provided in Table 6.4. The best fitting parameters show a relatively weaker relation in the cluster cores with a slope of ~ 0.33, which is similar to

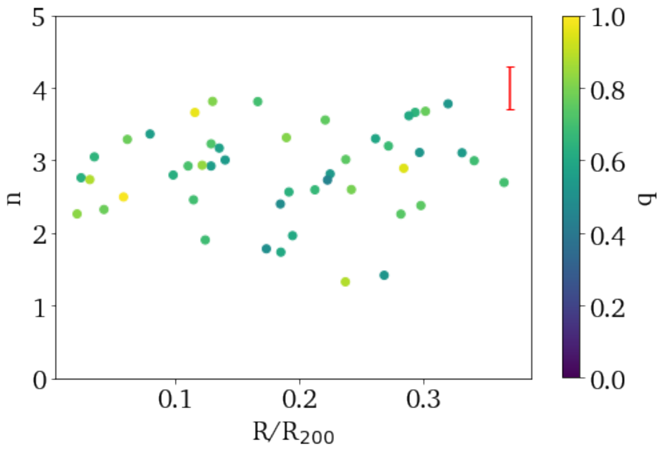

Figure 6.13: Sérsic indices of massive compact galaxies ($M_* > 3 \times 10^{10}$ and $R_e < 2$ kpc) versus projected radial distance of galaxies from BCGs in CLASH clusters. The data points are colour coded with their axes ratio. The median uncertainty present in the measurement of n is shown as a red error bar in the top right corner.

SFGs in CLAUDS+HSC-SSP COSMOS (Section 6.1) although galaxies in the CLASH cluster cores are generally old. There are young extended galaxies in the CLASH sample at lower masses but the sizes of the galaxies in the cluster cores are generally smaller than those of the parent QG population and cluster QGs in the CLAUDS+HSC-SSP data at a given stellar mass (the right panel of Figure 6.12). Damjanov et al. (2015) also report that the QGs in the cluster environment are more compact than their parent sample in the COSMOS field. We also find that $\sim 35\%$ of galaxies in the CLASH cluster cores are compact ($R_e < 2$ kpc) but massive ($M_* > 3 \times 10^{10}$). These massive compact galaxies are generally bulge dominated or ellipticals with high axis ratios ($q \gtrsim 0.5$) and are found at all distances from the the centres of the clusters (Figure 6.13).

Chapter 7

Discussion

7.1 Evolution of Star-Forming Galaxies

We have shown that the evolution in the average sizes of SFGs at a fixed mass (5×10^{10} $\mathrm{M}_{\odot}$) found in this study is weaker ($\beta = -0.45 \pm 0.11$) than the evolution reported in some of the previous studies, e.g., $\beta = -0.72 \pm 0.09$ (van der Wel et al. 2014) and $\beta = -0.73 \pm 0.14$ (Williams et al. 2010). These earlier studies measure the sizes of SFGs over a large redshift baseline ($z \lesssim 3$) and their size measurements may be biased by the faster evolution at $z > 1$.

The evolution of dark matter halos (in which galaxies reside) may be related to the change in the rate of size growth of SFGs. Numerical simulations show that in the hierarchical paradigm of structure formation, there is a trend in concentration (c) of dark matter halos at fixed mass with redshift, $c \sim (1+z)^{-1}$, where larger values of c denotes more concentrated dark matter halos (Bullock et al. 2001; Somerville et al. 2008, 2018). The halo concentration can affect disk sizes as higher halo concentration will produce smaller and denser disks. At the same time, the lower mass and weaker gravitational forces in the central parts of the dark matter halo due to a low halo concentration results in extended disks. This halo concentration effect may result in the formation of proportionally larger galaxy disks at higher redshifts ($z \sim 1$) compared to the local Universe ($z \sim 0$). However, once the disks are formed, they grow in size with time as they gradually accrete mass. These competing effects - formation of larger disks at higher redshifts compared to lower redshifts and growth of disks with time - weaken the size evolution in SFGs.

van der Wel et al. (2014) have investigated another reason for the decreasing rate of SFG size growth with cosmic time since $z \sim 3$ using observational data from the CANDELS survey. Their work indicates that the increase in the number of red SFGs (rest-frame $U - V > 1$) since $z \sim 2$ contributes to the slowing down of the SFG size evolution compared to rapid evolution ($\beta \sim -1.1$) reported at $z \gtrsim 2$ (e.g., Oesch et al. 2010; Mosleh et al. 2012) because red SFGs are smaller in size than bluer SFGs. We also investigate the effect of the change in fraction of red galaxies on the evolution of the sizes of SFGs in our data (Figure 7.1). We divide our SFG population into two groups, red ($U - V > 1$ in rest-frame) and blue ($U - V \leq 1$ in rest-frame), and define the SFG red fraction as

$$\text{SFG red fraction} = \frac{\text{Number of red SFGs}}{\text{Total number of SFGs}}. \tag{7.1.1}$$

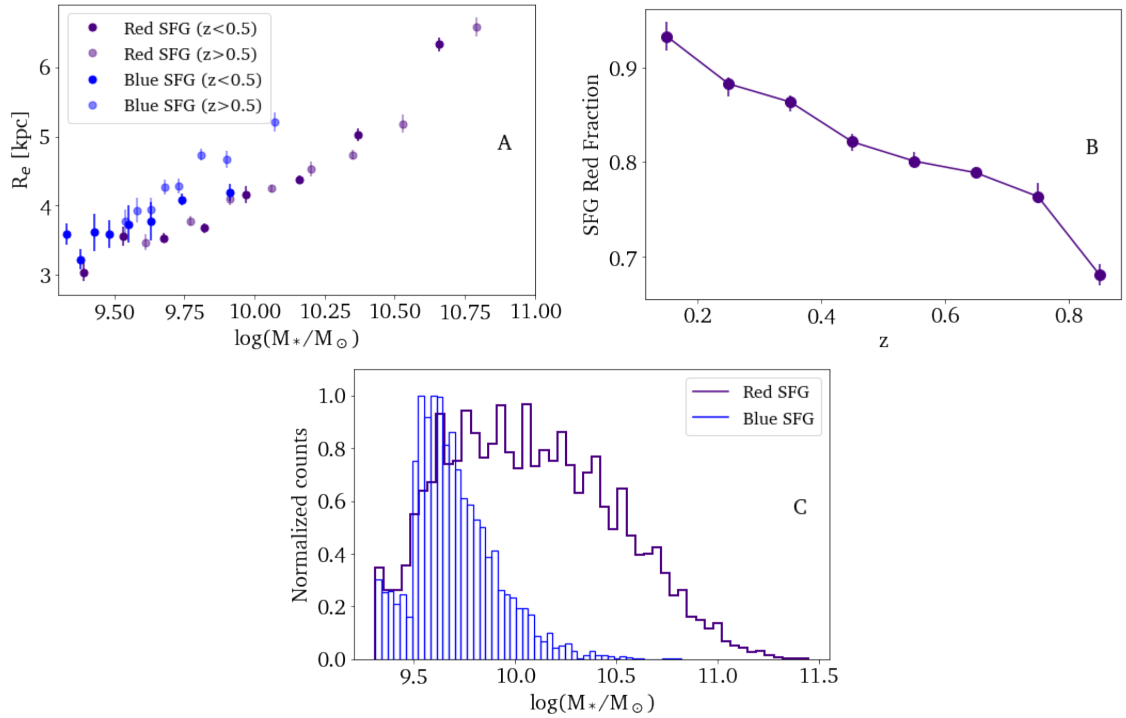

Figure 7.1: Panel A: Average size of red and blue SFGs vs galaxy stellar mass. The blue colour is for blue SFGs and the purple for red SFGs. The semi-transparent data points in each colour represent galaxies at $z > 0.5$ and the solid ones are for galaxies at $z < 0.5$. The error bars are obtained through bootstrapping. Panel B: Redshift evolution of the SFG red fraction. Bootstrapped error bars are also shown, although the error bars are smaller than the data points in some of the redshift bins. Panel C: Mass distribution of red and blue SFGs at $0.1 < z < 0.9$. See Section 6.1.1 for details.

We find that at a given mass and a redshift the red SFGs are smaller than their bluer counterparts of the same mass (Panel A in Figure 7.1). Moreover, the SFG fraction has increased steadily since $z \sim 0.9$ (Panel B in Figure 7.1). Hence, we provide new evidence for the argument that the increasing fraction of red SFGs contributes to the decrease in size growth of the SFG population at $z < 0.9$.

The increase in the SFG red fraction with time is also consistent with the observed evolution in the slopes of the size-mass relation for SFGs (Figure 6.3). Blue SFGs have larger sizes but their mass distribution is concentrated at lower masses than the red SFGs (Panel C in Figure 7.1). At higher redshifts ($z > 0.5$), the higher abundance of blue SFGs ($\sim 25\%$, Panel B in Figure 7.1) increases the average sizes of SFGs in the lower mass bins ($\log(M_*/M_\odot) < 10$) but the average sizes of SFGs are unaffected at higher masses. Consequently, the slope of the size-mass relation is flattened. In contrast, the slopes are steeper at lower redshifts ($z < 0.5$) due to the decrease in fraction of blue SFGs ($< 15\%$) with time (Panel B in Figure 7.1).

The increase in SFG red fraction is connected to the morphological transformation of SFGs as they age. Previous studies indicate that one of the major factors affecting the morphological evolution of SFGs since $z \sim 0.9$ is the *growth of bulges* at the centres of a galaxies (e.g., Oser et al. 2010; Hopkins et al. 2010; Tacchella et al. 2015; Sachdeva et al. 2017). Bulges are more centrally concentrated and their dominance will result in smaller R_e of the single Sérsic profile that describes the overall light profile of SFGs. Our results also show that the red SFGs have median sizes smaller than their bluer counterparts (Panel A in Figure 7.1).

Although dust can redden SFGs by absorbing starlight at shorter wavelengths (ultraviolet band) and re-emitting at longer wavelengths (infrared band, Xiao et al. 2012), we find that the increasing fraction of red SFGs also supports the bulge growth scenario by analysing the distributions of n in the Sérsic profiles of red and blue SFGs (Figure 7.2).

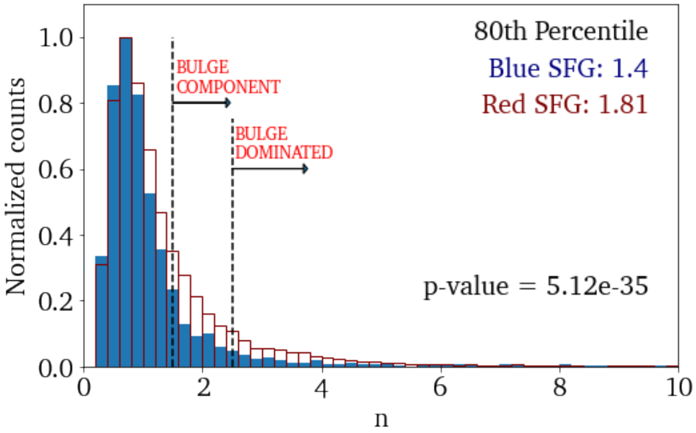

Figure 7.2: Distribution of Sérsic indices of red ($U-V>1$ in rest-frame) and blue ($U-V<1$ in rest-frame) SFGs. The red colour represents the red SFG population and blue is for blue SFGs. Histograms are normalised such that the count of the most populated bin is 1. The 80^{th} percentile of n for each distribution is given in the figure. We also show the p-value from the K-S test on the distributions.

Because bulges typically have higher Sérsic index than disks, bulge growth should result in an increase in the measured n of single Sérsic profiles for SFGs. Based on observational studies, galaxies with $n \gtrsim 1.5$ are generally considered as having a significant bulge component and those with $n \gtrsim 2.5$ are considered bulge dominated or spheroidal galaxies (e.g., Dutton 2009; Sachdeva 2013). The distributions of n for red and blue SFGs show that $\sim 28\%$ of red SFGs have $n > 1.5$ but only $\sim 17\%$ of blue SFGs fall in this category (Figure 7.2). Similarly, the distribution of n in red SFGs shows a tail at higher n: the 80^{th} percentile is at $n = 1.81$ in red SFGs compared to $n = 1.4$ in blue SFGs. This higher value of n for red SFGs (tail of n distribution) indicates the presence of bulges in them. We also perform a Kolmogorov–Smirnov test (K-S test, Kolmogorov 1933; Smirnov 1948) to check

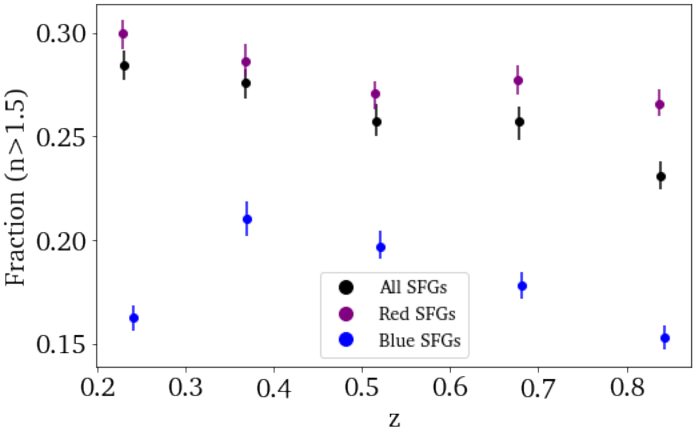

Figure 7.3: Fraction of SFGs with the significant bulge component ($n > 1.5$) in five redshift bins. Black represents all SFGs, purple is for red SFGs ($U - V > 1$) and blue is for blue SFGs ($U - V < 1$). Error bars are obtained through bootstrapping.

whether the two distributions differ statistically from each other[1]. An extremely small p-value (5.1×10^{-32}) implies that the distribution of Sérsic indices for red SFGs is different from that for blue SFGs. Thus, the increasing SFG red fraction with time is consistent with bulge growth in SFGs.

Additionally, we investigate the growth of bulges in SFGs by analysing the fraction of galaxies with a significant bulge component in their profile ($n > 1.5$) in five redshift bins (Figure 7.3). We find that the percentage of galaxies with a significant bulge component ($n > 1.5$) increases in the SFG population with time. We also find that this growth of bulges is reflected in both red and blue SFGs except in the lowest redshift bin ($0.1 < z \leq 0.3$). The observed low fraction of blue SFGs with bulge component (~ 0.16) in the lowest redshift

---

[1] K-S test investigates the null hypothesis that the two distributions are drawn from the same underlying parent distribution. If the p-value is less than 0.05, we can reject the null hypothesis, i.e., the two distributions are statistically different.

bin compared to higher redshifts ($0.3 < z \leq 0.75$) is probably due to the low survey volume probed at $z < 0.3$. Thus, our results support an ongoing bulge growth in SFGs at least since $z \sim 0.9$.

Several physical processes may be responsible for the emergence and growth of bulges in galaxies. Bulge growth can happen internally (secular evolution) or can be induced externally. In secular evolution, the bulge formation and growth is often a result of perturbations in the galaxy disks due to internal structural properties such as spiral arms and bars (Kormendy & Kennicutt 2004; Athanassoula 2005; Kormendy 2008; Gadotti 2009; Sellwood 2014). Although such secular growth of bulges (also called pseudo-bulges) is global to all disk galaxies, pseudo-bulges are characterised by disk like profiles ($n \sim 1$). In contrast, bulge formation and growth induced externally through mergers by displacing the stars and the gas in the disks towards galaxy centres can contribute to the increase in the Sérsic index (Naab et al. 2006; Gadotti 2009; Hopkins et al. 2010; Oser et al. 2010). Bulges formed in this manner, also called classical bulges, have light profiles and properties similar to elliptical galaxies. They generally have centrally concentrated surface brightness distributions, which are reflected in their higher n. Thus, the growth of classical bulges can be responsible for the increasing higher n tail of the Sérsic index distribution of SFGs with time since $z \sim 0.9$ in our sample (Figures 7.2 and 7.3).

One possible approach to consider in future studies of bulge growth in SFGs is the analysis of their bulge-to-total (B/T) ratios. An increasing B/T ratio in SFG profiles with cosmic time will indicate bulge growth. We could address this in our future research by incorporating disk-bulge decomposition using multi-component profile fitting. Furthermore, a comparative study of SFG morphology in different bands can also help study bulge growth because bulges are redder in colour compared to disks due to inside-out quenching of galaxies (Tacchella et al. 2015). Since we can analyse galaxies in U, g, r, i, z and y bands, we could also compare the light distributions of SFGs in these six bands in our future work.

7.2 Evolution of Quiescent Galaxies

The median size of QGs at a given mass is two times smaller than the size of SFGs at $0.1 < z < 0.9$ (the median size of QGs with masses $10.3 < \log(M_*/M_\odot) < 10.5$ is 2.21 kpc but the median size of the SFGs of the same mass range is 4.95 kpc, Figure 6.1). According to Lilly & Carollo (2016), this difference in galaxy sizes can be explained by two processes: progenitor bias and the fading of disks (Section 1.1). However, progenitor bias and the fading of disks alone cannot describe the observed details in our data. If these were the only factors, then the observed size evolution of QGs would be slower than that of the SFGs (Lilly & Carollo 2016). On the contrary, our analysis shows that QGs grow in size faster than SFGs (the upper panel in Figure 6.3), in agreement with most of the previous studies (eg., van der Wel et al. 2014; Mowla et al. 2019b; Damjanov et al. 2019). Thus, there must be additional factors that affect the observed size evolution of QGs.

Galaxy mergers can contribute significantly towards the size evolution of galaxies (Section 1.1). Although major dry mergers can yield an increase in size of QGs proportional to the increase in mass (eg., Boylan-Kolchin et al. 2006; Naab et al. 2007), their relative number since $z \lesssim 1$ is low (e.g., Bundy et al. 2009; López-Sanjuan et al. 2010a,b; Kaviraj et al. 2014; Thibert 2018). However, several studies show that minor mergers and accretion can support size growth in QGs (e.g., Khochfar & Silk 2006; Bezanson et al. 2009; Naab et al. 2009; van Dokkum et al. 2010; Trujillo et al. 2011; Oser et al. 2010, 2012; Hilz et al. 2012; Fagioli et al. 2016; Zahid et al. 2019). Moreover, both observational studies (Bezanson et al. 2009; Zahid et al. 2019) and simulations (Naab et al. 2009) indicate that minor mergers can cause a size growth proportional to the square of the mass added because the material is added to the galaxy outskirts.

We can investigate galaxy growth via minor mergers and accretion by testing the predictions by theoretical and/or empirical models. Since minor mergers and accretion generally preserve the virial equilibrium of the host galaxy, it is possible to predict the morphological transformation caused by these processes by tracing mass growth in galaxies (Bertin et al. 2002). Zahid et al. (2019) provide such predictions in the evolution of QG morphology based on the Sloan Digital Sky Survey (SDSS) Main Galaxy Sample (Strauss et al. 2002) at $z \sim 0$ and the F2 field of the Smithsonian Hectospec Lensing Survey (SHELS, Geller et al. 2014) at $z < 0.6$. Based on the differences between the SDSS local QG sample and the SHELS QG sample at higher redshifts, Zahid et al. (2019) develop an empirical model to describe the observed growth of mass, size and stellar velocity dispersion, which are functions of observed galaxy age and redshift, simultaneously. By matching the evolved SHELS galaxy properties and the observed SDSS galaxy properties, they parametrize the growth efficiency for mass and the growth rate for galaxy size and velocity dispersion due to increase in galaxy stellar mass. Zahid et al. (2019) also find that the growth parameters obtained from their empirical model match well with the purely theoretical and independent model predictions for minor mergers. Using the known correlation between stellar mass and dynamical mass together with virial theorem, Zahid et al. (2019) make predictions for the evolution of the Sérsic index as a function of stellar mass and redshift. This estimated evolution in Sérsic index (n) is a consequence of the observed mass growth and known correlation between n and stellar mass (Zahid & Geller 2017).

In Figure 7.4, we compare these predictions of Zahid et al. (2019, coloured curves) with the Sérsic indices of QGs measured in this study at $z \leq 0.5$ (maroon data points). We avoid QGs at higher redshifts because the model by Zahid et al. (2019) is constrained by the observed evolution of galaxy properties since $z \sim 0.6$. We also show the observed Sérsic index - stellar mass relation for SDSS QGs as a black curve in Figure 7.4. The Sérsic indices of QGs measured in this study are systematically smaller than the indices measured in SDSS QGs, in line with the predictions. Nevertheless, our measurements do not match the predictions perfectly. Our QG sample from COSMOS has a median redshift of 0.375 but the measured n in our sample is higher than the predicted n at $z = 0.35$, and in some mass bins, higher than $z = 0.25$ predictions. Therefore, we infer that minor mergers alone cannot

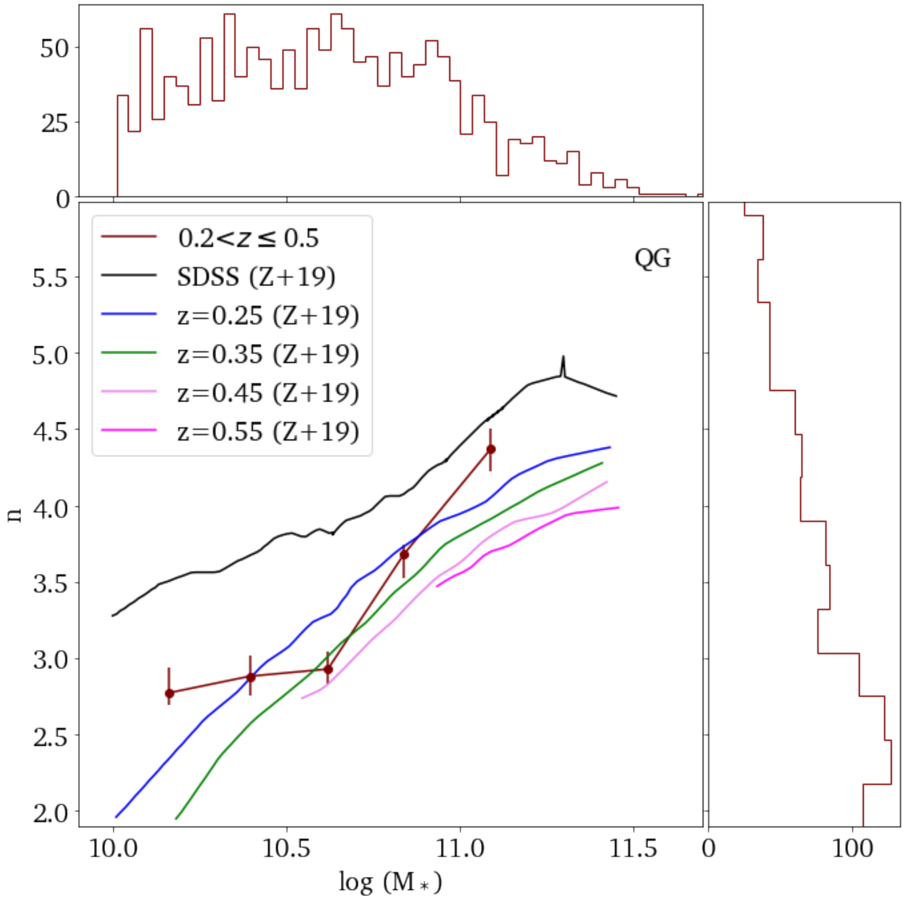

Figure 7.4: Relation between Sérsic index and stellar mass of QGs at $0.1 < z \leq 0.5$. Maroon data points represent median values of n in five equally populated mass bins. Error bars are obtained through bootstrapping. Sérsic indices are used from r, i and z images depending on their redshifts in order to bracket rest-frame 5000 $\mathring{A}$. The histograms above and the right of the main panel show the distribution of mass and n respectively. Sérsic indices of local QGs from SDSS are shown in black and the predictions by Zahid et al. (2019, Z+19) are shown in coloured curves. Z+19 masses are corrected for their offset compared to the mass measurements used in this study.

explain the size evolution of massive QGs observed in this study, though minor mergers and accretion probably play an important role. Under the assumption that the Zahid et al. (2019) model predicts the evolution in Sérsic index due to minor mergers accurately, we conclude that other processes (e.g., progenitor bias, adiabatic expansion) have a non-negligible effect on the structural evolution of QGs in our sample.

We cannot investigate the processes that contribute to the evolution of the QG size-mass relation separately using the current data set. We plan to incorporate age indicators such as colours in our future work because galaxy ages will help us analyse progenitor bias. Furthermore, studying the ages of the massive compact galaxies ($\log M_*/M_\odot > 10.5$ and $R_e < 2$ kpc) could help us understand the impact of adiabatic expansion and minor mergers on these objects. These processes should favour younger compact galaxies over older population, because both the expansion and mergers produce an increase in galaxy size over time. We could also study the number density of AGN and the evolution of their activity since $z \sim 0.9$ to separate the impact of adiabatic expansion from minor mergers and accretion. Studying the environment of all galaxies may help us understand the contribution of minor mergers and accretion processes (Section 1.2.3). We could address this in our future works by looking at the number of close companions of galaxies in our sample and analysing the impact of minor mergers on the morphological evolution of QGs with the help of merger fraction and timescales obtained from cosmological simulations such as Illustris (Nelson et al. 2019). We could also explore the observed evolution in the pivot mass (M_p) that separates massive QGs with strong correlation between size and stellar mass from low mass QGs with weak correlation. This analysis of the evolution in M_p might help us understand how the impact of various physical processes driving the evolution in QGs changes with time provided that the contributions from these processes differ between low mass galaxies ($M_* < M_p$) and high mass galaxies ($M_* > M_p$).

7.3 Effects of Environment

Numerous studies show that environment affects the star formation activity and the morphology of galaxies (e.g., Balogh et al. 2016; Peng et al. 2010b, 2015; Chartab et al. 2020). Denser environments favour elliptical QGs over disky SFGs, because such environments enhance galaxy-galaxy interactions (Section 1.2.3). Several studies address the environmental impact on galaxy morphologies by studying galaxies in galaxy groups, clusters and cores of the clusters as compared to galaxies in the field or low density environments (Gutiérrez et al. 2004; Rettura et al. 2010; Cooper et al. 2012; Lani et al. 2013; Scoville et al. 2013; Newman et al. 2014). In this study, we investigate galaxies in clusters (which include both cluster outskirts and cores) and cluster cores along with the parent population that includes all galaxies.

We do not find any significant difference in the size-mass relation between the members of rich clusters in COSMOS (which include cluster outskirts and cores) and the parent QG population (Figure 6.8). Both the intercepts and the slopes of the size-mass relation for the cluster galaxies are similar to the parameters of the size-mass relation for their parent population. Our COSMOS cluster sample suffers from low number statistics as we have analysed the morphologies of only 75 identified rich cluster members. We suspect that the apparent lack of difference in the size-mass relation between members of rich clusters and non-cluster galaxies is because our investigation is limited to galaxies more massive than $10^{10}\mathrm{M}_{\odot}$. Several studies indicate that mass quenching dominates at higher masses ($\log(M_*/\mathrm{M}_{\odot}) \gtrsim 10.2$) and environmental quenching dominates at lower masses ($\log(M_*/\mathrm{M}_{\odot}) \lesssim 10.2$, Peng et al. 2010b; Moutard et al. 2018; Chartab et al. 2020). Since galaxy quenching contributes to progenitor bias in QGs (Section 1.2.2), the impact of the environmental quenching mechanism should be more prominent at lower masses than higher masses. Hence, studies that investigate lower mass regimes are needed to better understand the impact of the global cluster environment on the QG population. Although other processes such as minor mergers and accretion can also affect size evolution, our study in massive QGs in COSMOS clusters does not show any evidence for different effects that these processes may have in clusters against the field.

We use K-S test to probe the effect of the environment on the size distribution of galaxies that are cluster members in COSMOS. To do this, we compare the size distribution of the COSMOS cluster galaxies and the parent COSMOS QG population in three mass bins (Figure 7.5). We find that the p-values are greater than 0.4 in all mass bins. Thus, the size distributions are not significantly different from each other. The Anderson Darling test[2]

---

[2] The Anderson Darling test is a modification of the K-S test to give more weight to the tails of the distri-

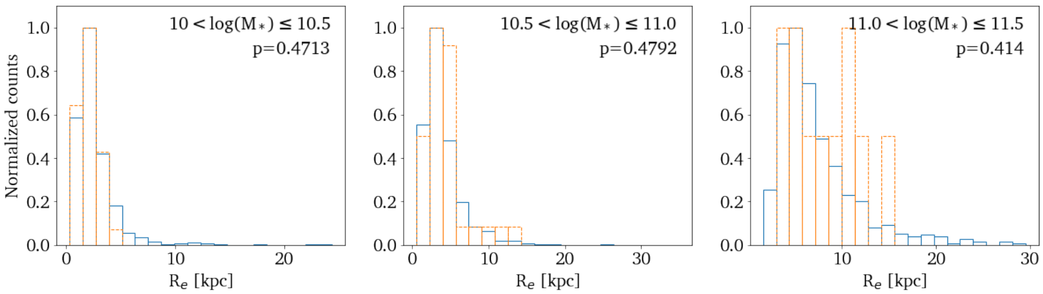

Figure 7.5: Size distribution (rest-frame 5000 *Å*) in three mass bins. Blue histograms show the distribution of the parent COSMOS QG population and orange histograms represent galaxies identified as cluster members in COSMOS. Heights of the largest bins are normalised to 1. p-values from K-S test are given in each panel.

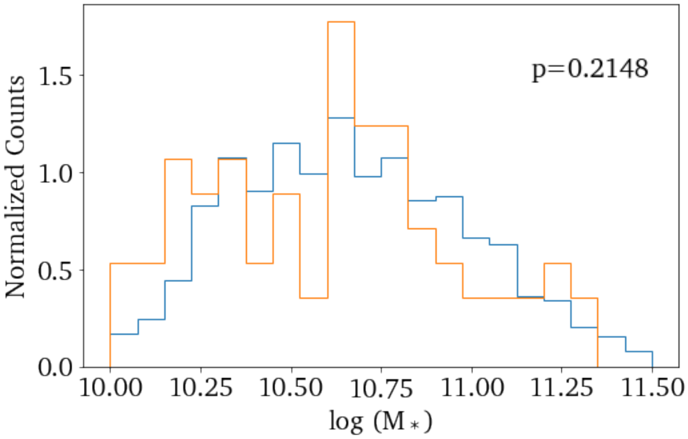

Figure 7.6: Mass distribution of COSMOS cluster members (orange) and the parent COSMOS QG population (blue). The p-value from the K-S test is also given.

(Anderson & Darling 1952; Stephens 1974) also gives similar results. These statistical tests may not be affected significantly by the difference in the mass distribution of the parent and cluster samples because the mass distributions are not statistically different (Figure 7.6), although the smaller size of the COSMOS cluster sample is a concern especially in the highest mass bin ($11 < \log(M_*/\mathrm{M}_\odot \leq 11.5$) with only 11 cluster members[3]. Thus, our analysis suggests that the environment may not alter the size distribution of massive galaxies in clusters.

The trend in the Sérsic index-mass relation of these cluster members (Figure 7.7) is also similar to the whole QG population studied; the Sérsic index monotonically increases with stellar mass. However, the average values in n are slightly different between cluster and parent populations. The median values of n for cluster galaxies are lower than those for the parent population at lower masses ($\log(M_*/\mathrm{M}_\odot) \lesssim 10.5$) and this is probably a result of enhanced progenitor bias in the cluster sample due to newly quenched galaxies being added to the sample through environmental quenching. In contrast, the median values of n are higher for the cluster members than their parent QG sample at higher masses ($\log(M_*/\mathrm{M}_\odot) \gtrsim 10.5$). These higher values of n at higher masses in cluster QGs may indicate minor mergers and accretion are important at the cluster outskirts. However, we can investigate the impact of progenitor bias and mergers only by incorporating galaxy ages. Progenitor bias should yield younger galaxies (with lower n) at lower masses while

---

butions than the K-S test.

[3] The Anderson Darling test is not robust if the sample size is very small ($\lesssim 20$).

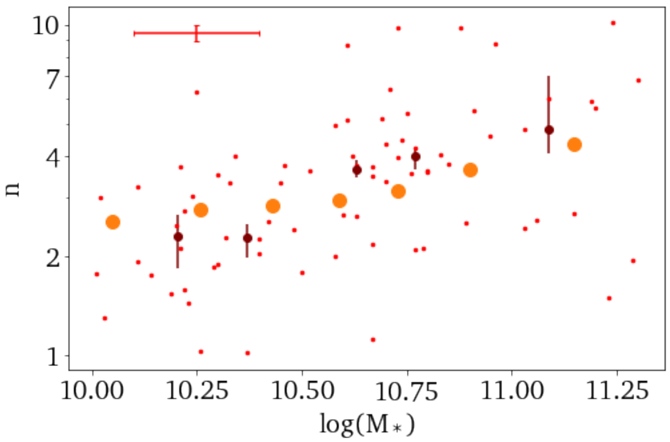

Figure 7.7: Relation between Sérsic index and stellar mass of cluster member galaxies in COSMOS. Measurement uncertainties present in *n* and mass are shown as error bars in the top left corner. Median Sérsic indices in different mass bins are denoted by larger data points (maroon) with their error bars obtained through bootstrapping. Median values of *n* of the parent QG sample are shown in orange. Note that the error bars in the median values of *n* of the parent sample are smaller than the data points.

growth through galaxy interactions should result in older population (with higher *n*) at higher masses. We will address this in future works. We will also be able to improve our statistics by studying a larger cluster sample in the complete CLAUDS+HSC-SSP area.

The environmental effects are clearer in the cores of clusters because the difference between HST CLASH cluster core members and the COSMOS QG population is significant. Galaxies in cluster cores are smaller than their field counterparts at higher masses ($\log(M_*/\mathrm{M}_\odot) \gtrsim 10.2$) but both cluster core and field galaxies have comparable sizes at $\log(M_*/\mathrm{M}_\odot) \lesssim 10.2$. Consequently, cluster core galaxies have a weaker size-mass relation. These observed characteristics of the size-mass relation of galaxies in the cluster cores (Figure 6.12) are probably a result of the combined effects of progenitor bias, harassment and

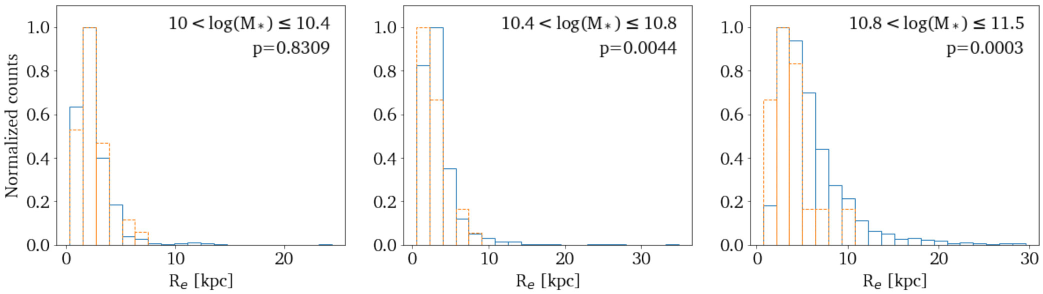

Figure 7.8: Size distribution in three mass bins. The blue histograms show the distribution of the COSMOS QG population and the orange histograms show the distribution of the HST CLASH galaxies. The heights of the most populated bins are normalised to 1. The p-values from the K-S test are given in each panel.

tidal stripping. Progenitor bias arising from environmental quenching mechanisms such as strangulation (Section 1.2.3) yields extended young galaxies ($D_n4000 < 1.5$) at lower masses (left panel in Figure 6.12). At the same time, harassment and tidal stripping prevent galaxies from growing in size and instead remove their stellar populations from the galaxy outskirts. Consequently, the slope of the size-mass relation flattens in the cluster cores.

Therefore, in the cluster core environments, we report an evolutionary scenario that may be different than in lower density environments (including cluster outskirts and galaxy groups). We investigate the effects of the environment on the size evolution further using a K-S test. A K-S test between COSMOS QGs and HST CLASH cluster member galaxies in three mass bins (Figure 7.8) shows that the size distribution of both populations are statistically different from each other at higher masses ($M_* > 10^{10.4}\,\mathrm{M}_\odot$), although the distributions are statistically indistinguishable at lower masses ($M_* < 10^{10.4}\,\mathrm{M}_\odot$). This bolsters our hypothesis that the evolution of galaxies in cluster cores is different than in other environments due to higher efficiency of environmental processes such as tidal stripping and harassment at least at $M_* > 10^{10.4}\,\mathrm{M}_\odot$. The K-S test results are also consistent with the disappearance of older galaxies via minor mergers with the BCG or extreme tidal disruptions (galactic cannibalism). Galaxies with higher masses are more susceptible to dynamical friction than galaxies with lower masses (Chandrasekhar 1942) and they eventually merge with BCGs losing their orbital energy. This process results in the absence of young galaxies ($D_n4000 < 1.5$) with higher masses near the cluster centre (Figure 6.11). Thus, we infer that environment plays a major role in the morphological evolution of galaxies in the cluster cores.

Our analysis of the cluster cores is also limited by the sample size. Limitation in the sample size will be addressed in future works by measuring stellar masses of the cluster members identified through the red sequence in this study. Additionally, we could observe these clusters using spectroscopy to confirm the membership of the red sequence selected members. In this study, we have assumed that all members selected using the red sequence are old but with the D_n4000 index estimated from spectroscopic data, we could confirm their age.

Chapter 8

Conclusions

We measure the morphology (size and concentration of light profiles) of SFGs and QGs in the COSMOS/UltraVISTA region at $0.1 < z < 0.9$ using the g, r, i and z bands from the CLAUDS+HSC-SSP survey. Additionally, we also measure the morphology of galaxies residing in the cores of 5 HST CLASH clusters at $0.18 < z < 0.29$ using f814w images. We perform simulations to estimate the systematic uncertainties present in the measurements of galaxy morphology. With the help of these morphology measurements, we have investigated the evolution of morphology for SFGs and QGs separately and the factors that contribute to the observed evolution.

At all redshifts within $0.1 < z \leq 0.9$, we confirm the previously known result that SFGs and QGs differ significantly in their morphologies. At rest-frame 5000 $\AA$, SFGs are larger in size than QGs at a given stellar mass and redshift. However, QGs have more centrally concentrated light profiles than do SFGs.

We study the size-mass relation of QGs and SFGs in CLAUDS+HSC-SSP data by fitting a linear relation between galaxy size (R_e) at rest-frame 5000 $\AA$ and stellar mass ($M_*/\mathrm{M}_\odot$) in log-log space. We estimate galaxy sizes at rest-frame 5000 $\AA$ either by correcting the size measurements in i-band or using a combination of r, i and z bands to bracket rest-frame 5000 $\AA$ at a given redshift. Consistency in the observed size-mass relations between both methods indicates the robustness of the results from this thesis. Based on the best-fit size-mass relation in five redshift bins, we estimate the evolution in characteristic sizes of galaxies at a fixed mass ($M_* = 5 \times 10^{10}$ $\mathrm{M}_\odot$) since $z \sim 1$, $R_e \propto (1+z)^\beta$. Additionally, we analyse the size-mass relation of cluster galaxies in COSMOS and galaxies in the cores of the CLASH clusters.

Following are the important results from this thesis:

1. We confirm a weak correlation between the size and mass for SFGs ($M_* > 10^{9.5}$ $\mathrm{M}_\odot$); at $0.1 < z < 0.9$, the slopes of the size-mass relation, $\frac{d\log(R_e/\mathrm{kpc})}{d\log(M_*/\mathrm{M}_\odot)}$, for SFGs range from $\sim 0.2-0.3$. We also find a weak evolution in the slopes of the size-mass relation for SFGs over the redshift range we probe: the slope steepens with cosmic time for SFGs. The observed redshift evolution of the characteristic sizes of SFGs in this study ($\beta = -0.45 \pm 0.11$) is slower for SFGs compared to previous studies at higher redshifts ($z > 1$).

2. The evolution of the SFG size-mass relation can be understood by the changing frac-

tions of red ($U-V>1$ in rest-frame) and blue ($U-V\leq 1$ in rest-frame) SFGs with redshift. Our results show that the fraction of red SFGs increases with cosmic time while the fraction of blue SFGs decreases. Since blue SFGs tend to have larger sizes and lower masses than red SFGs, a high abundance of blue SFGs can flatten the size-mass relation of SFGs. However, as the fraction of blue SFGs decreases with cosmic time, the slope of the size-mass relation steepens to lower redshifts, as is observed in our data.

3. Consequently, the changing SFG red fraction can contribute to the changing pace of size evolution in the SFG population. Larger blue SFGs become less abundant with cosmic time and this decreasing fraction of blue SFGs affects the overall size distribution of SFGs. The increase in the abundance of smaller red SFGs with respect to blue SFGs slows down the pace of the size growth in SFGs.

4. The morphological features of SFGs and the increasing red fraction are consistent with the growth of bulges in SFGs. The distribution of Sérsic indices has a more prominent high Sérsic index tail for red SFGs than blue SFGs, implying that more red SFGs are bulge dominated than blue SFGs.

5. We confirm the strong correlation between the size and mass for massive QGs (more massive than the pivot mass (M_p) that separates massive QGs from low mass QGs); at $0.1<z<0.9$, the range of slopes of the size-mass relation for massive QGs is

$\sim 0.6-0.9$. We find a weak evolution in the slopes of the size-mass relation for QGs since $z \sim 1$: the slope becomes shallower with cosmic time. We also confirm the redshift evolution of the characteristic sizes of QGs at a faster pace ($\beta = -1.06 \pm 0.11$) compared to SFGs over the redshift range we probe.

6. Based on our analysis of the Sérsic index-mass relation, we conclude that minor mergers play an important role in the evolution of QGs. However, the semi-empirical model that is most consistent with the minor merger scenario alone cannot reproduce the observed Sérsic index-mass relation. Therefore, we speculate that the evolution in size-mass relation for QGs may be the result of more than one physical process.
7. We observe an evolution in the pivot point in the size-mass relation for QGs that separates massive QGs from low mass QGs. The mass at the pivot point (M_p) shifts to lower masses with cosmic time. Thus, as the Universe ages, more low mass QGs enter the steeper size-mass relation.
8. The size-mass relation of the massive QGs in the clusters in the COSMOS/UltraVISTA region is similar to that of the massive QGs in the field. This similarity shows that environment has no significant effect on the morphology of massive QGs at $0.1 < z < 0.9$. However, there is some difference in the Sérsic index-mass relation of QGs in the clusters and the field. At intermediate masses ($10 \lesssim \log(M_*/M_\odot) \lesssim 10.5$), QGs in the clusters have lower Sérsic index compared to QGs with same masses in

the field, which suggests that the galaxies at this mass range in the clusters may have a significant fraction of newly quenched disky galaxies. In contrast, at higher masses than $\log(M_*/M_\odot) \sim 10.5$, cluster QGs have lower Sérsic index than field QGs suggesting that evolution of galaxies through minor mergers and/or accretion at cluster environments may be stronger than in the field. A stronger evolution through the mergers and/or accretion at higher masses can compensate the progenitor bias in the lower masses thereby maintaining a uniform slope of the size-mass relation.

9. The morphology of galaxies in the cores of the HST CLASH clusters differ significantly from the galaxies in the field. The size-mass relation of galaxies with higher masses ($\log(M_*/M_\odot) \gtrsim 10$) in the cluster cores has a slope of ~ 0.33, in stark contrast with the slope of similar galaxies in the field at $0.1 < z < 0.3$ (~ 0.61).
10. QGs with lower masses ($\log(M_*/M_\odot) \lesssim 10.2$) in the cluster cores are comparatively larger than their counterparts in the field. Moreover, these low mass galaxies in the cluster cores are generally younger than more massive core galaxies. The sizes and ages of QGs at lower masses imply a progenitor bias arising from the quenching of galaxies in the cluster cores at lower masses.
11. Galaxies with higher masses ($\log(M_*/M_\odot) \gtrsim 10.2$) in the cluster cores, on the other hand, are smaller than those in the field. We infer that the difference in the sizes of massive galaxies and the slope of the size-mass relation in cluster cores with respect

to the general quiescent population may be due to their extreme environment that suppresses galaxy growth through mergers or accretion.

In summary, we find evidence for bulge growth in the SFGs that slows down the evolution in SFG sizes. The observed features in the size-mass relation for QGs can be caused by several factors including progenitor bias, fading of disks, minor mergers and adiabatic expansion. Although we do not find any significant difference in the morphological evolution of massive QGs ($M_* > M_p$) between cluster environment and the field in COSMOS, our results from the analysis of the morphology of galaxies in the HST CLASH data show that the extreme environments play a dominant role in the evolution of galaxies in the cores of clusters.

8.1 Future Directions

We intend to extend our morphological studies to the entire 18.6 deg^2 of the CLAUDS+HSC-SSP in U, g, r, i, z and y bands at $0.1 < z < 0.9$. Such a large sky coverage will help us to reduce the impact of large scale structures and sample variance in our data. Inclusion of the U-band will enable us to analyse how quenching affects galaxy morphology because comparing galaxy morphology in the U-band and at longer wavelengths (e.g., z-band) can give insight into the differences between regions with young stars (blue) and those with predominantly old stars (red) in a galaxy. Moreover, we could utilise the U-band data along with longer wavelength datasets to constrain spatially resolved galaxy spectral energy distributions and thereby, analyse the central concentration of stellar mass and star formation in galaxies.

We could study the impact of several processes on galaxy morphology in the CLAUDS+HSC-SSP sample as discussed in Chapter 7 by incorporating age indicators such as rest-frame colours. Studying the environment of each galaxy studied by looking at the number of its close companions could help us analyse the minor merger and accretion driven growth scenario in QGs. Constraining merger fractions with the results from simulations such as Illustris could additionally help us to understand the extent to which minor mergers affect the observed evolution in QG morphology. Besides, one could address the impact of adiabatic expansion on the evolution of QGs by studying the evolution in the number density of AGNs since $z \sim 1$. Furthermore, multi-component fitting of galaxy light profiles would enable us to measure B/T ratios and quantify bulge growth in SFGs.

In our future work, we will measure the masses of all the galaxies identified as members of HST CLASH clusters using the red sequence method, which will more than double the current sample size to study the size-mass relation of galaxies in the cluster cores. We also intend to observe these members identified by the red sequence method with spectroscopy, which will help us to confirm their membership and constrain their ages.

Appendix A

Simulation Results in g, r and z Bands

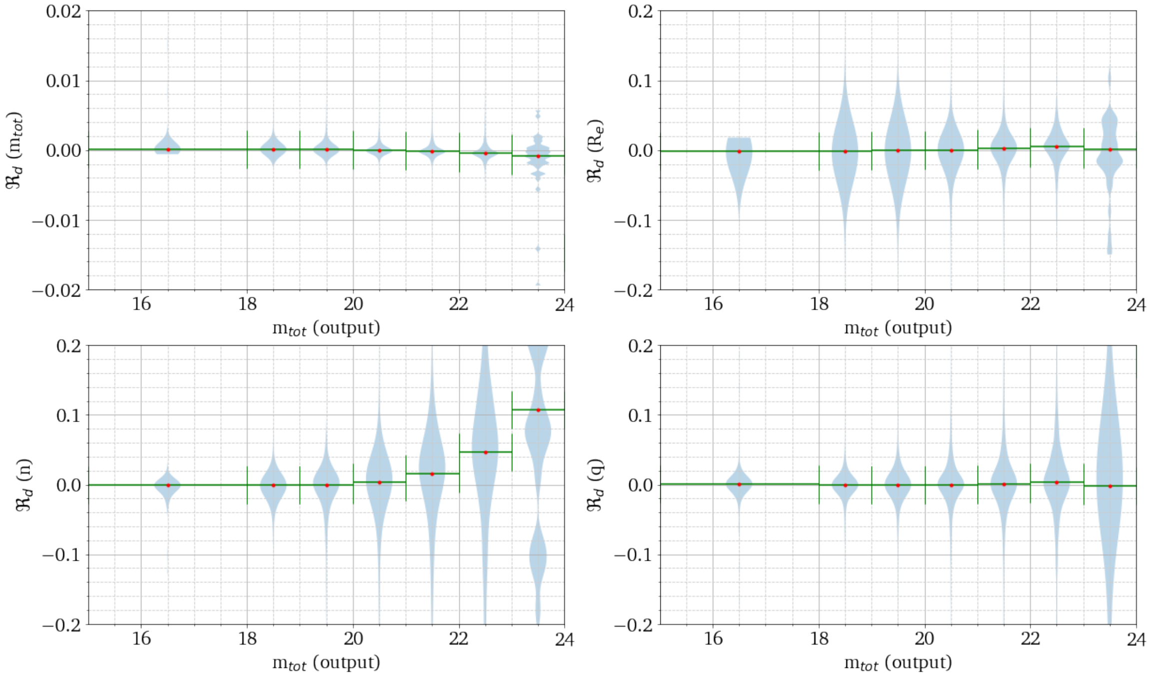

A

Figure A.1: Violin plots of relative difference ($\Re_d$) in parameters as a function of output parameters in g-band (Section 5.2). Details are same as Figure 5.9. A: $\Re_d$ as a function of output magnitude; B: $\Re_d$ as a function of output size; C: $\Re_d$ as a function of output Sérsic index. Note that the scaling in y-axis is not uniform across the panels.

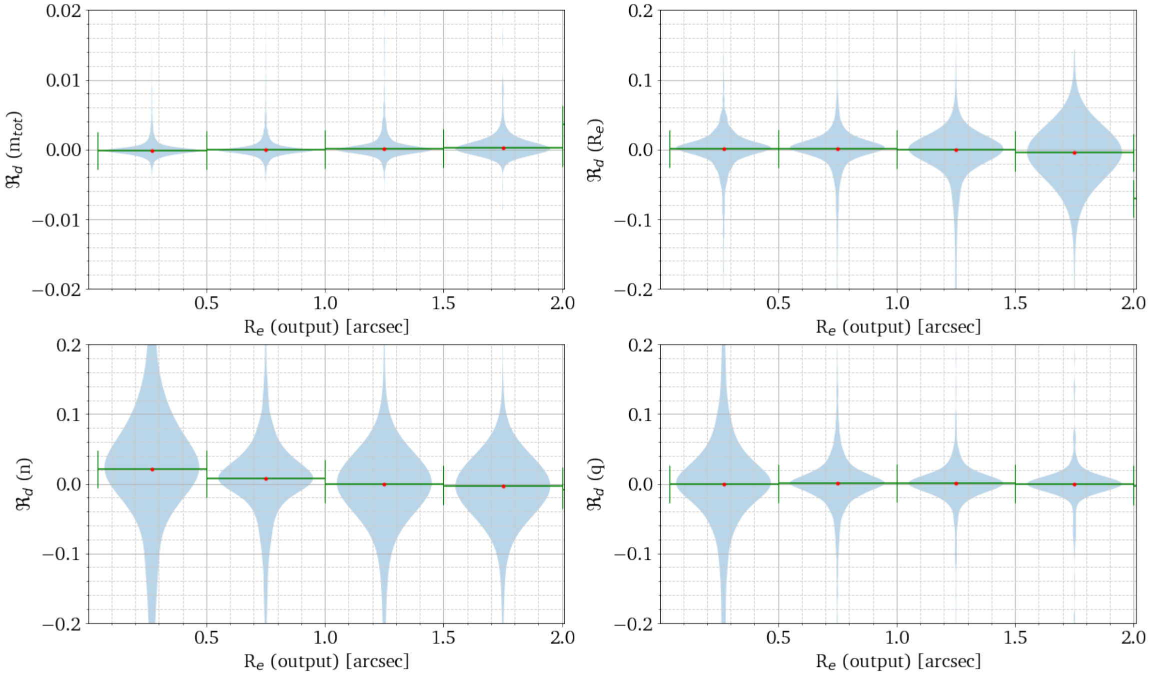

B

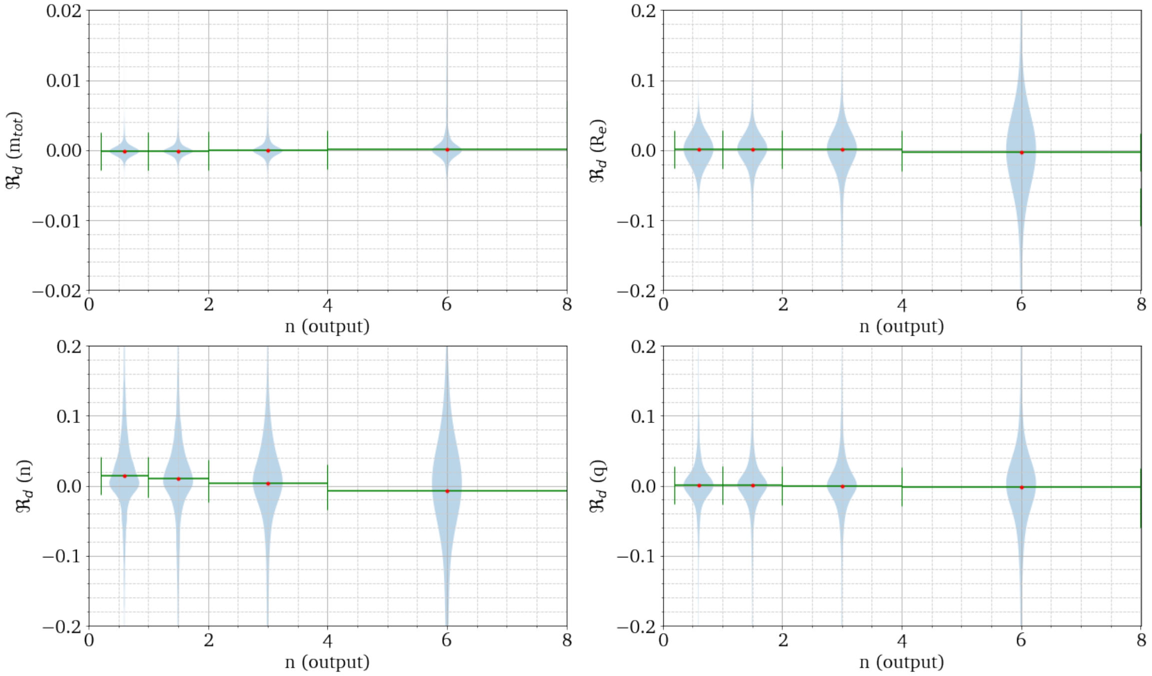

C

Figure A.1: Violin plots of relative difference ($\Re_d$) in parameters as a function of output parameters in g-band (continued)

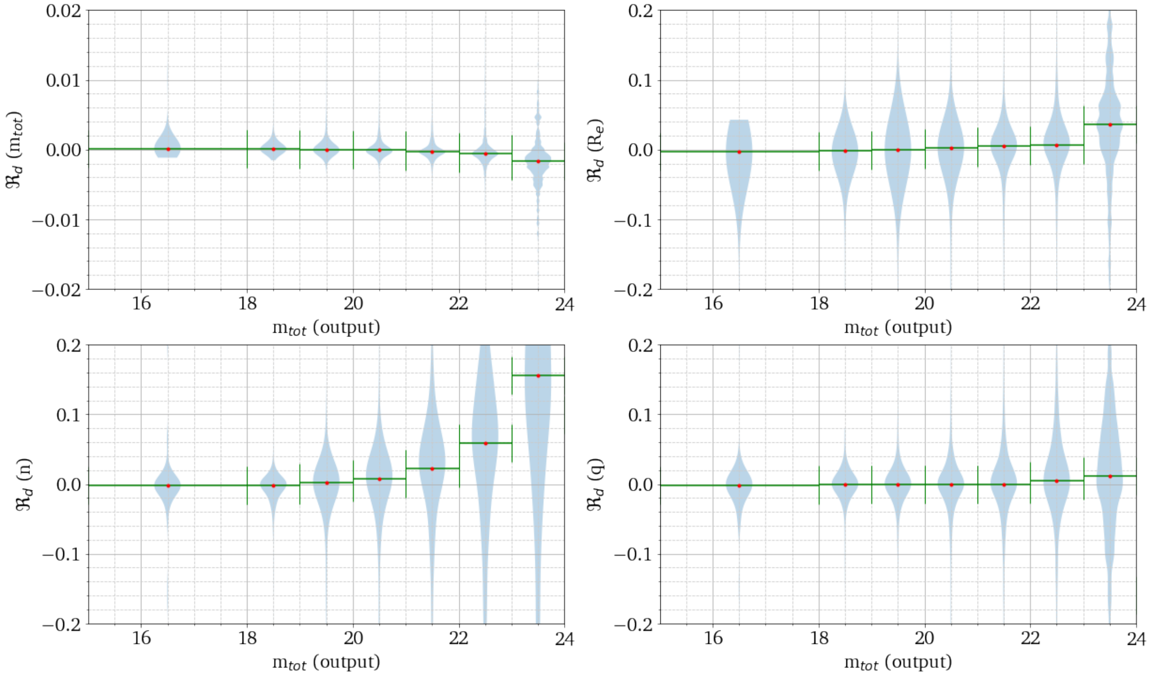

A

Figure A.2: Violin plots of relative difference ($\Re_d$) in parameters as a function of output parameters in r-band (Section 5.2). Details are same as Figure 5.9. A: $\Re_d$ as a function of output magnitude; B: $\Re_d$ as a function of output size; C: $\Re_d$ as a function of output Sérsic index. Note that the scaling in y-axis is not uniform across the panels.

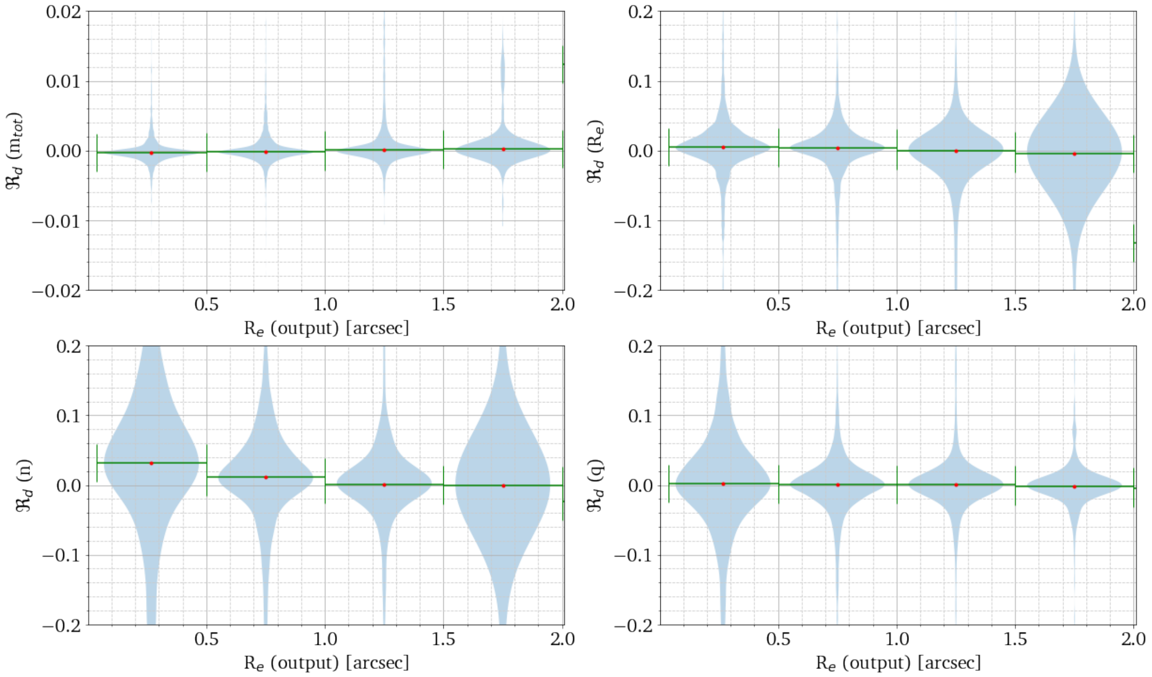

B

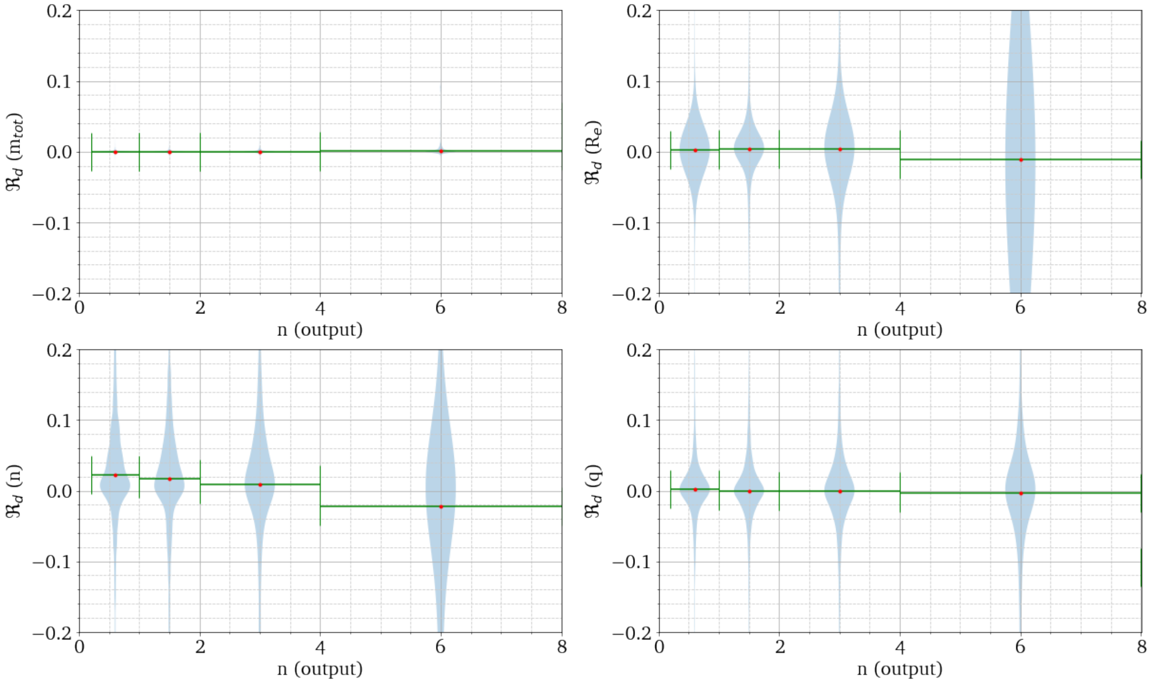

C

Figure A.2: Violin plots of relative difference ($\Re_d$) in parameters as a function of output parameters in *r*-band (continued)

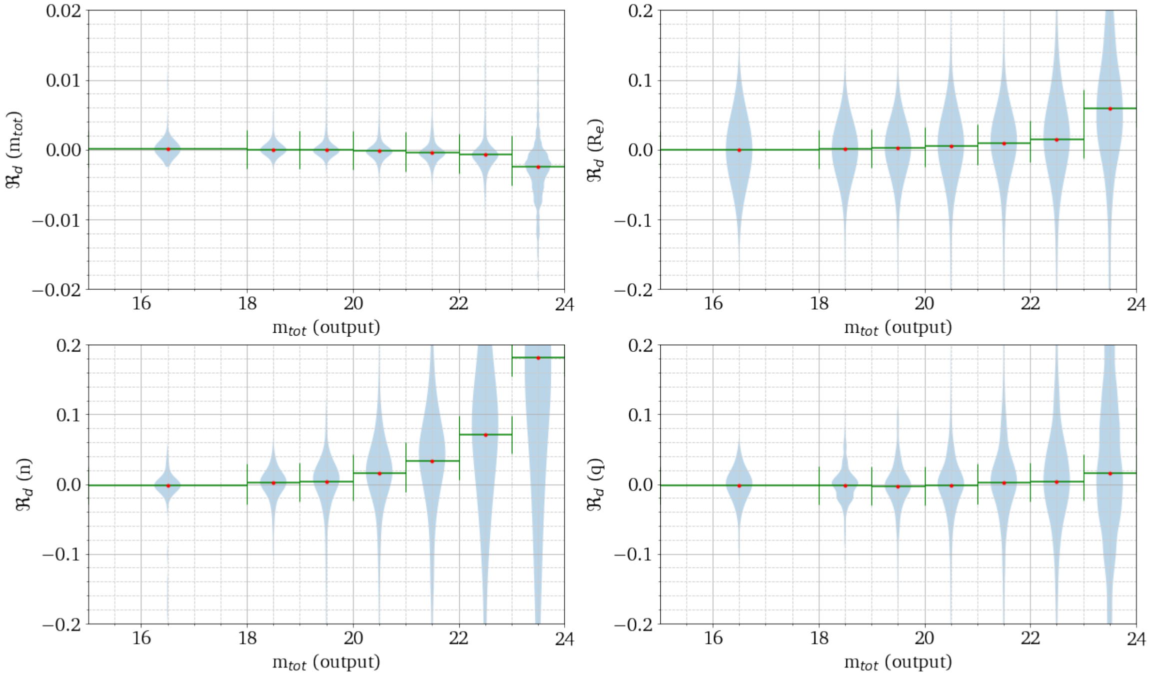

A

Figure A.3: Violin plots of relative difference ($\mathfrak{R}_d$) in parameters as a function of output parameters in z-band (Section 5.2). Details are same as Figure 5.9. A: $\mathfrak{R}_d$ as a function of output magnitude; B: $\mathfrak{R}_d$ as a function of output size; C: $\mathfrak{R}_d$ as a function of output Sérsic index. Note that the scaling in y-axis is not uniform across the panels.

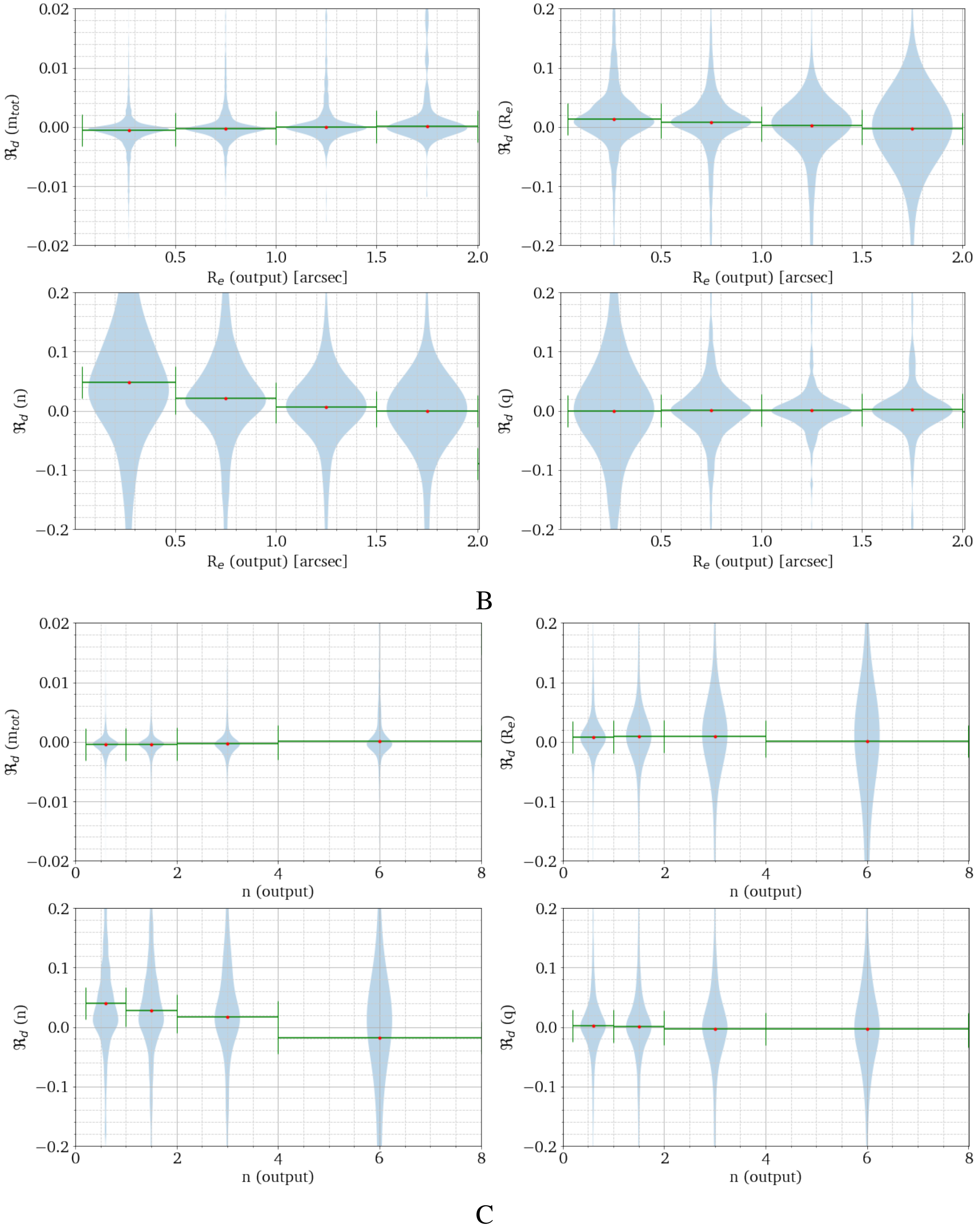

Figure A.3: Violin plots of relative difference ($\Re_d$) in parameters as a function of output parameters in z-band (cont.)

Appendix B

Size-Mass Relation using r, i and z Bands

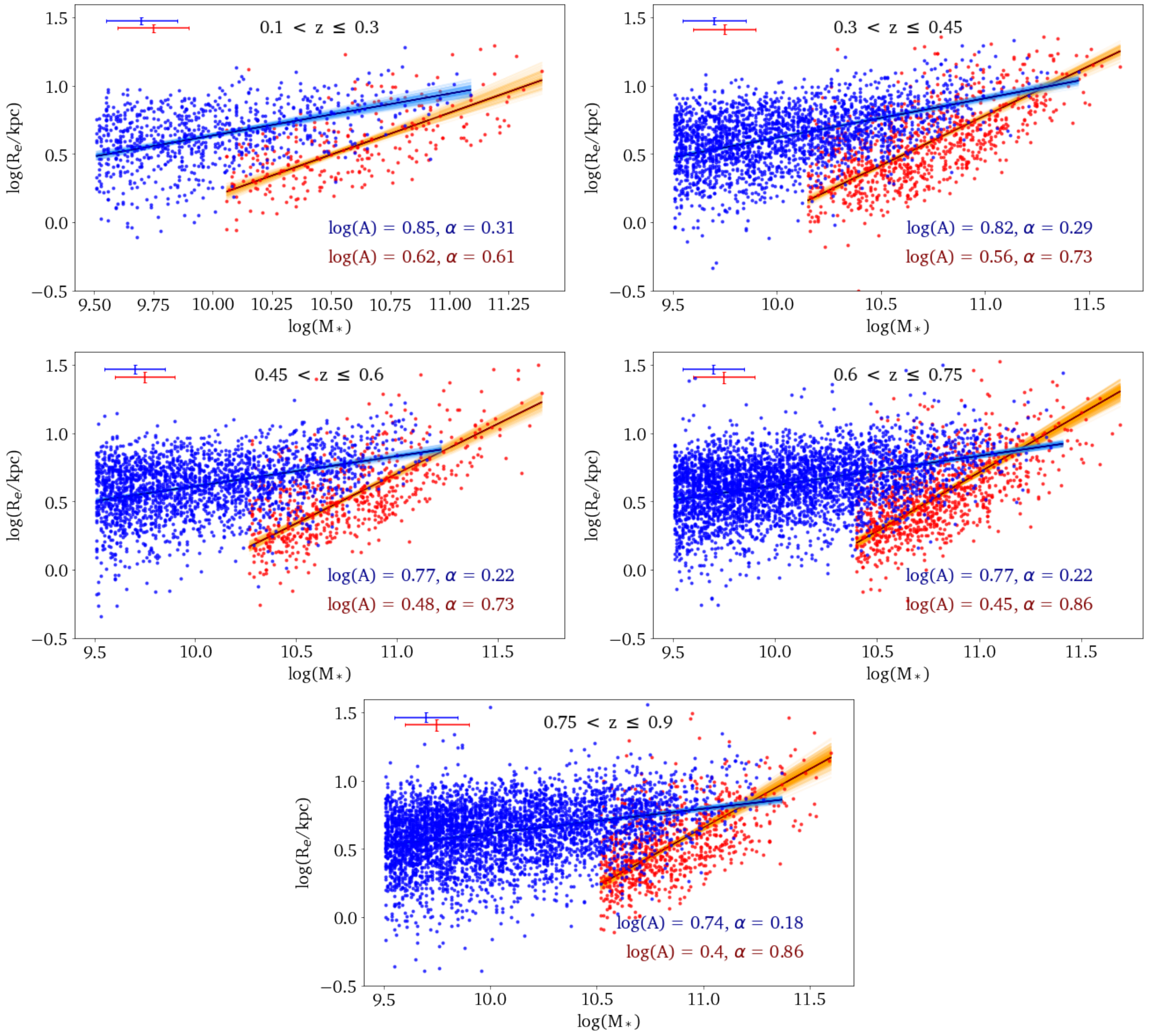

Figure B.1: Linear fits to the size-mass relation of galaxies in rest-frame 5000$\mathring{A}$ obtained using the combination of r, i and z bands (Section 6.1). Massive QGs are selected using M_p obtained through Equation 6.1.6. Rest of the details are same as Figure 6.2. Note that the scaling in x-axis is not uniform across the panels.

Bibliography

Aguilar L. A., White S. D. M., 1986, The Astrophysical Journal, 307, 97

Aihara H., et al., 2019, Publications of the Astronomical Society of Japan, 71, 114

Anderson T. W., Darling D. A., 1952, Annals of Mathematical Statistics, 23, 193

Andreon S., 2018, Astronomy and Astrophysics, 617, A53

Arnouts S., Cristiani S., Moscardini L., Matarrese S., Lucchin F., Fontana A., Giallongo E., 1999, Monthly Notices of the Royal Astronomical Society, 310, 540

Athanassoula E., 2005, Monthly Notices of the Royal Astronomical Society, 358, 1477

Balogh M. L., Morris S. L., Yee H. K. C., Carlberg R. G., Ellingson E., 1999, The Astrophysical Journal, 527, 54

Balogh M. L., Navarro J. F., Morris S. L., 2000, The Astrophysical Journal, 540, 113

Balogh M. L., et al., 2016, Monthly Notices of the Royal Astronomical Society, 456, 4364

Barden M., et al., 2005, The Astrophysical Journal, 635, 959

Barden M., Häußler B., Peng C. Y., McIntosh D. H., Guo Y., 2012, Monthly Notices of the Royal Astronomical Society, 422, 449

Baumgardt H., Kroupa P., 2007, Monthly Notices of the Royal Astronomical Society, 380, 1589

Benítez N., 2000, The Astrophysical Journal, 536, 571

Benítez N., et al., 2004, The Astrophysical Journal Supplement Series, 150, 1

Benson A. J., 2010, Physics Reports, 495, 33

Bertin E., 2011, in Evans I. N., Accomazzi A., Mink D. J., Rots A. H., eds, Astronomical Society of the Pacific Conference Series Vol. 442, Astronomical Data Analysis Software and Systems XX. p. 435

Bertin E., Arnouts S., 1996, Astronomy and Astrophysics Supplement Series, 117, 393

Bertin G., Ciotti L., Del Principe M., 2002, Astronomy and Astrophysics, 386, 149

Bezanson R., van Dokkum P. G., Tal T., Marchesini D., Kriek M., Franx M., Coppi P., 2009, The Astrophysical Journal, 697, 1290

Bezanson R., van Dokkum P., Franx M., 2012, The Astrophysical Journal, 760, 62

Binney J., Tremaine S., 1987, Galactic Dynamics. Princeton University Press, Princeton

Blakeslee J. P., Tonry J. L., 1992, The Astronomical Journal, 103, 1457

Blanton M. R., Moustakas J., 2009, Annual Review of Astronomy and Astrophysics, 47, 159

Boily C. M., Kroupa P., 2003, Monthly Notices of the Royal Astronomical Society, 338, 673

Bosch J., et al., 2018, Publications of the Astronomical Society of Japan, 70, S5

Bournaud F., Elmegreen B. G., 2009, The Astrophysical Journal Letters, 694, L158

Bower R. G., Lucey J. R., Ellis R. S., 1992a, Monthly Notices of the Royal Astronomical Society, 254, 589

Bower R. G., Lucey J. R., Ellis R. S., 1992b, Monthly Notices of the Royal Astronomical Society, 254, 601

Boylan-Kolchin M., Ma C.-P., Quataert E., 2006, Monthly Notices of the Royal Astronomical Society, 369, 1081

Brammer G. B., van Dokkum P. G., Coppi P., 2008, The Astrophysical Journal, 686, 1503

Brammer G. B., et al., 2011, The Astrophysical Journal, 739, 24

Brinchmann J., Charlot S., White S. D. M., Tremonti C., Kauffmann G., Heckman T., Brinkmann J., 2004, Monthly Notices of the Royal Astronomical Society, 351, 1151

Bruzual G., Charlot S., 2003, Monthly Notices of the Royal Astronomical Society, 344, 1000

Bullock J. S., Kolatt T. S., Sigad Y., Somerville R. S., Kravtsov A. V., Klypin A. A., Primack J. R., Dekel A., 2001, Monthly Notices of the Royal Astronomical Society, 321, 559

Bundy K., Fukugita M., Ellis R. S., Targett T. A., Belli S., Kodama T., 2009, The Astrophysical Journal, 697, 1369

Burke C., Collins C., Stott J., Hilton M., 2013, in Thomas D., Pasquali A., Ferreras I., eds, IAU Symposium Vol. 295, The Intriguing Life of Massive Galaxies. pp 172–173 (`arXiv:1211.1826`), doi:10.1017/S1743921313004602

Calzetti D., Armus L., Bohlin R. C., Kinney A. L., Koornneef J., Storchi-Bergmann T., 2000, The Astrophysical Journal, 533, 682

Carnall A. C., McLure R. J., Dunlop J. S., Davé R., 2018, Monthly Notices of the Royal Astronomical Society, 480, 4379

Carollo C. M., et al., 2013, The Astrophysical Journal, 773, 112

Carollo C. M., et al., 2016, The Astrophysical Journal, 818, 180

Castignani G., Combes F., Salomé P., 2020, Astronomy and Astrophysics, 635, L10

Ceverino D., Dekel A., Bournaud F., 2010, Monthly Notices of the Royal Astronomical Society, 404, 2151

Chabrier G., 2003, Publications of the Astronomical Society of the Pacific, 115, 763

Chandrasekhar S., 1942, Principles of Stellar Dynamics. The University of Chicago press, Chicago

Chartab N., et al., 2020, The Astrophysical Journal, 890, 7

Chen L., 2019, Master's Thesis, Saint Mary's University, Halifax

Christlein D., Zabludoff A. I., 2004, The Astrophysical Journal, 616, 192

Ciambur B. C., 2016, Publications of the Astronomical Society of Australia, 33, e062

Coccato L., Gerhard O., Arnaboldi M., Ventimiglia G., 2011, Astronomy and Astrophysics, 533, A138

Coe D., Benítez N., Sánchez S. F., Jee M., Bouwens R., Ford H., 2006, The Astronomical Journal, 132, 926

Conselice C. J., 2014, Annual Review of Astronomy and Astrophysics, 52, 291

Contini E., De Lucia G., Hatch N., Borgani S., Kang X., 2016, Monthly Notices of the Royal Astronomical Society, 456, 1924

Cooper M. C., et al., 2012, Monthly Notices of the Royal Astronomical Society, 419, 3018

Cox T. J., Jonsson P., Primack J. R., Somerville R. S., 2006, Monthly Notices of the Royal Astronomical Society, 373, 1013

Croton D. J., et al., 2006, Monthly Notices of the Royal Astronomical Society, 365, 11

D'Onofrio M., Marziani P., Buson L., 2015, Frontiers in Astronomy and Space Sciences, 2, 4

Daddi E., et al., 2007, The Astrophysical Journal, 670, 156

Damjanov I., et al., 2009, The Astrophysical Journal, 695, 101

Damjanov I., Zahid H. J., Geller M. J., Hwang H. S., 2015, The Astrophysical Journal, 815, 104

Damjanov I., Zahid H. J., Geller M. J., Fabricant D. G., Hwang H. S., 2018, The Astrophysical Journal Supplement Series, 234, 21

Damjanov I., Zahid H. J., Geller M. J., Utsumi Y., Sohn J., Souchereau H., 2019, The Astrophysical Journal, 872, 91

De Lucia G., et al., 2007, Monthly Notices of the Royal Astronomical Society, 374, 809

Delaye L., et al., 2014, Monthly Notices of the Royal Astronomical Society, 441, 203

Di Matteo T., Springel V., Hernquist L., 2005, Nature, 433, 604

Diaferio A., Geller M. J., 1997, The Astrophysical Journal, 481, 633

Dressler A., 1980, The Astrophysical Journal, 236, 351

Duncan M. J., Farouki R. T., Shapiro S. L., 1983, The Astrophysical Journal, 271, 22

Dutton A. A., 2009, Monthly Notices of the Royal Astronomical Society, 396, 121

Ebeling H., Stephenson L. N., Edge A. C., 2014, The Astrophysical Journal Letters, 781, L40

Elson R. A. W., 1999, in Globular Clusters. 10th Canary Islands Winter School of Astrophysics. pp 209–248

Fabello S., Catinella B., Giovanelli R., Kauffmann G., Haynes M. P., Heckman T. M., Schiminovich D., 2011, Monthly Notices of the Royal Astronomical Society, 411, 993

Fabricant D. G., Hertz E. N., Szentgyorgyi A. H., Fata R. G., Roll J. B., Zajac J. M., 1998, in D'Odorico S., ed., Society of Photo-Optical Instrumentation Engineers (SPIE) Conference Series Vol. 3355, Optical Astronomical Instrumentation. pp 285–296, doi:10.1117/12.316814

Fabricant D., et al., 2005, Publications of the Astronomical Society of the Pacific, 117, 1411

Fagioli M., Carollo C. M., Renzini A., Lilly S. J., Onodera M., Tacchella S., 2016, The Astrophysical Journal, 831, 173

Faisst A. L., Carollo C. M., Capak P. L., Tacchella S., Renzini A., Ilbert O., McCracken H. J., Scoville N. Z., 2017, The Astrophysical Journal, 839, 71

Fan L., Lapi A., De Zotti G., Danese L., 2008, The Astrophysical Journal Letters, 689, L101

Fan L., Lapi A., Bressan A., Bernardi M., De Zotti G., Danese L., 2010, The Astrophysical Journal, 718, 1460

Fang J. J., Faber S. M., Koo D. C., Dekel A., 2013, The Astrophysical Journal, 776, 63

Farouki R., Shapiro S. L., 1981, The Astrophysical Journal, 243, 32

Feldmann R., Quataert E., Hopkins P. F., Faucher-Giguère C.-A., Kereš D., 2017, Monthly Notices of the Royal Astronomical Society, 470, 1050

Ferguson H. C., Binggeli B., 1994, Astronomy and Astrophysics Review, 6, 67

Ferguson H. C., et al., 2004, The Astrophysical Journal Letters, 600, L107

Franx M., van Dokkum P. G., Förster Schreiber N. M., Wuyts S., Labbé I., Toft S., 2008, The Astrophysical Journal, 688, 770

Gabor J. M., Davé R., Finlator K., Oppenheimer B. D., 2010, Monthly Notices of the Royal Astronomical Society, 407, 749

Gadotti D. A., 2009, Monthly Notices of the Royal Astronomical Society, 393, 1531

Geller M. J., Diaferio A., Rines K. J., Serra A. L., 2013, The Astrophysical Journal, 764, 58

Geller M. J., Hwang H. S., Diaferio A., Kurtz M. J., Coe D., Rines K. J., 2014, The Astrophysical Journal, 783, 52

Genzel R., et al., 2011, The Astrophysical Journal, 733, 101

Gladders M. D., Yee H. K. C., 2000, The Astronomical Journal, 120, 2148

Golden-Marx J. B., Miller C. J., 2019, The Astrophysical Journal, 878, 14

Goodwin S. P., Bastian N., 2006, Monthly Notices of the Royal Astronomical Society, 373, 752

Graham A. W., Erwin P., Trujillo I., Asensio Ramos A., 2003, The Astronomical Journal, 125, 2951

Gunn J. E., Gott III J. R., 1972, The Astrophysical Journal, 176, 1

Guo Y., et al., 2017, The Astrophysical Journal Letters, 841, L22

Gutiérrez C. M., Trujillo I., Aguerri J. A. L., Graham A. W., Caon N., 2004, The Astrophysical Journal, 602, 664

Gwyn S. D. J., 2008, Publications of the Astronomical Society of the Pacific, 120, 212

Hausman M. A., Ostriker J. P., 1978, The Astrophysical Journal, 224, 320

Häussler B., et al., 2007, The Astrophysical Journal Supplement Series, 172, 615

Hilz M., Naab T., Ostriker J. P., Thomas J., Burkert A., Jesseit R., 2012, Monthly Notices of the Royal Astronomical Society, 425, 3119

Hopkins P. F., Hernquist L., Cox T. J., Di Matteo T., Robertson B., Springel V., 2006, The Astrophysical Journal Supplement Series, 163, 1

Hopkins P. F., et al., 2010, The Astrophysical Journal, 715, 202

Huang S., Haynes M. P., Giovanelli R., Brinchmann J., 2012, The Astrophysical Journal, 756, 113

Ilbert O., et al., 2006, Astronomy and Astrophysics, 457, 841

Jáchym P., Palouš J., Köppen J., Combes F., 2007, Astronomy and Astrophysics, 472, 5

Kauffmann G., Charlot S., 1998, arXiv e-prints, pp astro–ph/9810031

Kauffmann G., et al., 2003, Monthly Notices of the Royal Astronomical Society, 341, 54

Kaviraj S., et al., 2014, Monthly Notices of the Royal Astronomical Society, 443, 1861

Kawinwanichakij L., et al., 2017, The Astrophysical Journal, 847, 134

Kelly B. C., 2007, The Astrophysical Journal, 665, 1489

Kelvin L. S., et al., 2012, Monthly Notices of the Royal Astronomical Society, 421, 1007

Khochfar S., Silk J., 2006, The Astrophysical Journal Letters, 648, L21

Kodama T., Arimoto N., 1997, Astronomy and Astrophysics, 320, 41

Koekemoer A. M., Fruchter A. S., Hook R. N., Hack W., Hanley C., 2006, in Koekemoer A. M., Goudfrooij P., Dressel L. L., eds, The 2005 HST Calibration Workshop: Hubble After the Transition to Two-Gyro Mode. p. 423

Kolmogorov A., 1933, Inst. Ital. Attuari, Giorn., 4, 83

Kormendy J., 2008, in Proceedings of the IAU Symposium. eprint: arXiv:0708.2104, pp 107–112, doi:10.1017/S1743921308017407

Kormendy J., Kennicutt Jr. R. C., 2004, Annual Review of Astronomy and Astrophysics, 42, 603

Kormendy J., Fisher D. B., Cornell M. E., Bender R., 2009, The Astrophysical Journal Supplement Series, 182, 216

Kriek M., van Dokkum P. G., Labbé I., Franx M., Illingworth G. D., Marchesini D., Quadri R. F., 2009, The Astrophysical Journal, 700, 221

Krist J. E., Hook R. N., Stoehr F., 2011, in Proceedings of the SPIE. p. 81270J, doi:10.1117/12.892762

Kurtz M. J., Mink D. J., 1998, Publications of the Astronomical Society of the Pacific, 110, 934

Lange R., et al., 2015, Monthly Notices of the Royal Astronomical Society, 447, 2603

Lani C., et al., 2013, Monthly Notices of the Royal Astronomical Society, 435, 207

Lapi A., et al., 2018, The Astrophysical Journal, 857, 22

Lauer T. R., et al., 1995, The Astronomical Journal, 110, 2622

Law D. R., Steidel C. C., Erb D. K., Pettini M., Reddy N. A., Shapley A. E., Adelberger K. L., Simenc D. J., 2007, The Astrophysical Journal, 656, 1

Leauthaud A., et al., 2007, The Astrophysical Journal Supplement Series, 172, 219

Lemze D., et al., 2013, The Astrophysical Journal, 776, 91

Li C., Kauffmann G., Jing Y. P., White S. D. M., Börner G., Cheng F. Z., 2006, Monthly Notices of the Royal Astronomical Society, 368, 21

Lilly S. J., Carollo C. M., 2016, The Astrophysical Journal, 833, 1

Lilly S. J., Le Fevre O., Hammer F., Crampton D., 1996, The Astrophysical Journal Letters, 460, L1

Lilly S., et al., 1998, The Astrophysical Journal, 500, 75

Lilly S. J., et al., 2007, The Astrophysical Journal Supplement Series, 172, 70

Lilly S. J., et al., 2009, The Astrophysical Journal Supplement Series, 184, 218

López-Sanjuan C., Balcells M., Pérez-González P. G., Barro G., García-Dabó C. E., Gallego J., Zamorano J., 2010a, in Bruzual G. R., Charlot S., eds, IAU Symposium Vol. 262, Stellar Populations - Planning for the Next Decade. pp 209–212, doi:10.1017/S1743921310002796

López-Sanjuan C., Balcells M., Pérez-González P. G., Barro G., García-Dabó C. E., Gallego J., Zamorano J., 2010b, The Astrophysical Journal, 710, 1170

Lotz J. M., Primack J., Madau P., 2004, The Astronomical Journal, 128, 163

Madau P., Dickinson M., 2014, Annual Review of Astronomy and Astrophysics, 52, 415

Malmquist K. G., 1922, Meddelanden fran Lunds Astronomiska Observatorium Serie I, 100, 1

Malmquist K. G., 1925, Meddelanden fran Lunds Astronomiska Observatorium Serie I, 106, 1

Maraston C., 2005, Monthly Notices of the Royal Astronomical Society, 362, 799

Martig M., Bournaud F., Teyssier R., Dekel A., 2009, The Astrophysical Journal, 707, 250

Martinet N., Durret F., Adami C., Rudnick G., 2017, Astronomy and Astrophysics, 604, A80

Matharu J., et al., 2019, Monthly Notices of the Royal Astronomical Society, 484, 595

Matharu J., et al., 2020, Monthly Notices of the Royal Astronomical Society, 493, 6011

Mayer L., Mastropietro C., Wadsley J., Stadel J., Moore B., 2006, Monthly Notices of the Royal Astronomical Society, 369, 1021

McGaugh S. S., Schombert J. M., 2014, The Astronomical Journal, 148, 77

Mehmood H., 2017, PhD thesis, University of Waterloo

Mo H. J., Mao S., White S. D. M., 1998, Monthly Notices of the Royal Astronomical Society, 295, 319

Moeckel N., Bate M. R., 2010, Monthly Notices of the Royal Astronomical Society, 404, 721

Moffat A. F. J., 1969, Astronomy and Astrophysics, 3, 455

Monna A., et al., 2015, Monthly Notices of the Royal Astronomical Society, 447, 1224

Moore B., Katz N., Lake G., Dressler A., Oemler A., 1996, Nature, 379, 613

Moré J. J., 1978, Lecture Notes in Mathematics, Berlin Springer Verlag, 630, 105

Moresco M., et al., 2013, Astronomy and Astrophysics, 558, A61

Morishita T., Ichikawa T., Kajisawa M., 2014, The Astrophysical Journal, 785, 18

Mosleh M., et al., 2012, The Astrophysical Journal Letters, 756, L12

Moutard T., Sawicki M., Arnouts S., Golob A., Malavasi N., Adami C., Coupon J., Ilbert O., 2018, Monthly Notices of the Royal Astronomical Society, 479, 2147

Moutard T., Sawicki M., Arnouts S., Golob A., Coupon J., Ilbert O., Yang X., Gwyn S., 2020, Monthly Notices of the Royal Astronomical Society, 494, 1894

Mowla L., van der Wel A., van Dokkum P., Miller T. B., 2019a, The Astrophysical Journal Letters, 872, L13

Mowla L. A., et al., 2019b, The Astrophysical Journal, 880, 57

Muzzin A., et al., 2012, The Astrophysical Journal, 746, 188

Muzzin A., et al., 2013a, The Astrophysical Journal Supplement Series, 206, 8

Muzzin A., et al., 2013b, The Astrophysical Journal, 777, 18

Naab T., Jesseit R., Burkert A., 2006, Monthly Notices of the Royal Astronomical Society, 372, 839

Naab T., Johansson P. H., Ostriker J. P., Efstathiou G., 2007, The Astrophysical Journal, 658, 710

Naab T., Johansson P. H., Ostriker J. P., 2009, The Astrophysical Journal Letters, 699, L178

Nelson D., et al., 2019, Computational Astrophysics and Cosmology, 6, 2

Newman A. B., Ellis R. S., Bundy K., Treu T., 2012, The Astrophysical Journal, 746, 162

Newman A. B., Ellis R. S., Andreon S., Treu T., Raichoor A., Trinchieri G., 2014, The Astrophysical Journal, 788, 51

Nipoti C., Stiavelli M., Ciotti L., Treu T., Rosati P., 2003, Monthly Notices of the Royal Astronomical Society, 344, 748

Nipoti C., Treu T., Ciotti L., Stiavelli M., 2004, Monthly Notices of the Royal Astronomical Society, 355, 1119

Oesch P. A., et al., 2010, The Astrophysical Journal Letters, 709, L21

Oguri M., 2014, Monthly Notices of the Royal Astronomical Society, 444, 147

Oguri M., et al., 2018, Publications of the Astronomical Society of Japan, 70, S20

Oser L., Ostriker J. P., Naab T., Johansson P. H., Burkert A., 2010, The Astrophysical Journal, 725, 2312

Oser L., Naab T., Ostriker J. P., Johansson P. H., 2012, The Astrophysical Journal, 744, 63

Pannella M., et al., 2015, The Astrophysical Journal, 807, 141

Peng C. Y., Ho L. C., Impey C. D., Rix H.-W., 2002, The Astronomical Journal, 124, 266

Peng C. Y., Ho L. C., Impey C. D., Rix H.-W., 2010a, The Astronomical Journal, 139, 2097

Peng Y.-j., et al., 2010b, The Astrophysical Journal, 721, 193

Peng Y., Maiolino R., Cochrane R., 2015, Nature, 521, 192

Petrosian V., 1976, The Astrophysical Journal Letters, 209, L1

Pignatelli E., Fasano G., Cassata P., 2006, Astronomy and Astrophysics, 446, 373

Postman M., et al., 2012, The Astrophysical Journal Supplement Series, 199, 25

Ratra B., Vogeley M. S., 2008, Publications of the Astronomical Society of the Pacific, 120, 235

Ravindranath S., et al., 2004, The Astrophysical Journal Letters, 604, L9

Reddy N. A., Pettini M., Steidel C. C., Shapley A. E., Erb D. K., Law D. R., 2012, The Astrophysical Journal, 754, 25

Renzini A., 2006, Annual Review of Astronomy and Astrophysics, 44, 141

Rettura A., et al., 2010, The Astrophysical Journal, 709, 512

Robotham A. S. G., Taranu D. S., Tobar R., Moffett A., Driver S. P., 2017, Monthly Notices of the Royal Astronomical Society, 466, 1513

Rodriguez-Gomez V., et al., 2016, Monthly Notices of the Royal Astronomical Society, 458, 2371

Roy N., et al., 2018, Monthly Notices of the Royal Astronomical Society, 480, 1057

Sachdeva S., 2013, Monthly Notices of the Royal Astronomical Society, 435, 1186

Sachdeva S., Saha K., Singh H. P., 2017, The Astrophysical Journal, 840, 79

Sargent M. T., et al., 2007, The Astrophysical Journal Supplement Series, 172, 434

Sawicki M., 2012, Publications of the Astronomical Society of the Pacific, 124, 1208

Sawicki M. J., Lin H., Yee H. K. C., 1997, The Astronomical Journal, 113, 1

Sawicki M., et al., 2019, Monthly Notices of the Royal Astronomical Society, 489, 5202

Sawicki M., Arcila-Osejo L., Golob A., Moutard T., Arnouts S., Cheema G. K., 2020, Monthly Notices of the Royal Astronomical Society, 494, 1366

Scarlata C., et al., 2007, The Astrophysical Journal Supplement Series, 172, 406

Schaefer A. L., et al., 2017, Monthly Notices of the Royal Astronomical Society, 464, 121

Schechter P. L., 1980, The Astronomical Journal, 85, 801

Schombert J., McGaugh S., Lelli F., 2019, Monthly Notices of the Royal Astronomical Society, 483, 1496

Scoville N., et al., 2007, The Astrophysical Journal Supplement Series, 172, 1

Scoville N., et al., 2013, The Astrophysical Journal Supplement Series, 206, 3

Sellwood J. A., 2014, Reviews of Modern Physics, 86, 1

Sersic J. L., 1968, Atlas de Galaxias Australes. Observatorio Astronomico de Cordoba, Cordoba, Argentina

Shen S., Mo H. J., White S. D. M., Blanton M. R., Kauffmann G., Voges W., Brinkmann J., Csabai I., 2003, Monthly Notices of the Royal Astronomical Society, 343, 978

Simard L., 1998, in Albrecht R., Hook R. N., Bushouse H. A., eds, Astronomical Society of the Pacific Conference Series Vol. 145, Astronomical Data Analysis Software and Systems VII. p. 108

Skelton R. E., et al., 2014, The Astrophysical Journal Supplement Series, 214, 24

Smirnov N., 1948, The Annals of Mathematical Statistics, 19, 279

Sohn J., Chon G., Böhringer H., Geller M. J., Diaferio A., Hwang H. S., Utsumi Y., Rines K. J., 2018, The Astrophysical Journal, 855, 100

Sohn J., Geller M. J., Zahid H. J., Fabricant D. G., 2019, The Astrophysical Journal, 872, 192

Somerville R. S., Davé R., 2015, Annual Review of Astronomy and Astrophysics, 53, 51

Somerville R. S., et al., 2008, The Astrophysical Journal, 672, 776

Somerville R. S., et al., 2018, Monthly Notices of the Royal Astronomical Society, 473, 2714

Stanford S. A., Eisenhardt P. R., Dickinson M., 1998, The Astrophysical Journal, 492, 461

Stephens M. A., 1974, Journal of the American Statistical Association, 69, 730

Strauss M. A., et al., 2002, The Astronomical Journal, 124, 1810

Sweet S. M., et al., 2017, Monthly Notices of the Royal Astronomical Society, 464, 2910

Szomoru D., Franx M., Bouwens R. J., van Dokkum P. G., Labbé I., Illingworth G. D., Trenti M., 2011, The Astrophysical Journal Letters, 735, L22

Tacchella S., et al., 2015, Science, 348, 314

Thibert N. C. M., 2018, Master's Thesis, Saint Mary's University, Halifax

Tonry J., Davis M., 1979, The Astronomical Journal, 84, 1511

Toomre A., 1964, The Astrophysical Journal, 139, 1217

Toomre A., Toomre J., 1972, The Astrophysical Journal, 178, 623

Trujillo I., Aguerri J. A. L., Cepa J., Gutiérrez C. M., 2001, Monthly Notices of the Royal Astronomical Society, 328, 977

Trujillo I., Erwin P., Ramos A. A., 2004, The Astronomical Journal, 127, 26

Trujillo I., Ferreras I., de La Rosa I. G., 2011, Monthly Notices of the Royal Astronomical Society, 415, 3903

Valentino F., et al., 2020, The Astrophysical Journal, 889, 93

Valentinuzzi T., et al., 2010a, The Astrophysical Journal, 712, 226

Valentinuzzi T., et al., 2010b, The Astrophysical Journal Letters, 721, L19

Vazdekis A., 2008, in Knapen J. H., Mahoney T. J., Vazdekis A., eds, Astronomical Society of the Pacific Conference Series Vol. 390, Pathways Through an Eclectic Universe. p. 255

Weinberg M. D., 1997, The Astrophysical Journal, 478, 435

Williams R. J., Quadri R. F., Franx M., van Dokkum P., Labbé I., 2009, The Astrophysical Journal, 691, 1879

Williams R. J., Quadri R. F., Franx M., van Dokkum P., Toft S., Kriek M., Labbé I., 2010, The Astrophysical Journal, 713, 738

Wuyts S., et al., 2007, The Astrophysical Journal, 655, 51

Wuyts S., et al., 2012, The Astrophysical Journal, 753, 114

Xiao T., Wang T., Wang H., Zhou H., Lu H., Dong X., 2012, Monthly Notices of the Royal Astronomical Society, 421, 486

Zahid H. J., Geller M. J., 2017, The Astrophysical Journal, 841, 32

Zahid H. J., Damjanov I., Geller M. J., Chilingarian I., 2015, The Astrophysical Journal, 806, 122

Zahid H. J., Sohn J., Geller M. J., 2018, The Astrophysical Journal, 859, 96

Zahid H. J., Geller M. J., Damjanov I., Sohn J., 2019, The Astrophysical Journal, 878, 158

Zanella A., et al., 2016, The Astrophysical Journal, 824, 68

de Jong R. S., 1996, Astronomy and Astrophysics Supplement Series, 118, 557

de Souza R. E., Gadotti D. A., dos Anjos S., 2012, Astrophysics Source Code Library, p. ascl:1204.003

de Vaucouleurs G., 1953, Monthly Notices of the Royal Astronomical Society, 113, 134

van Dokkum P. G., et al., 2010, The Astrophysical Journal, 709, 1018

van de Voort F., Bahé Y. M., Bower R. G., Correa C. A., Crain R. A., Schaye J., Theuns T., 2017, Monthly Notices of the Royal Astronomical Society, 466, 3460

van der Kruit P. C., Freeman K. C., 2011, Annual Review of Astronomy and Astrophysics, 49, 301

van der Kruit P. C., Searle L., 1981, Astronomy and Astrophysics, 95, 105

van der Wel A., et al., 2011, The Astrophysical Journal, 730, 38

van der Wel A., et al., 2014, The Astrophysical Journal, 788, 28